Title
Electric-field noise scaling and wire-mediated coupling of remote ions in a novel elevator surface trap

Author
An, Da

Publication Date
2021

Peer reviewed|Thesis/dissertation

Electric-field noise scaling and wire-mediated coupling of remote ions in a novel elevator surface trap

by

Da An

A dissertation submitted in partial satisfaction of the

requirements for the degree of

Doctor of Philosophy

in

Physics

in the

Graduate Division

of the

University of California, Berkeley

Committee in charge:

Professor Hartmut Häffner, Chair
Professor Norman Yao
Professor Evan Williams

Spring 2021

Electric-field noise scaling and wire-mediated coupling of remote ions in a novel elevator surface trap

Abstract

Electric-field noise scaling and wire-mediated coupling of remote ions in a novel elevator surface trap

by

Da An

Doctor of Philosophy in Physics

University of California, Berkeley

Professor Hartmut Häffner, Chair

In this work, we present the design, fabrication, and operation of a novel surface-electrode Paul trap that produces a radio-frequency-null along the axis perpendicular to the trap surface. This arrangement enables control of the vertical trapping potential and consequentially the ion-electrode distance via dc-electrodes only. We demonstrate confinement of single $^{40}Ca^{+}$ ions at heights between 50 µm and 300 µm above planar copper-coated aluminium electrodes. Laser-cooling and coherent operations are performed on both the planar and vertical motional modes. This architecture provides a platform for precision electric-field noise detection, trapping of vertical ion strings without excess micromotion, and may have applications for scalable quantum computers with surface ion traps.

In our novel surface trap, we probe electric-field noise for ion-surface distances d between 50 µm and 300 µm in the normal and planar directions. We find the noise distance dependence to scale as $d^{-2.6}$ in our trap and a frequency dependence which is consistent with $1/f$ noise. Simulations of the electric-field noise specific to our trap geometry provide evidence that we are not limited by technical noise sources. Our distance scaling data is consistent with a noise correlation length of about 100 µm at the trap surface, and we discuss how patch potentials of this size would be modified by the electrode geometry.

Finally, we achieve coupling between the motions of trapped ions separated by 620 µm. Our results mark the first implementation of remote ion-ion interactions enhanced via an electrically floating metallic wire in an RF Paul trap. By tuning the confinement of each ion into resonance, we demonstrate classical energy exchange through sympathetic heating and heating rate reduction. The coupling interaction exchange time is extracted to be 22 ms. Practical improvements to the ion-wire-ion system are discussed, with realistic applications to sympathetic cooling of remote ions and more optimistic goals of coherent energy exchange at the single-quantum level. Our ion-wire-ion system establishes a building block for scalable

trapped ion quantum computers and provides a tool for quantum communication between qubits of different types.

To my parents, who have always encouraged me.
And to my wife, who has always supported me.

Acknowledgments

This Ph.D. work could not have been accomplished without the support of my colleagues, my friends, and my family. I take the time here to emphasize the appreciation I have for those who have greatly helped me along my journey.

To start off, I would like to thank my advisor, Hartmut Häffner, who has provided invaluable guidance throughout my Ph.D. and has taught me the mindset and joys of being a physicist. I cannot thank him enough for cultivating a fantastic research environment and community where I had the intellectual and financial freedom to explore any of my scientific interests.

I am fortunate to have had the pleasure of working alongside several amazing graduate students and remarkable post-docs. In particular, I am thankful to have worked with Clemens Matthiesen, whose perseverance and enthusiasm fostered experimental success and astute exchange of ideas. I also want to thank Erik Urban for welcoming me into the group and showing me how to be a great ion trapper and scientist. Thanks to Dylan Gorman, Ahmed Abdelrahman, and Nikos Daniilidis for laying the theoretical and experimental groundwork for my project. And thanks to Maya Berlin-Udi and Alberto Alonso for their insightful discussions and help with setting up experiments. I would also like to recognize the undergraduate students, Jun Wang and Liona Fan-Chiang, who executed valuable simulation work for our double trap. And shout-out to Joe Broz for his help with ensuring all the lab operations run smoothly. To the rest of my awesome labmates: Soenke, Crystal, Neil, Nicole, Ryan, Eli, Boerge, Wei-Ting, Sara, and Sumanta, thank you for sharing many enlightening and fun conversations both inside and outside of the lab.

Of course, I would not be here without the support and endless encouragement of my parents. Thank you to my dad for teaching me how to stay calm in the face of challenge. And thank you to my mom for filling my life with positivity and excitement. Finally, to my wife, Katherine, thank you for being the best friend and support system I could ever ask for and thank you for keeping my journey light-hearted.

Contents

List of Figures

Chapter 1

Introduction

Trapped atomic ions have emerged as a promising platform for the physical realization of quantum computation and simulation [1], due in part to their identical and well isolated nature along with long coherence times of the internal qubit states. Trapped ion systems also have demonstrated high-fidelity single-qubit and multi-qubit coherent operations, up to 99.9999% for single-qubit gates [2] and 99.9% for two-qubit gates [3, 4], controllable through external electromagnetic fields and laser light.

My thesis work is centered around a novel surface ion trap design which allows simple shuttling of ions perpendicular to the trap surface. The first hurdle of this thesis work was the implementation and characterization of such a trap. For its ability to transport ions up and down with purely DC fields, we term this trap as the "elevator" trap. Using the elevator trap as a tool, two main experimental results are presented in this thesis: electric-field noise distance scaling and wire-mediated long-range ion-ion energy exchange.

In reference to the first result, a prominent challenge for the miniaturization of ion traps, necessary for scaling to large numbers of qubits and smaller footprints, is the presence of electric-field noise. This noise causes decoherence of the ion motional modes and limits the fidelity of multi-ion qubit interactions [5]. The electric field noise originates from surfaces close to the trapped ion and is typically orders of magnitude larger than the Johnson noise expected from the thermal motion of the electrons in a conductor of the same geometry [6]. While identifying the microscopic sources of this excess electric-field noise is an active topic of research, it has been found to scale strongly with distance to the trap surface [6, 7]. To date, various possible sources of such excess electric-field noise have been proposed and studied theoretically, resulting in a range of possible distance scalings [6, 8, 9]. In this thesis work, we measure a precise noise scaling with distance to provide information on the spatial extent of surface noise sources. This information may aid the community to understand the underlying mechanisms behind excess surface noise and allow engineering of better ion traps or inspire reliable surface treatments. Beyond ion traps, surface electric-field noise limits the performance of solid-state quantum sensors, such as nitrogen-vacancy centers in diamond [10], and hinders precision measurements, including gravitational probes with charged particles [11, 12] and Casimir-Polder force studies [13, 14]. Thus, a better

understanding of surface noise in ion traps may help advance research in these fields.

Another key feature for scalable trapped ion technology is the ability to communicate information between distant ions in separate traps. Control in a single trapping potential is limited to tens of ions due to trap frequency crowding and other technical challenges. Thus, scaling trapped ion systems to hundreds of ions requires a modular architecture which features several linked ion registers. Proposed interconnect mechanisms among these registers may take the form of shuttling ions or generating photonic links. In this thesis, we explore an alternative to these interconnects that involves transferring quantum information from one ion to another distant ion through a classical wire. The ideas behind this project date even prior to the inception of the Häffner lab at UC Berkeley in 2009. Over the years, this ambitious project has challenged generations of researchers and undergone a few iterations. The first iteration of the experiment was designed with a standard linear surface trap with a wire suspended above the trap using piezo translation stages [15]. Ultimately, we arrived at a trap design which integrated the coupling wire onto the surface trap itself. The 500 µm long electrically floating wire connects two separate trapping zones, each modeled after the elevator trap. With this trap, we provide experimental results showing the energy exchange between two remote ions enhanced via the shared metallic wire. These results mark the base of future ion-wire-ion systems, which may lead to large-scale modular ion traps or hybridized versions of trapped ion qubits and solid-state qubits for quantum computation.

An outline of this thesis is given by the following: We begin in **Chapter 2** with a brief review of the physics behind ion trapping and provide example designs for standard ion traps. In **Chapter 3**, we explore the atomic structure of the $^{40}Ca^{+}$ ion and analyze basic laser-ion interactions required for control and measurement of an ion in our experiments.

In **Chapter 4**, we introduce a novel surface trap design, the four-RF-electrode trap, which we colloquially term the "elevator" trap. This trap design features RF fields that provide confinement in the trap plane, but cancel along the vertical axis which is perpendicular to the trap surface. The ion trapping height and vertical potential are fully controlled with DC fields, simplifying vertical shuttling, hence the "elevator" moniker, and allowing for trapping of vertical ion strings. With this design, we have demonstrated trapping at heights ranging from 50 to 300 µm above the trap surface. We also discuss potential applications of the trap design in quantum control and electric field sensing.

Chapter 5 details the experimental setup of our ion trap apparatus, including fabrication, assembly, electronics, optics, and challenges faced and overcome throughout the process.

In **Chapter 6**, we present the first scientific results utilizing the elevator trap. Explicitly, we probe electric-field noise in a surface ion trap for ion-surface distances d between 50 and 300 µm in the normal and planar directions. We find the noise distance dependence to scale as $d^{-2.6}$ in our trap and a frequency dependence which is consistent with $1/f$ noise. Simulations of the electric-field noise specific to our trap geometry provide evidence that we are not limited by technical noise sources. Our distance scaling data is consistent with a noise correlation length of about 100 µm at the trap surface, and we discuss how patch potentials of this size would be modified by the electrode geometry.

Finally, in **Chapter 7**, we present a novel long-range ion-ion coupling mechanism: motional dipole-dipole coupling of two ions in separate traps enhanced via an electrically floating metallic wire. Here, two ions are held in separate trapping zones, and their motions induce oscillating charges in a shared wire, which acts as an intermediate bus to communicate between the ions. We demonstrate classical energy exchange between the two separated ions connected with a wire. Improvements are discussed in order to bring the energy exchange into the single-quantum regime. We conclude with and overview of applications for such a capability, including scalable quantum networks and hybrid quantum architectures.

Chapter 2

Ion traps

As charged particles, ions have naturally strong interactions with electromagnetic fields. Taking advantage of this feature, we can spatially confine ions in three-dimensions with an appropriate choice of fields. These external trapping fields in combination with the mutual Coulomb interaction between ions allows the formation of ion crystals, or spatially separated individual ions with shared motion. The two main schemes for physical realization of trapped ions utilize either oscillating electric fields (Paul traps) or oscillating magnetic fields (Penning traps). In this chapter, we describe the theory behind the former scheme, and discuss the standard physical implementations of radio-frequency (RF) Paul traps.

2.1 Paul traps

3-D confinement of an ion is impossible to achieve with solely static (DC) electric fields. This can be seen by attempting to solve Laplace's equation, $\nabla^2\Phi = 0$, with a static quadrupole potential,

$$\Phi(x, y, z) = \frac{U_0}{2r_0^2} \sum_i \alpha_i x_i^2. \tag{2.1}$$

where U_0 is the static voltage, r_0 is the characteristic ion-electrode distance, x_i correspond to the three spatial dimensions x, y, z, and α_i are geometric factors in the i^{th} dimension. There are two mathematical requirements to establish confinement in 3-D for positively charged ions. The first requirement is to maintain a confining concavity of the quadratic potential in all dimensions, meaning

$$\alpha_i > 0, \forall i = 1, 2, 3. \tag{2.2}$$

The second requirement is to satisfy Laplace's equation, which is equivalent to satisfying

$$\sum_i \alpha_i = 0. \tag{2.3}$$

All non-trivial solutions to Eq. (2.3) imply that we must have at least one dimension with anti-confining potential, i.e. $\alpha_i < 0$. However, this is explicitly in contradiction with the

first requirement stated in Eq. (2.2). From this contradiction, we conclude the impossibility of creating a fully confining static electric potential in 3-D space.

A solution to this dilemma was introduced by Wolfgang Paul in 1953 [16]. Broadly, the idea was to generate 3-D confinement with dynamic electric fields rather than static fields. The validity of Paul's design centers on an averaging effect from the oscillating RF trapping fields, and can be conceptually understood as the following: At any instantaneous point in time, we must have a saddle-like potential, with anti-confinement in at least one orthogonal spatial dimension. However, we can oscillate the potential in time such that the confinement and anti-confinement axes switch back and forth. If this is done fast enough, an ion located at the center of this oscillating potential will experience an averaged confining force in all dimensions where the voltage oscillation is non-zero.

2.1.1 Classical ion motion

We investigate this mathematically following the analysis from [17, 1]. By adding a time-dependent term to the potential in Eq. (2.1), we arrive at the full electric potential that can be written as

$$\Phi(x,y,z,t) = \frac{U_0}{2r_0^2}\sum_i \alpha_i x_i^2 + \frac{V_0}{2r_0^2}\cos(\Omega_{RF}t)\sum_i \alpha_i' x_i^2. \tag{2.4}$$

where V_0 is the amplitude of the oscillating part of the potential, Ω_{RF} is the angular frequency of oscillation set by an external driving force, and α_i' is the geometric factor of the i^{th} oscillating potential.

Each spatial dimension in the potential, $\Phi(x,y,z,t)$, can be treated independently, and the one-dimensional classical equation of motion of an ion with charge e and mass m is

$$\ddot{x} + \frac{e}{m}\frac{\partial \Phi}{\partial x} = \ddot{x} + \frac{e}{mr_0^2}(U_0\alpha + V_0\cos(\Omega_{RF}t))x = 0 \tag{2.5}$$

This can be reformulated into the Mathieu differential equation

$$\frac{d^2x}{d\xi^2} + [a_x - 2q_x\cos(2\xi)]x = 0 \tag{2.6}$$

where

$$\xi = \frac{\Omega_{RF}t}{2}\ ,\ a_x = -\frac{4eU_0\alpha}{mr_0^2\Omega_{RF}^2}\ ,\ q_x = \frac{2eV_0\alpha'}{mr_0^2\Omega_{RF}^2}. \tag{2.7}$$

The Mathieu equation has been shown to have stable solutions [1, 18, 19] of the form

$$x(\xi) = Ae^{i\beta_x\xi}\sum_{n=-\infty}^{\infty} C_{2n}e^{i2n\xi} + Be^{-i\beta_x\xi}\sum_{n=-\infty}^{\infty} C_{2n}e^{-i2n\xi} \tag{2.8}$$

where A and B are constants determined by initial conditions, and β_x and C_{2n} are functions of a_x and q_x. These stable solutions are only valid for certain values of a_x and q_x [1, 20]. One

such stable parameter region is where $(|a_x|, q_x^2) \ll 1$. All of the trapped ion experiments in this thesis have operated in this parameter regime. Working in this region along with the initial condition of $A = B$, we find the solution to the Mathieu equation to be

$$x(t) = A_x \cos(\beta_x \frac{\Omega_{RF}}{2} t)[1 - \frac{q_x}{2} \cos(\Omega_{RF} t)], \tag{2.9}$$

$$\beta_x = \sqrt{a_x + \frac{q_x^2}{2}} \tag{2.10}$$

where A_x is a constant determined by additional initial conditions.

The stable solution $x(t)$, in Eq. (2.9), represents the lowest-order approximate classical trajectory of an ion confined within a quadratic potential. On inspection of $x(t)$, we see that the motion consists of two oscillating terms: a large amplitude, slowly oscillating term at frequency $\omega_x = \beta_x \Omega_{RF}/2$, which is commonly referred to as 'secular' motion, and a small amplitude, fast oscillation at frequency Ω_{RF}, typically termed as 'micromotion'. Micromotion can be experimentally suppressed by bringing the ion into the RF null [17], making $q_x \approx 0$. The RF null is the position where the electric-field gradient is minimized; it sits at the saddle point of the electric potential, where the amplitude of the oscillating potential is typically zero. In most theoretical treatments [1], another assumption of low ion kinetic energy is made, implying $A_x \approx 0$. This condition is imposed to ensure that the ion motion does not cause significant deviation from the RF null. With the combination of $q_x \approx 0$ and $A_x \approx 0$, we find that the trapped ion motion may be fully capture by the secular motion,

$$x(t) \approx A_x \cos(\omega_x t). \tag{2.11}$$

We could have similarly arrived at this solution by using an effective stationary potential, known as a 'pseudopotential', to approximate the average RF potential. The intuition for this method is that, for $\omega_x \ll \Omega_{RF}$, over one period of ion oscillation, $\tau_x = 2\pi/\omega_x$, the force from the RF acting on the ion averages to zero. And so we can model the system with a pseudopotential,

$$\Psi(x) = \frac{e^2}{4m\Omega_{RF}^2} |\nabla \Phi(x)|^2 \tag{2.12}$$

2.2 Common RF trap designs

The electrode geometry and design of an ion trap is influenced by several functional factors. For example, it is prudent to generate confining potentials as harmonic as possible near the ion position because this leads to larger trapping depths and increased ion lifetimes. Additionally, the electrodes must be placed to provide 3-D control of the dipole and quadrupole electric-fields. In practice, many possible arrangements of RF and DC electrodes may satisfy the above conditions. In this section, we will discuss two such ion trap designs that have proved valuable to the trapped ion research community.

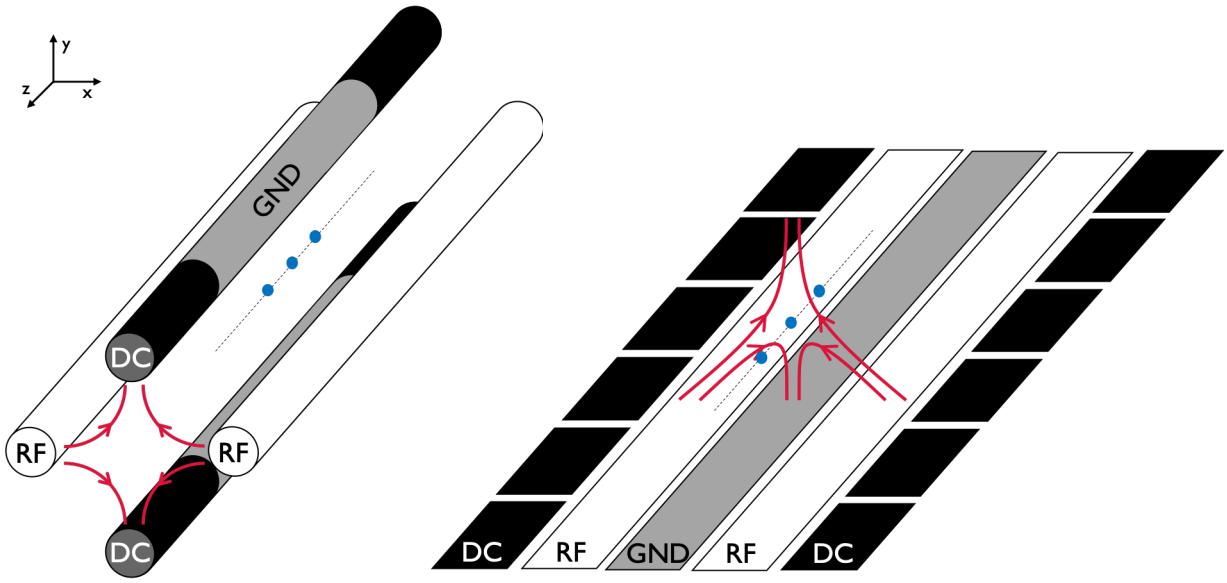

Figure 2.1: (Left) Schematic of electrode layout for a 3-D linear RF Paul trap. Static DC fields are applied to black electrodes, oscillating RF fields are applied to white electrodes, and gray electrodes are held as GND reference. The electric-field lines, shown in red, illustrate the instantaneous quadrupole field formed by the RF electrodes. With the appropriate voltages on each electrode, crystallized ion strings oriented along the $\hat{z}$ axis may form. (Right) Schematic of electrode layout for a standard five-wire linear surface trap design. The RF and GND electrodes can be directly mapped from the 3-D electrode rods, noting that the upper GND rod is now represented by GND at $y = \infty$. The resulting instantaneous RF electric-field lines are again shown in red, with quadrupole confinement similar the 3-D counterpart. Additionally, the 3-D DC endcaps are translated to multiple surface DC electrodes. The combination of RF and DC fields analogously traps ion strings along the $\hat{z}$ axis. Typical DC electrode voltages are on the order of 10 V, and RF electrodes are driven with order $10 - 100$ V at ~ 10 MHz.

2.2.1 3-D linear trap

A 3-D linear RF trap has electrode structure shown in Fig. 2.1 (left). Although many variations exist, the general architecture consists of four rods arranged symmetrically around a center axis. When two oppositely paired rod electrodes are driven with in-phase RF voltage, they generate oscillating quadrupole confinement in the radial $\hat{x}, \hat{y}$ directions, as shown by the red electric-field lines in Fig. 2.1. By symmetry of the RF electrodes, there is an RF null, or pseudopotential minimum, line that forms along the center $\hat{z}$ axis. Ions trapped along this RF null axis experience minimal micromotion, allowing the ion motion to be described by the secular approximation, as seen in Section 2.1.1. The remaining two opposite rods are split into segments that hold static DC potentials to confine ions in the axial $\hat{z}$ direction. Both the RF and DC potentials are referenced to a common ground (GND).

With an axial $\hat{z}$ confinement relatively weak compared to the radial $\hat{x}, \hat{y}$ confinement, this configuration will align multiple ions along the RF-null z axis in a linear chain. The separation between ions is determined by a balance between the ion-ion Coulomb force and the strength of confinement in the axial direction. Typical ion-ion separations are ~ 5 µm, allowing for individual addressing of each ion with independent laser beams. This capability and architecture has led to a plethora of exciting results in quantum information processing, quantum sensing, and quantum simulation [21, 22].

2.2.2 Linear surface ion trap

The first demonstration of a microfabricated surface-electrode ion trap [23] opened the path towards scalable quantum information processing with trapped ions. The design of a standard linear surface trap, shown in Fig. 2.1 (right), takes inspiration from its 3-D predecessor, and is often referenced as the five-wire trap design [24, 25]. The long RF rods are mapped and flattened onto the surface in the form of long RF electrodes, and the segmented DC rods are mapped onto segmented surface electrodes, with designated ground potentials on the trap surface and at infinity. This design maintains the quadrupole confinement of the 3-D linear traps, and can analogously trap linear chains of ions along the axial $\hat{z}$ direction.

The advantages of a surface trap architecture over 3-D traps include simplified fabrication of complex electrode structures, allowing for finer and more localized ion control, such as localized micromotion compensation, ion shuttling between trapping regions and through junctions [26, 27, 28], and splitting and merging of ion chains. Additionally, the footprint of surface traps are an order of magnitude smaller than bulky 3-D traps. Surface traps also take advantage of standardized micro- and nano-fabrication techniques, which make trap production more reliable, reproducable, and customizable. For instance, various groups have created surface traps with unique potential landscapes [29, 30] and on-chip integration of ion addressing beams have been demonstrated [31].

Of course, this architecture also comes with disadvantages. Because the spacing between electrodes is typically on the order of microns, the voltages must be kept relatively small (to prevent arching and damage to the traps), leading to lower trap depths and shorter ion lifetimes. Another disadvantage is a result of the 2-D limited geometry of the electrodes, which causes anharmonicities in the electric potentials. As a result, the quadratic approximation of the confinement potential does not spatially extend as far as its 3-D counterparts, leading to reduction of the trap depths of ~ 100 times [24]. Optical access is also essentially limited to laser beams parallel with the trap plane, since beams coming from below will not reach the ion and short wavelength ($\lesssim 450$ nm) beams coming from above will expose the surface electrodes to unwanted photo-electric charging [32]. Furthermore, trapped ions are held typically $30 - 300$ µm above the surface, which makes them sensitive to electric-field noise on the surface of the trap, see Chapter 6. This sensitivity causes unwanted motional decoherence, which negatively affects the fidelity of quantum operations.

Chapter 3

Laser-ion interactions

In this section, we will explore the internal structure of the $^{40}Ca^{+}$ ion, which acts as the experimental workhorse of this thesis. With the use of lasers, we are able to perform a variety of essential experimental operations on the $^{40}Ca^{+}$ ion. Accordingly, we continue the discussion with an overview of the basic laser-ion interactions required for control and measurement of an ion, such as ion state detection, cooling, and state manipulation.

3.1 Atomic structure of Calcium

3.1.1 $^{40}Ca^{+}$ production

We begin our discussion of the Ca atom by reviewing the experimental procedure for producing $^{40}Ca^{+}$ ions. In brief, single $^{40}Ca^{+}$ ions are produced by heating macroscopic granules of neutral Ca, causing sublimation of the Ca. The neutral Ca atoms generated in this way are then ionized with a set of localized lasers.

The setup to achieve this is shown in Fig. 3.1. This apparatus is referred to as the Ca "oven", composed of a stainless steel tube, which is open-ended on one side and filled with neutral Ca granules. Importantly, a thin sheet of tantalum foil wraps around the oven tube. By running electrical current through the tantalum foil and oven tube, we generate ohmic heating of the system, and a spray of heated Ca atoms exits the open end of the tube. The full circuit is routed outside of the vacuum chamber via two metallic arms connected to the oven tube and tantalum foil. Typically, we run the Ca oven with $2-4$ A, or $2-4$ W. Higher powers generally lead to faster loading of $^{40}Ca^{+}$ ions in the trap, but one must take care not to overdrive the oven, as this may lead to accidental coating of the electrode surfaces or higher in-vacuum pressures, increasing collisions and leading to unstable trapping. When packing the tube with Ca, it is important to minimize exposure to atmosphere because the Ca granules oxidize within a couple hours in air.

To generate $^{40}Ca^{+}$ from the spray of neutral Ca atoms, we perform photoionization, which can be feasibly accomplished with one, two, or three photon processes [33]. Even

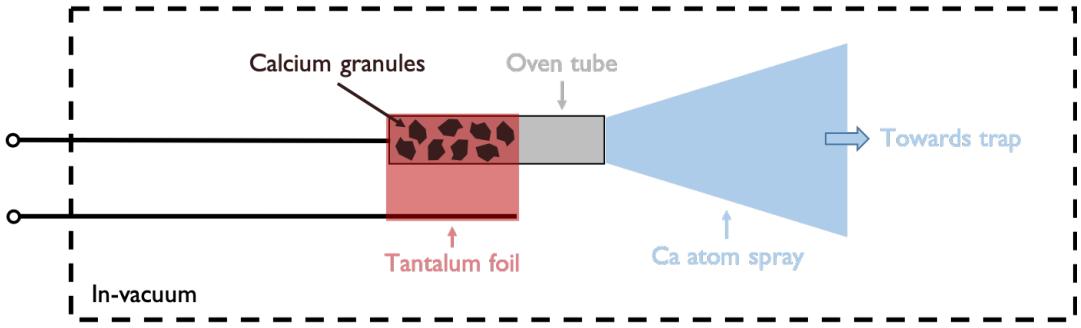

Figure 3.1: Schematic of the in-vacuum Ca oven. Two electrical leads receive external power to heat the oven tube in the region covered by tantalum foil. As the temperature rises in the tube, the Ca granules sublimate, and a spray of Ca atoms exits the open-ended oven tube. The path of a Ca atom upon exit is random and uncollimated, leading to a wide solid angle spray.

higher number photon processes may be conceived, but the resources required for such a task are not practical. We choose to work with the two-photon process because the one-photon process requires ultraviolet (UV) light near 203 nm, which is difficult to work with, and the three-photon process has a slower ionization rate. Starting with the $^1S_0$ electronic ground state of ^{40}Ca, 422 nm laser light excites the electron to the $^1P_1$ excited state. Then laser light with energy greater than 391 nm light excites the electron into the continuum, releasing a single electron from the ^{40}Ca atom. Typically, the 422 nm light is oriented perpendicular to the open-ended Ca tube so that Doppler shifts caused by the velocity of the spray of Ca atoms may be neglected.

3.1.2 $^{40}Ca^+$ energy levels

We are then left with singly ionized $^{40}Ca^+$, which has one valence electron, and thus a hydrogen-like internal energy level structure with a nuclear spin of $I = 0$, meaning there is no hyperfine structure. Fig. 3.2 shows the five lowest energy levels of $^{40}Ca^+$ along with the relevant transition wavelengths between states. The ground state, $S_{1/2}$, has electric-dipole transitions to the $P_{1/2}$ and $P_{3/2}$ excited states as well as electric-quadrupole transitions to the $D_{3/2}$ and $D_{5/2}$ excited states.

Of particular note is the $S_{1/2} \leftrightarrow P_{1/2}$ transition at 397 nm combined with the $P_{1/2} \leftrightarrow D_{3/2}$ transition at 866 nm. The manifold created by these three states is used for state detection, see Section 3.3, and Doppler cooling of the ion, see Section 3.4.1. Although the $S_{1/2} \leftrightarrow P_{1/2}$ transition at 397 nm takes center stage in these operations, the addition of the 866 nm laser crucially maintains an effective cycling transition between the $S_{1/2}$ and $P_{1/2}$ states. Because $P_{1/2}$ has a branching ratio of $(P_{1/2} \leftrightarrow S_{1/2})/(P_{1/2} \leftrightarrow D_{3/2}) = 14.54$ [34], absence of the 866 nm laser results in optical pumping of the electronic population into the $D_{3/2}$ state. The 866 nm light is required to repump population from $D_{3/2}$ back to the $P_{1/2}$ state, allowing us

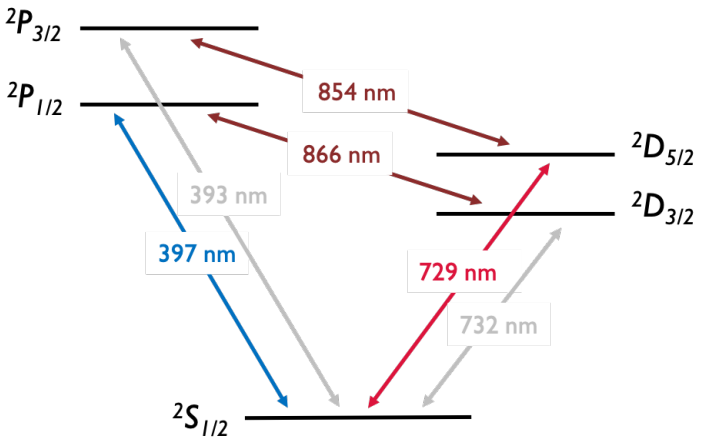

Figure 3.2: Energy level structure of $^{40}Ca^+$, with atomic states labeled as $^{(2S+1)}L_J$. Colored arrows indicate the transition wavelengths between states relevant to the experimental work in this thesis. For completeness, grey arrows show additional transition wavelengths from the electronic ground state, $S_{1/2}$.

to effectively neglect the $D_{3/2}$ state in our analysis.

Another important transition is the $S_{1/2} \leftrightarrow D_{5/2}$ transition at 729 nm. Although it is dipole-forbidden, enough laser power will coherently drive $S_{1/2} \leftrightarrow D_{5/2}$ as a quadrupole transition. This feature allows us to use the meta-stable $D_{5/2}$ state, with a naturally long lifetime of 1.2 s [35], as the excited state of our optical qubit. A quick path to reset our qubit from the $D_{5/2}$ state to the $S_{1/2}$ state is through the $D_{5/2} \leftrightarrow P_{3/2}$ transition at 854 nm, since the lifetime of the $P_{3/2}$ state is 7.4 ns [36]. Thus, a combination of the 729 nm and 854 nm transitions forms a manifold for coherent state manipulation between the ground state, $S_{1/2}$, and the excited state, $D_{5/2}$.

3.1.3 Zeeman sub-levels

For states with non-zero electronic total angular momentum, $\vec{J}$, an externally applied magnetic field, $\vec{B}$, will split the energy levels of the state due to the Zeeman effect. The energy shift of these Zeeman sub-levels is determined by

$$\Delta E = g_J \mu_B m_j |\vec{B}|, \tag{3.1}$$

where μ_B is the Bohr magneton, m_j is the magnetic quantum number, and g_J is the Landé g-factor given by

$$g_J = 1 + \frac{J(J+1) + S(S+1) - L(L+1)}{2J(J+1)} \tag{3.2}$$

where J is the total electronic angular momentum, L is the orbital angular momentum, and S is the spin angular momentum. In our experiments typically a magnetic field of $3-5$ G

is applied, which results in energy shifts on the order of 1 MHz. These energy splittings become relevant in the $S_{1/2} \leftrightarrow D_{5/2}$ transition, since the natural linewidth of this transition, ~ 0.16 Hz, is much narrower than 1 MHz. The $S_{1/2}$ state splits into 2 sub-levels while the $D_{5/2}$ state splits into 6 sub-levels. Combined with the fact that electric quadrupole transitions allow only $|\Delta m_j| \leq 2$, we find that optical spectroscopy of the $S_{1/2} \leftrightarrow D_{5/2}$ transition can result in 10 different transition lines.

In order to better approximate an ideal two-level atom, we may suppress excitation on some transitions with a combination of geometric interaction effects and optical pumping [36]. The interaction geometry can be parameterized by two angles: the angle between the laser beam propagation and the magnetic field, θ, and the angle between the laser beam polarization and the magnetic field vector projected into the plane of incidence, γ. For example, we may select only the $\Delta m = \pm 2$ transitions by setting $\theta = 90^\circ$ and $\gamma = 90^\circ$ [36], leaving us with 4 transition lines. Furthermore, we may halve the allowable transitions by suppressing excitations from the $S_{1/2}(m = +1/2)$ state via optically pumping the population into the $S_{1/2}(m = -1/2)$ state such that only the $S_{1/2}(m = -1/2) \leftrightarrow D_{5/2}(m = -5/2)$ and $S_{1/2}(m = -1/2) \leftrightarrow D_{5/2}(m = +3/2)$ transitions remain. The frequency splitting between these two transitions is large, typically $30 - 40$ MHz. Hence, for a single laser tone with frequency near one of the transitions, we may approximate the resulting dynamics with a two-level system.

3.2 Coherent operations

In this section, we provide an analysis of the coherent dynamics of trapped ions interacting with laser light. The discussion is centered around the full trapped ion Hamiltonian, $\hat{H}$,

$$\hat{H} = \hat{H}_m + \hat{H}_e + \hat{H}_i \tag{3.3}$$

where $\hat{H}_m$ is the trapped ion motional Hamiltonian, $\hat{H}_e$ is the internal electronic Hamiltonian, and $\hat{H}_i$ represents the laser-ion interaction Hamiltonian. In addition, we offer some intuition behind the dynamics through approximations within the Hamiltonian and pedagogical examples.

3.2.1 Quantized ion motion

To being, an accurate understanding of the coherent dynamics and cooling process of ions requires a quantum-mechanical picture of their motion. With the help of various laser cooling techniques, see Section 3.4, the kinetic energy of trapped ions may be reduced to levels near their motional ground state. In this regime, the harmonic motion of the ions may be treated quantum-mechanically. In order to fully capture the quantum state of a trapped ion, we must account for these quantized motional states of the $^{40}Ca^{+}$ ion in harmonic trapping potentials in addition to the internal electronic states from Section 3.1. Explicitly, the

motional Hamiltonian of the system takes the familiar form,

$$\hat{H}_m = \sum_i (\frac{\hat{p}_i}{2m} + \frac{1}{2}m\omega_i^2\hat{x}_i) = \sum_i \hbar\omega_i(\hat{a}_i^\dagger\hat{a}_i + \frac{1}{2}) \tag{3.4}$$

$$\hat{a}_i^\dagger = \sqrt{\frac{m\omega_i}{2\hbar}}(\hat{x}_i - \frac{i}{m\omega_i}\hat{p}_i)\ ,\ \hat{a}_i = \sqrt{\frac{m\omega_i}{2\hbar}}(\hat{x}_i + \frac{i}{m\omega_i}\hat{p}_i), \tag{3.5}$$

where $\hat{a}^\dagger$ and $\hat{a}$ are, respectively, the creation and annihilation operators of the quantum harmonic oscillator.

3.2.2 Laser interactions with two-level atom

We continue our discussion under the assumption that the electronic energy levels of $^{40}Ca^+$ may be treated as an effective two-level system on one of the $S_{1/2} \leftrightarrow D_{5/2}$ transitions, with ground state $|S\rangle$ and excited state $|D\rangle$. As such, we take advantage of the the Pauli spin operators σ_z, σ^+, and σ^- to represent our system. The energy of the internal electronic states is described by the Hamiltonian $\hat{H}_e$,

$$\hat{H}_e = \frac{\hbar\nu}{2}\sigma_z, \tag{3.6}$$

where ν is the atomic transition frequency between the $|S\rangle$ and $|D\rangle$ states.

The excitation in the $|S\rangle \leftrightarrow |D\rangle$ manifold may be controlled by laser light, where the one-dimensional electric-field of the laser light that addresses the transition is described by

$$\vec{E}(x,t) = \mathcal{E}e^{i(kx-\nu_L t+\phi)} + \mathcal{E}^* e^{-i(kx-\nu_L t+\phi)} \tag{3.7}$$

where $\mathcal{E}$ is the magnitude of electromagnetic wave, ν_L is the frequency of the laser light, k is the wavenumber, and ϕ is the phase. The interaction of our two-level atom with a light-field is given by the Hamiltonian $\hat{H}_i = -\hat{d}\cdot\vec{E}$, where $\hat{d} = \mu(\sigma^+ + \sigma^-)$ is the ion's electric dipole moment with matrix element μ. In particular, interaction with a laser parameterized by Eq. (3.7) produces

$$\hat{H}_i = \frac{\hbar\Omega_R}{2}(\sigma^+ + \sigma^-)(e^{i(kx-\nu_L t+\phi)} + e^{-i(kx-\nu_L t+\phi)}), \tag{3.8}$$

where the coupling strength is defined by the Rabi frequency, $\Omega_R = \mu\mathcal{E}/\hbar$.

The dynamics of the system can be best seen by transforming into the interaction picture with $U = exp[-i(\hat{H}_m + \hat{H}_e)t/\hbar]$, where our Hamiltonian becomes

$$H_I = U^\dagger H_i U = \frac{\hbar\Omega_R}{2}(\sigma^+ e^{i(kx-\delta t+\phi)} + \sigma^- e^{-i(kx-\delta t+\phi)}) \tag{3.9}$$

with $\delta = \nu_L - \nu$. Note that we have applied the rotating-wave approximation in Eq. (3.9) because the rapidly oscillating terms, with frequencies $\nu_L + \nu$, have little effect on the time-evolution of the system, and can thus be neglected [37].

At this point, it is relevant to talk about the different length scales associated with the laser wavelength, λ, and ion spatial extent, x_0. The Lamb-Dicke parameter, η, is defined to be the ratio between these two quantities,

$$\eta = \frac{2\pi x_0}{\lambda} = k_x \sqrt{\frac{\hbar}{2m\omega_t}} = \sqrt{\frac{\omega_R}{\omega_t}}, \tag{3.10}$$

where $k_x = \vec{k} \cdot \hat{x}$ is projection of the laser onto the ion's motion in the $\hat{x}$-direction. The last equality in Eq. (3.10) gives additional intuition about the Lamb-Dicke parameter as a function of the trap frequency, ω_t, and the ion's recoil energy, $\omega_R = \hbar k^2/2m$, upon absorption or emission of a photon. Now using the equality $k_x x = \eta(a+a^\dagger)$, we can reformulate Eq. (3.9) as

$$H_I = \frac{\hbar\Omega_R}{2}(e^{i\eta(\hat{a}+\hat{a}^\dagger)}\sigma^+ e^{-i(\delta t-\phi)} + e^{-i(\eta(\hat{a}+\hat{a}^\dagger)}\sigma^- e^{i(\delta t-\phi)}), \tag{3.11}$$

which will permit a better physical understanding of the dynamics in Section 3.2.3.

3.2.3 Lamb-Dicke regime

When the spatial extent of the atomic wavepacket is much smaller than the transition wavelength, we find ourselves in the Lamb-Dicke regime, defined by $\eta^2(2n+1) \ll 1$. Our experiments are often run in this regime, with typical parameters of $\omega_R \sim 10$ kHz and $\omega_t \sim$ MHz, resulting in a small parameter $\eta \sim 0.1$. Hence, we can expand the Hamiltonian in Eq. (3.11) with the Taylor expansion

$$e^{i\eta(\hat{a}+\hat{a}^\dagger)} \approx 1 + i\eta(\hat{a}+\hat{a}^\dagger) + \mathcal{O}(\eta), \tag{3.12}$$

meaning that transitions which change the motional quanta by more than one are suppressed, and we arrive at the simplified Hamiltonian

$$H_I = \frac{\hbar\Omega_R}{2}[(1+i\eta(\hat{a}+\hat{a}^\dagger))\sigma^+ e^{-i(\delta t-\phi)} + (1+i\eta(\hat{a}+\hat{a}^\dagger))\sigma^- e^{i(\delta t-\phi)}]. \tag{3.13}$$

In this regime, there are only three important resonances to consider. After setting $\phi = 0$ for simplicity, the first resonance occurs for $\delta = 0$, and is referred to as the *carrier* transition, which takes the form

$$H_{car} = \frac{\hbar}{2}\Omega_{car}[\sigma^+ + \sigma^-]. \tag{3.14}$$

This Hamiltonian gives rise to $|S,n\rangle \leftrightarrow |D,n\rangle$ transitions, with coupling strength described by the Rabi frequency, Ω_{car}. Although carrier transitions do not affect the ion motional states, the coupling strength is affected by the motional state of the ion. This effect to second order is

$$\Omega_{car} = \Omega_R L_n(\eta^2) \approx \Omega_R(1-\eta^2 n). \tag{3.15}$$

This relationship physically arises from the perceived Doppler shift of the laser frequency from the ion's frame. As the magnitude of the motion increases with increasing quantum

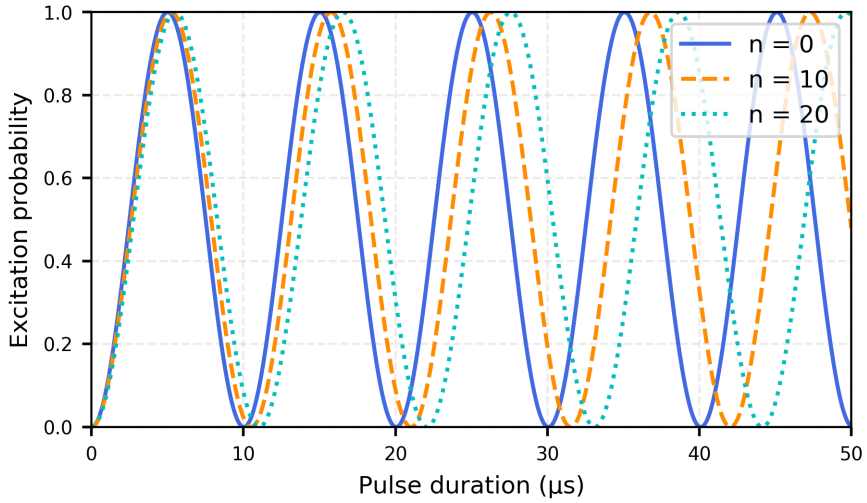

Figure 3.3: Simulated carrier Rabi flops with bare Rabi frequency $\Omega_0 = 2\pi \times 10$ μs. The Rabi excitations for Fock states $n = 0$ (10/20) are shown in blue (orange/cyan)

number, n, the Doppler-induced detuning from the carrier transition increases as well, thus decreasing the coupling strength of the carrier transition.

The second resonance occurs for $\delta = -\omega_t$ and is called the *first red sideband* transition, with a Hamiltonian of the form

$$H_{rsb} = \frac{\hbar}{2}\Omega_R\eta[\hat{a}\sigma^+ + \hat{a}^\dagger\sigma^-]. \tag{3.16}$$

This Hamiltonian leads to $|S, n\rangle \leftrightarrow |D, n-1\rangle$ transitions, with coupling strength $\Omega_{rsb} = \eta\sqrt{n}\Omega_R$. This interaction removes one quantum of motion as the ion's internal electronic state is excited, analogous to the Jaynes-Cumming Hamiltonian in Cavity QED.

The third resonance is referred to as the *first blue sideband* transition and occurs for $\delta = \omega_t$, with Hamiltonian

$$H_{bsb} = \frac{\hbar}{2}\Omega_R\eta[\hat{a}^\dagger\sigma^+ + \hat{a}\sigma^-], \tag{3.17}$$

giving rise to transitions of the type $|S, n\rangle \leftrightarrow |D, n+1\rangle$, with Rabi frequency $\Omega_{bsb} = \eta\sqrt{n+1}\Omega_R$. Sometimes called the anti-Jaynes-Cummings Hamiltonian, this interaction adds one quantum of motion while also exciting the electronic state of the ion.

3.2.4 Coherent dynamics

At this stage, we are equipped to explore and visualize the time-evolution of the transitions described in Section 3.2.3. Starting with the carrier transition, we see the effect of varying the fock state manifold, which results in different Rabi frequencies. As shown in Fig. 3.3,

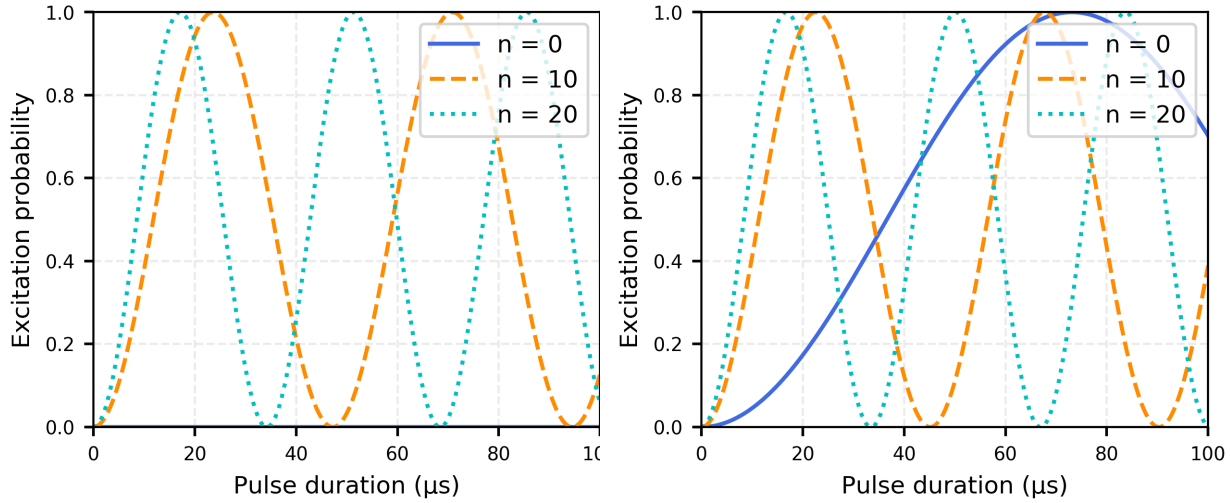

Figure 3.4: (Left) Simulated first-order red sideband Rabi flops with bare Rabi frequency $\Omega_0 = 2\pi \times 10$ μs. (Right) Simulated first-order blue sideband Rabi flops. The Rabi excitations for Fock states $n = 0$ (10/20) are shown in blue (orange/cyan). Note there is no red sideband excitation for the $n = 0$ Fock state.

an increase in $|n\rangle$ results in a weaker coupling strength for the $|S, n\rangle \leftrightarrow |D, n\rangle$ transition, as expected from Eq. (3.15).

The coupling strength of the sideband transitions exhibit the opposite behavior with changing $|n\rangle$, and actually increase with increasing $|n\rangle$. This trend can be seen in Fig. 3.4, where Fig. 3.4(left) shows the time-evolution of the first-order red sideband for $|n\rangle = 0, 10,$ and 20, and Fig. 3.4(right) shows the time-evolution of the first-order blue sideband for the same $|n\rangle$ sequence.

3.3 State detection

Following an analysis of the theory behind coherent operations with a two-level ion, it is appropriate to describe an experimental method of measuring the $^{40}Ca^{+}$ ion state. In order to probe whether an ion is in the $|S\rangle$ ground state or the $|D\rangle$ excited state, we employ the electron shelving technique. By driving the $S_{1/2} \leftrightarrow P_{1/2}$ transition with a laser near 397 nm, we project the ion into one of two states in the subspace $|S\rangle, |D\rangle$. If the ion is in the $|S\rangle$ state, it will fluoresce from photon scattering on the $S_{1/2} \leftrightarrow P_{1/2}$ transition. Conversely, if the ion is in the $|D\rangle$ state, it will appear dark, as 397 nm light does not excite any transitions and thus no photons are scattered.

We collect the scattered photons into a photomultiplier tube (PMT) and gather statistics on the number of collected photons following each experiment. The resulting data for 100 realizations of the same quantum state is shown in Fig. 3.5, where we have collected photons

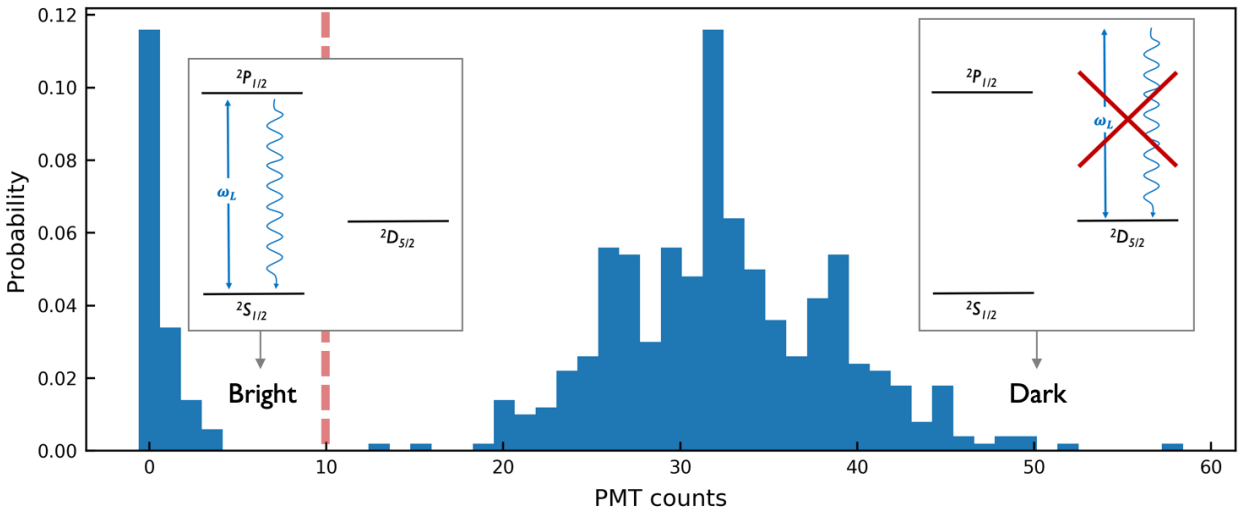

Figure 3.5: Normalized state readout histogram of 100 experiments with 2 ms exposure time on a PMT in kiloCounts. The dashed red line designates a threshold which separates the readout counts of bright and dark states. Overlaid are energy level diagrams and transitions for readout of an ion in the bright state, $|S\rangle$ (left) and in the dark state, $|D\rangle$ (right).

in the PMT for 2 ms after each realization. The particular state represented in Fig. 3.5 is a superposition of $|S\rangle$ and $|D\rangle$, $|\psi\rangle = |\alpha|^2 |S\rangle + |\beta|^2 |D\rangle$. The values of $|\alpha|^2$ and $|\beta|^2$ may be extracted from the readout counts associated with bright $|S\rangle$ and dark $|D\rangle$ states, respectively, where the distinction between the two states is set by a threshold on the number of collected photons, designated by the red dashed line in Fig. 3.5. In practice, the threshold state discrimination is a sufficient method, but we note that a more thorough analysis of α and β may be performed with fits of the histograms to Poisson distributions [36].

3.4 Laser cooling

3.4.1 Doppler cooling

Conceptually, the physics of Doppler cooling is centered on the Doppler effect and may be naively explained with energy conservation. To illustrate this, let us consider a single cycle in the Doppler cooling process. We begin with a laser, red-detuned from an atomic dipole transition and directed onto a trapped ion in harmonic motion. As the ion moves toward the laser light, it may absorb a red-detuned photon, since, in the ion's frame of reference, the Doppler effect shifts the photon frequency onto resonance with the atomic transition. Successively, a photon resonant with the atomic transition is spontaneously emitted, resulting in a net loss of energy from the ion.

Using a more analytical approach, we can understand Doppler cooling with a semi-classical picture of the atomic motion, which includes dissipative forces induced by laser

light and momentum fluctuations caused by spontaneous emission. Qualitatively, we expect to reach a motional equilibrium once the viscous Doppler laser cooling rate equals the spontaneous emission heating rate. Quantitatively, we may determine this equilibrium Doppler cooling temperature limit using the Einstein relation for a one-dimensional system,

$$D = m\eta k_B T \tag{3.18}$$

where D is the diffusion constant from the diffusion model for Brownian motion, η is the friction coefficient associated with the viscous (velocity dependent) force exerted by the laser on the ion, k_B is the Boltzmann constant, and T is the temperature associated with the ion motion, see Section 3.4.2 for details. For the calculation, we treat the $S_{1/2} \leftrightarrow P_{1/2}$ transition of our ion as a two-level system, with $S_{1/2}$ as the ground state, $|g\rangle$, and $P_{1/2}$ as the excited state, $|e\rangle$.

Let us begin by deriving η from the average force exerted on an ion by laser light with frequency ω_L. This force is calculated by the average rate of momentum change [1],

$$\langle \hat{F} \rangle = \langle \frac{dp}{dt} \rangle = \hbar \vec{k} \Gamma \rho_{ee} = \hbar \vec{k} R_{opt} \tag{3.19}$$

where $\hbar\vec{k}$ is the momentum kick imparted by the laser, Γ is the linewidth of the atomic transition, ρ_{ee} is the probability of finding the ion in the excited state, and R_{opt} is the rate of optical pumping analogous to the spontaneous emission rate,

$$R_{opt} = \frac{\Gamma |\Omega_R|^2}{(\Gamma/2)^2 + (\delta - \vec{k} \cdot \vec{v})^2}, \tag{3.20}$$

where the Rabi frequency, $\Omega_R = \vec{d} \cdot \vec{E}/\hbar$, is dependent on the atomic dipole $\vec{d}$ and the laser electric-field $\vec{E}$, and $\delta = \omega_L - \omega$ is the laser detuning referenced to the atomic transition frequency. Eq. (3.19) holds only in the weak laser-field limit, $\Omega_R^2 \ll \Gamma^2$, where the force is not dominated by a radiatively broadened transition. In the case of a cold ion, we can expand the force in Eq. (3.19) for small velocities, $\vec{k} \cdot \vec{v} \ll 1$, to obtain

$$\langle \hat{F} \rangle \approx \hbar \vec{k} R_{opt}^{v=0} \left(1 + \frac{2\delta \vec{k} \cdot \vec{v}}{(\Gamma/2)^2 + \delta^2} \right). \tag{3.21}$$

The first term of Eq. (3.21) is a velocity-independent momentum kick which does not contribute to the cooling rate [1]. The second term of Eq. (3.21) provides a velocity-dependent cooling force, which may be parameterized as $\vec{F} = \eta m \vec{v}$ with η defined to be the friction coefficient,

$$\eta = \frac{2R_{opt}^{v=0}}{m} \frac{\hbar k^2 \delta}{(\Gamma/2)^2 + \delta^2}. \tag{3.22}$$

Our analysis continues with a calculation of the diffusion constant, D, under the Heisenberg-Langevin formalism. D describes the natural heating caused by spontaneous emission and is

defined to be the autocorrelation function of $\delta\hat{F}(t)$, defined as the fluctuating force resulting from Brownian motion of the ion,

$$2D\delta(t-t') = \langle \delta\hat{F}(t)\delta\hat{F}(t')^\dagger \rangle. \tag{3.23}$$

To understand $\delta\hat{F}(t)$, we start with the full force exerted on an ion by a plane-wave laser, $\Omega_R e^{ikx}$,

$$\hat{F} = i\hbar k\Omega_R^*\hat{\sigma}_{ge} - i\hbar k\Omega_R\hat{\sigma}_{eg} = \langle\hat{F}\rangle + \delta\hat{F}, \tag{3.24}$$

where $\hat{\sigma}_{ge} = |g\rangle\langle e|$. We decompose the full force into an average force, $\langle\hat{F}\rangle$, along with fluctuations around the mean, $\delta\hat{F}$. To find $\hat{\sigma}_{ge}$, we look to the Heisenberg-Langevin equation,

$$\frac{d\hat{\sigma}_{ge}}{dt} = \frac{i}{\hbar}[\hat{H}_{LI}, \hat{\sigma}_{ge}] - \left(\frac{\Gamma}{2} + i\delta\right)\hat{\sigma}_{ge} + (\hat{\sigma}_{ee} - \hat{\sigma}_{gg})\hat{f}(t) \tag{3.25}$$

where $\hat{f}(t)$ is a stochastic force which follows properties of the Langevin noise term, i.e. $\langle\hat{f}(t)\rangle = 0$ and $\langle\hat{f}(t)\hat{f}(t')^\dagger\rangle = \delta(t-t')$, and the Hamiltonian for the laser-ion interaction is given by

$$\hat{H}_{LI} = -\hbar\Omega_R^*\hat{\sigma}_{ge} - \hbar\Omega_R\hat{\sigma}_{eg} \tag{3.26}$$

Since we are interested in times near equilibrium, we care only about processes much slower than Γ, meaning we may approximate $\frac{d\hat{\sigma}_{ge}}{dt} \approx 0$ in solving for $\hat{\sigma}_{ge}$,

$$\hat{\sigma}_{ge} = \frac{(\hat{\sigma}_{ee} - \hat{\sigma}_{gg})\hat{f}(t)}{\Gamma/2 + i\delta} + \frac{i}{\hbar(\Gamma/2 + i\delta)}[\hat{H}_{LI}, \hat{\sigma}_{ge}]. \tag{3.27}$$

As we insert $\hat{\sigma}_{ge}$ into Eq. (3.24), notice that only the fluctuating terms with $\hat{f}(t)$ contribute to the fluctuating force, $\delta\hat{F}(t)$,

$$\delta\hat{F}(t) = i\hbar k\Omega_R^*\frac{(\hat{\sigma}_{ee} - \hat{\sigma}_{gg})\hat{f}(t)}{\Gamma/2 + i\delta} - i\hbar k\Omega_R\frac{(\hat{\sigma}_{ee} - \hat{\sigma}_{gg})\hat{f}(t)^\dagger}{\Gamma/2 - i\delta}. \tag{3.28}$$

Finally, we may calculate the autocorrelation function of the fluctuating force as

$$\langle\delta\hat{F}(t)\delta\hat{F}(t')^\dagger\rangle = (\hbar k)^2\frac{2\Gamma|\Omega_R|^2}{(\Gamma/2)^2 + \delta^2}\delta(t-t'), \tag{3.29}$$

and derive a diffusion constant given by

$$D = (\hbar k)^2\frac{\Gamma|\Omega_R|^2}{(\Gamma/2)^2 + \delta^2} = (\hbar k)^2 R_{opt}^{v=0}. \tag{3.30}$$

With η the friction coefficient from Eq. (3.22), calculated assuming small laser power, and D the diffusion constant from Eq. (3.30), we may solve the Einstein relation for the equilibrium temperature,

$$k_B T = \frac{\hbar((\Gamma/2)^2 + \delta^2)}{2\delta}. \tag{3.31}$$

Note that the temperature is minimized when $\delta = \Gamma/2$, giving an optimized equilibrium temperature dependent only on the linewidth of the excited state. Consequently the Doppler cooling limit is given by

$$k_B T = \frac{\hbar\Gamma}{2}. \tag{3.32}$$

We may expand our one-dimensional analysis above to a generalized geometry by following the work from Leibfried et al. [1] and Stenholm [38] to arrive at a weak-field Doppler cooling temperature limit,

$$k_B T = \frac{\hbar\Gamma}{4}(1+\xi), \tag{3.33}$$

with geometry factor ξ. In the one-dimensional case, where the spontaneously emitted photons may only point directly towards or away from the laser beam propagation, $\xi = 1$, and Eq. (3.33) matches Eq. (3.32). In the more realistic case, photons may be emitted isotropically into 3-D space, which effectively slows the momentum diffusion in the laser cooling direction. Such an effect may be accounted for by setting the geometrical factor $\xi = 2/5$.

3.4.2 Temperature

Of course, as the motional states of ions are quantized, it does not make sense to assign a temperature to a single realization of the ion motion. Instead, it is more accurate to say that the measurement of ion temperature requires an accrual of statistics on the ion's number state, $\hat{N}$. Then from that information, we extract an average occupation of the the motional quantum number, $\bar{n}$. Assuming the ion is in a thermal state, i.e. at thermal equilibrium, we can then interpret a temperature, T from this $\bar{n}$ measurement. We know that when an ion is at thermal equilibrium with an external bath of temperature, T, the distribution of its motional states, $|n\rangle$, is proportional to the Boltzmann factor, $e^{-n\hbar\omega/k_B T}$. This allows us to relate temperature, T, and the mean motional occupation, $\bar{n}$,

$$k_B T = \frac{\hbar\omega_t}{\ln\left(\frac{\bar{n}+1}{\bar{n}}\right)}. \tag{3.34}$$

At this juncture, it may be helpful to provide some sense of the temperatures we will be dealing with in this thesis. The $S_{1/2} \leftrightarrow P_{1/2}$ transition has a linewidth of roughly 20 MHz, meaning our final Doppler cooled ions reach $T \approx 0.3$ mK. From Eq. (3.34), we see that this temperature corresponds to average occupations of $\bar{n} = 6$ quanta, as we typically operate our traps with $\omega_t = 1$ MHz.

3.4.3 Resolved-sideband cooling

The Doppler cooling temperature limit makes intuitive sense. However, there are quite a few techniques, aptly termed sub-Doppler cooling, that provide cooling beyond the Doppler

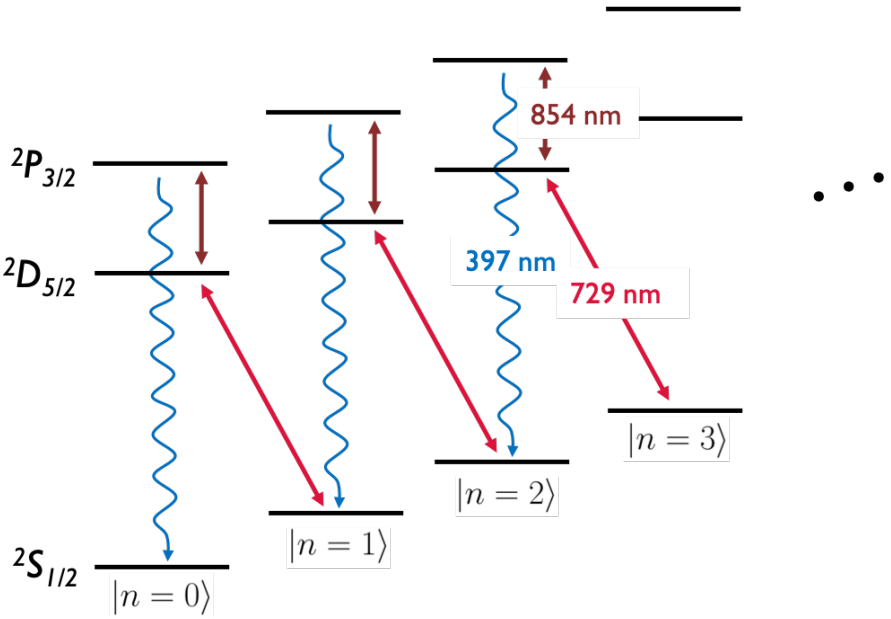

Figure 3.6: Relevant sideband cooling energy levels and transitions. Solid arrows indicate driven transitions, and squiggly arrows indicate spontaneous decay. The cooling process can be followed from right to left, ending at $|S, n=0\rangle$, where the 729 nm light is no longer resonant with a motional transition.

limit by taking advantage of the internal energy level structure of ions. One such scheme is resolved-sideband cooling. As the name suggests, this method works in the regime where the effective linewidth of the electronic transition, Γ, is narrower than the motional trap frequency, ω_t. In addition to the $\Gamma \ll \omega_t$ requirement, it is also beneficial for the ion to start in the Lamb-Dicke regime, $\eta^2(2\bar{n}+1) \ll 1$, as this promotes the ion to predominantly decay on the carrier transition, preventing unwanted transitions to different motional states during spontaneous emission. Because of this, sideband cooling is usually performed after an initial Doppler cooling step, which initializes the ion into the Lamb-Dicke regime.

From Section 3.2.3, we have seen that sideband transitions can change the motional state of the ion. We can take advantage of these transitions to cool the ion to its motional ground state. The scheme for resolved-sideband cooling is shown in Fig. 3.6, where we have ignored the effects of heating. The process starts with an ion in the $|S, n\rangle$ state; then a π-pulse first-order red sideband transition is applied with a laser frequency of $\omega_l = \nu - \omega_t$, where ν is the $S_{1/2} \leftrightarrow D_{5/2}$ atomic transition. This operation brings the ion into the $|D, n-1\rangle$ state. From there, an 854 nm light then excites the ion into the $P_{3/2}$ state, where it quickly decays back to the $|S, n-1\rangle$, thus completing a cycle of sideband cooling. At the end of a single cycle, we have reduced the motional state of the ion by one quanta. Successive cycles of sideband cooling will eventually bring the ion into the motional ground state, $|S, 0\rangle$. From here, there are no longer any transitions at the laser frequency, ω_l, allowing the population to accumulate into the $|S, 0\rangle$ state.

3.5 Temperature measurement

From Sec. 3.4.2, we saw that the temperature can be described by an average occupation of motional states, $\bar{n}$, assuming a thermal distribution. In this section we will provide background on how to experimentally measure $\bar{n}$ of an ion.

3.5.1 Sideband spectroscopy

The first method for measuring $\bar{n}$ takes advantage of resolved sidebands in the Lamb-Dicke regime. With the proper laser detuning, δ, we can drive red sideband transitions and blue sideband transitions as described in Eq. (3.16) and Eq. (3.17), respectively. Then the time-evolution of the excitation probabilities when driving these sidebands is given by

$$P_D^{\text{rsb}}(t) = \frac{1}{2}(1 - \sum_{n=1}^{\infty} P_n \cos(2\Omega_{n,n-1}t)) = \sum_{n=1}^{\infty} P_n \sin^2(\Omega_{n,n-1}t), \tag{3.35}$$

$$P_D^{\text{bsb}}(t) = \frac{1}{2}(1 - \sum_{n=0}^{\infty} P_n \cos(2\Omega_{n,n+1}t)) = \sum_{n=0}^{\infty} P_n \sin^2(\Omega_{n,n+1}t), \tag{3.36}$$

where P_n is the occupation probability of the motional state $|n\rangle$ at time $t = 0$.

Assuming a thermal distribution of motional states, we know that P_n is given by [39, 40]

$$P_n = \frac{\bar{n}^n}{(\bar{n}+1)^{n+1}}. \tag{3.37}$$

Now for any time, t, we can compare the populations of the red and blue sidebands with the ratio

$$\frac{P_D^{\text{rsb}}(t)}{P_D^{\text{bsb}}(t)} = \frac{\sum_{n=1}^{\infty} \frac{\bar{n}^n}{(\bar{n}+1)^{n+1}} \sin^2(\Omega_{n,n-1}t)}{\sum_{n=0}^{\infty} \frac{\bar{n}^n}{(\bar{n}+1)^{n+1}} \sin^2(\Omega_{n,n+1}t)} = \frac{(\frac{\bar{n}}{\bar{n}+1}) \sum_{n=0}^{\infty} \frac{\bar{n}^n}{(\bar{n}+1)^{n+1}} \sin^2(\Omega_{n+1,n}t)}{\sum_{n=0}^{\infty} \frac{\bar{n}^n}{(\bar{n}+1)^{n+1}} \sin^2(\Omega_{n,n+1}t)} = \frac{\bar{n}}{\bar{n}+1}. \tag{3.38}$$

From this, we can see that a measurement of $\bar{n}$ consists of measuring the ratio between the on-resonant excitation probabilities of the red and blue sidebands [41],

$$\bar{n} = \frac{R}{1-R}\ ,\ R = \frac{P_D^{\text{rsb}}(t)}{P_D^{\text{bsb}}(t)}. \tag{3.39}$$

Experimentally, we perform this measurement by probing the excitation probability as a function of frequency, centered around the sidebands $\nu \pm \omega_t$. An example of temperature measurement via sideband spectroscopy is shown in Fig. 3.7, where we plot the red and blue sideband spectra for various ion tempartures. We extract the on-resonant (peak) excitation of both red and blue sideband transitions with Gaussian fits, and then take the appropriate

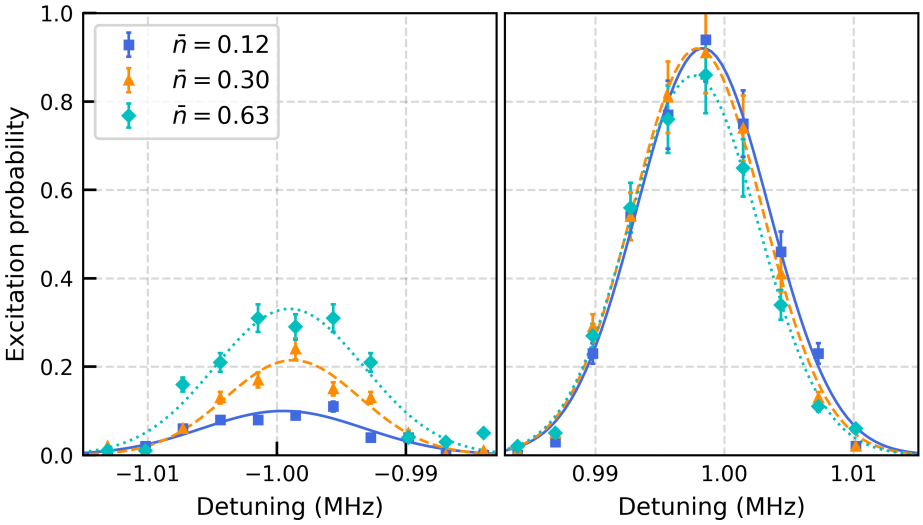

Figure 3.7: Demonstration of temperature measurement using sideband spectroscopy for thermal states with $\bar{n} = 0.12, 0.30,$ and 0.63 shown in blue, orange, and cyan, respectively. The left (right) panel displays the red (blue) sideband excitation probability as a function of the laser detuning from $\nu - \omega_t$ ($\nu + \omega_t$). Data is taken near the *pi*-time of the first order sideband Rabi flops, with solid lines as Gaussian fits to the data. From the peak values of the fit, the mean motional occupation, $\bar{n}$, for each data set is calculated at $2\pi \times 1$ MHz trap frequency. Error bars are based on binomial statistics for 100 measurement repetitions and represent one standard deviation uncertainty.

ratio to calculate tempratures of $\bar{n} = 0.12, 0.30,$ and 0.63. The asymmetry of the sideband excitations is largest when the ion is near the motional ground state. As $\bar{n}$ increases, both red and blue sidebands tend towards peak excitation probabilities of 0.5.

Although this method is commonly used and fairly easy to measure, there are a few considerations to take into account. The first is that this method becomes insensitive when $\bar{n}$ exceeds ~ 2 quanta [6]. For larger $\bar{n}$, statistical errors (typically 10% for 100 repeated experiments) on the extracted P_D^{rsb} and P_D^{bsb} values imply unphysical values of the ratio $P_D^{\text{rsb}}/P_D^{\text{bsb}}$, which must be lower than 1 for a thermal state. Any measurements of $\bar{n} \gtrsim 2$ should be performed with alternate methods. Secondly, we can see from Eq. (3.38) that the ratio is independent of the pulse length, t, but that does not mean the pulse length is unimportant. For the best signal to noise ratio, the pulse length should be set near or slightly before the π-time of the blue sideband transition, i.e. the first maximum of the Rabi oscillation [1]. Lastly, this method assumes a thermal distribution for the ion motional states. Consequently, this ratio method will give inaccurate results if the ion is in a nonthermal state, whether accidentally [42, 43] or purposely.

One method for measuring higher $\bar{n}$ values is to use higher-order sidebands. The general idea is similar to the first-order sideband case discussed above, but now generalized for the

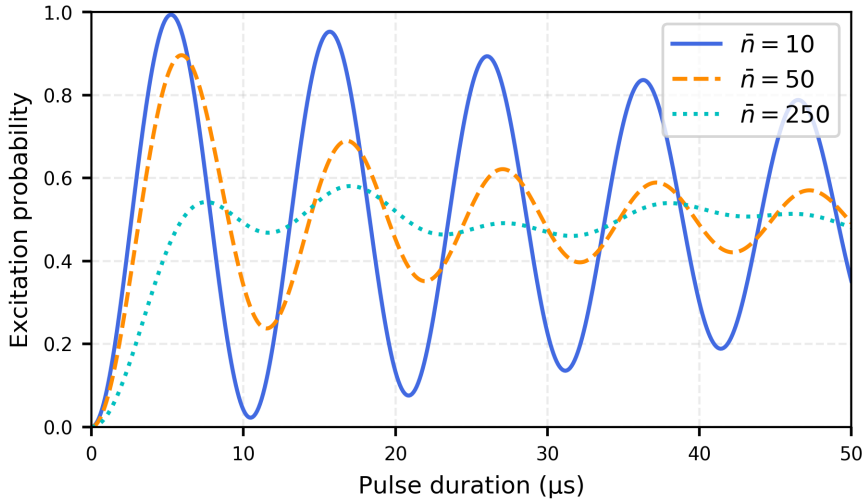

Figure 3.8: Simulated carrier Rabi flops of thermal states with $\bar{n} = 10, 50,$ and 250 shown in blue, orange, and cyan, respectively. The bare Rabi frequency of all the simulations is set to, $\Omega_0 = 2\pi \times 10$ μs. Heuristically, increasing $\bar{n}$ results in a slower effective Rabi frequency and a faster perceived contrast decay.

k-th order sidebands,

$$\frac{P_D^{\mathrm{rsb}_k}(t)}{P_D^{\mathrm{bsb}_k}(t)} = \left(\frac{\bar{n}}{\bar{n}+1}\right)^k. \tag{3.40}$$

This method is sensitive to $\bar{n} \sim k$ [7].

3.5.2 Rabi oscillations

We can also extract $\bar{n}$ from the time-domain by analyzing Rabi flops at fixed detunings. Let us focus first on the carrier Rabi oscillations, with time-dependent excitation described by

$$P_D^{car}(t) = \sum_{n=0}^{\infty} P_n \sin^2(\Omega_{car} t). \tag{3.41}$$

where P_n for a thermal state is given by Eq. (3.37), and Ω_{car} is a state-dependent Rabi frequency which follows Eq. (3.15). To help visualize the carrier transition time-evolution, we show simulated Rabi flops of thermal states, with $\bar{n} = 10, 50,$ and 250, in Fig. 3.8. Qualitatively, we see a decay of contrast over time, which is caused by the dephasing of the Rabi flops for various $|n\rangle$ fock states that compose the thermal state. Due to this effect, ions with larger $\bar{n}$ will exhibit faster contrast decay, shown in Fig. 3.8, as they have a larger spread in their harmonic oscillator quantum number. Quantitatively, we can extract $\bar{n}$ from a fit to the carrier Rabi flop. An interesting note is that in the absence of other decoherence

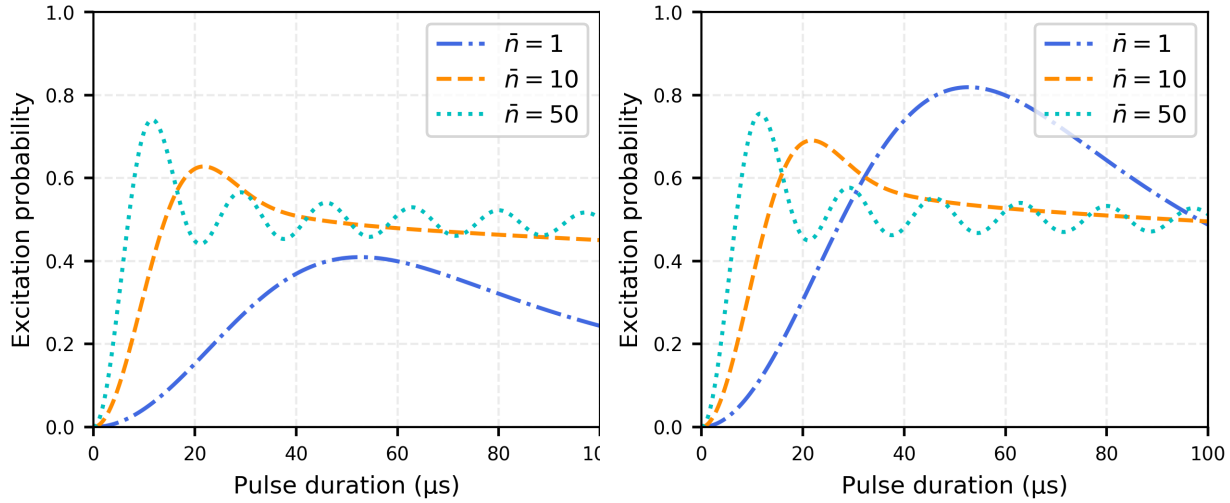

Figure 3.9: (Left) Simulated first-order red sideband Rabi flops plotted for $\bar{n} = 1, 10,$ and 50 in blue, orange, and cyan, respectively. (Right) Simulated first-order blue sideband Rabi flops also for $\bar{n} = 1, 10,$ and 50 in blue, orange, and cyan, respectively. All simulations use $\Omega_0 = 2\pi \times 10$ μs. In contrast to the carrier Rabi flops, the effective sideband oscillations quicken with increasing $\bar{n}$.

sources, there will be a revival of the carrier Rabi flop contrast if we probe for long enough times.

Following the same logic, we can also utilize sideband excitation flops to fit for $\bar{n}$. Fig. 3.9 shows the time-evolution of first-order red sideband (left) and first-order blue sideband (right) excitations for various $\bar{n}$ values. To generate accurate fits of these sideband excitations, it is essential to possess prior knowledge of the bare Rabi frequency, Ω_R. Thus in practice, we first perform carrier excitation fits to extract Ω_R.

In general, the method of analyzing Rabi oscillations is sensitive to larger $\bar{n}$ than the sideband asymmetry method described in Section 3.5.1. Of course, this technique also has limitations. When $\bar{n} \gtrsim 500$ quanta, the carrier transition rapidly dephases, leaving little information to be extracted from the dynamics. So in the case of large $\bar{n}$, it is prudent to probe higher-order sideband transitions. In addition, the time-evolution of sideband transitions is more appropriate for characterizing the motional occupation of non-thermal states, as the Rabi frequency spread has a smaller dependence on n. The Rabi flop method we have discussed is most accurate when the laser is well aligned with a single ion motional mode. When the laser has projection onto other motional modes, Eq. (3.41) must be modified to include the effects of those modes. Specifically, the carrier Rabi frequency from Eq. (3.15) becomes [5]

$$\Omega_{car} \approx \Omega_R \prod_s (1 - \eta_s^2 n_s), \tag{3.42}$$

where s denotes the motional modes. We must account for these additional parameters in

our fit of Eq. (3.41) to generate accurate measurements of the temperature.

Chapter 4

Four-RF-electrode (elevator) trap

In this chapter, we introduce a novel surface trap design, the four-RF-electrode trap, which we colloquially term the "elevator" trap. This trap design features RF fields that provide confinement in the trap plane, but cancel along the vertical axis which is perpendicular to the trap surface. The ion trapping height and vertical potential are fully controlled with DC fields, simplifying vertical shuttling, hence the "elevator" moniker, and allowing for trapping of vertical ion strings. With this design, we have demonstrated trapping at heights ranging from 50 to 300 µm above the trap surface. We also discuss potential applications of the trap design in quantum control, such as moving ions in and out of control fields [44], and electric field sensing [8, 9].

4.1 Trap design

Our trap design takes inspiration from the cross-sectional cut of a conventional four-rod Paul trap [16]. Fig. 4.1 shows a false-color photograph of the trap we fabricated and used in this thesis. Four RF electrodes measuring 290 × 290 µm^2 each are centered on the corners of a 560 × 560 µm^2 square while nine DC electrodes are sized and positioned to optimize control of static dipole and quadrupole fields. All other areas on the chip are grounded. Further details of the trap fabrication are outline in Section 5.1.2.

4.1.1 Trapping modes

The elevator trap can be operated in two configurations: as a point trap or as a vertical-linear trap.

Point trap configuration

In the point trap configuration, all four RF electrodes are driven with the same amplitude and phase, generating three-dimensional RF confinement with a single RF-null trapping point. The position of the RF null is independent of the magnitude of RF drive and dependent only

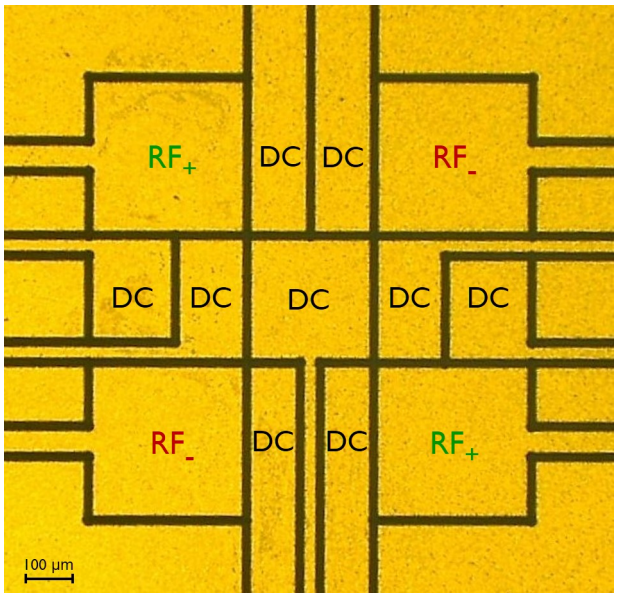

Figure 4.1: False-color microscope image of the microfabricated elevator trap. Static voltages are applied to electrodes labeled DC, and oscillating voltages are applied to RF electrodes, labeled as $RF_{\pm}$ according to the signal phase.

on the geometry of the electrodes. Fig. 4.2 shows the equipotential lines of the pseudopotential in this configuration with applied RF voltage of 100 V_{pp}. From these simulations, we see that this point trap configuration has an RF null point, i.e. trapping height, located 245 µm above the center of the trap. As the three-dimensional trapping is completely set by the RF fields, the principal axes of oscillation are composed of the vertical $\hat{z}$-axis and two other axes which are inherently degenerate in the xy-plane. We apply quadrupole DC fields to break this degeneracy and set the orientation of the planar principal axes along the $\hat{x}$-axis and $\hat{y}$-axis. With an RF drive frequency of $\Omega_{RF} = 2\pi \times 20$ MHz and applied voltage of 100 V_{pp}, we expect trap frequencies of $\omega_x, \omega_y = 2\pi \times 292$ kHz and $\omega_z = 2\pi \times 597$ kHz. Experimentally, the main purpose of ion measurements in the point trap was to demonstrate the validity of our electric-field simulations. Additionally, trapping in this configuration gave us confidence that the entirety of the physical trapped ion system functioned properly, including the RF and DC electronics and connections, optics paths, vacuum system, and control software.

Vertical-linear configuration

In the vertical-linear configuration, we employ an out-of-phase RF drive where one diagonal pair of RF electrodes (RF_+) is driven with a sinusoidal voltage, while the other diagonal pair (RF_-) is driven with a voltage of the same amplitude, but opposite phase. This drive is physically realized with a $\lambda/2$ resonator detailed in Section 5.3.3.

The out-of-phase RF drive of the vertical-linear trap produces an effective potential, or pseudopotential [1], originating from time-averaged RF fields, as shown in Fig. 4.3. The

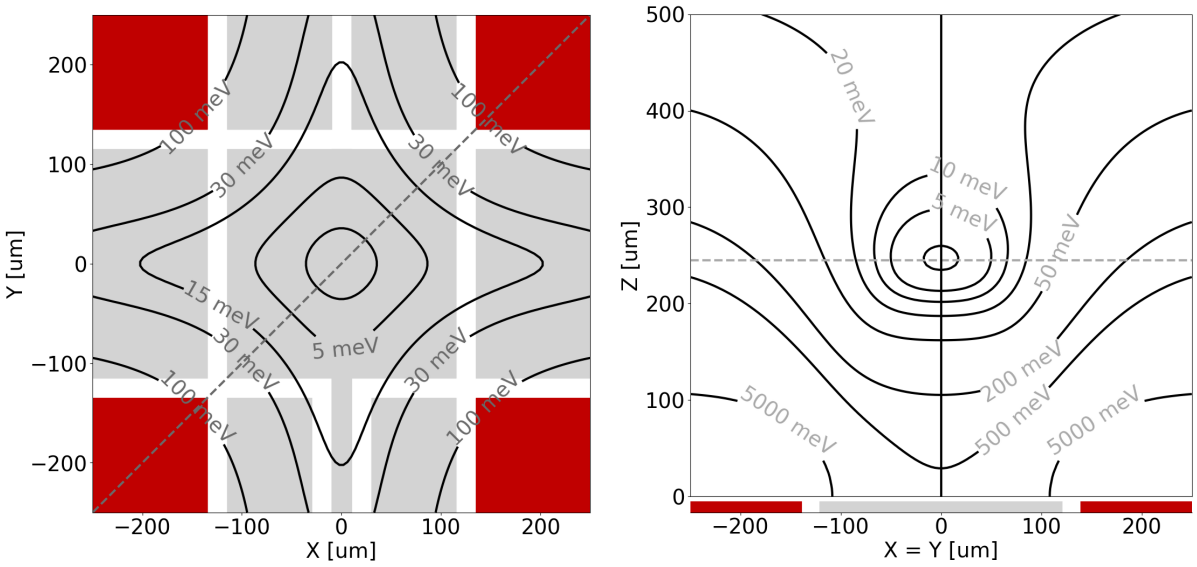

Figure 4.2: (Left) Top-down view of xy-plane RF pseudopotentials at a height of $z = 245$ µm, with electrode geometry shown for reference. The RF electrodes, shown in red, are driven with signals of equivalent amplitude and phase. The DC electrodes are shown in grey. (Right) Side view of RF pseudopotentials. The grey dashed lines in (left) and (right) denote the position of the cross-sectional slice in (right) and (left), respectively.

calculation of the potential assumes a strictly two-dimensional trap geometry, which can be solved analytically [45] taking into account each electrode's solid-angle with respect to the ion location. Our simulations assume an RF drive frequency $\Omega_{\mathrm{rf}} = 2\pi\times18$ MHz and a peak-peak voltage $V_{\mathrm{pp}} = 200$ V. Panel (left) in Fig. 4.3 displays the RF pseudopotential lines in the xy-plane at a height of 175 µm, showing quadrupole confinement with an RF null at the trap center, $x = y = 0$. The trap design is shown in the background for reference. Fig. 6.1 (right) shows a cross-section of the pseudopotential in the plane defined by the dashed grey line in panel (left) and the vertical z-axis. Due to the symmetry of the RF-electrode pairs, the RF fields fully cancel along the vertical z-axis at $x = y = 0$, creating an RF-null axis perpendicular to the surface. Confinement in this direction can be achieved with DC potentials, which allows tuning of the trapping location along the vertical axis without introducing excess micromotion.

4.2 Trap operation

We operate the trap in an ultra-high vacuum chamber at a pressure $< 1 \times 10^{-10}$ mbar. An RF voltage at a frequency of $\Omega_{RF} = 2\pi\times18.1$ MHz is generated with a signal generator (Rohde & Schwartz SMB 100A), amplified (mini-circuits ZHL-5W-1) and applied to the RF electrodes through an inductively coupled toroidal half-wave resonator. A beam of calcium

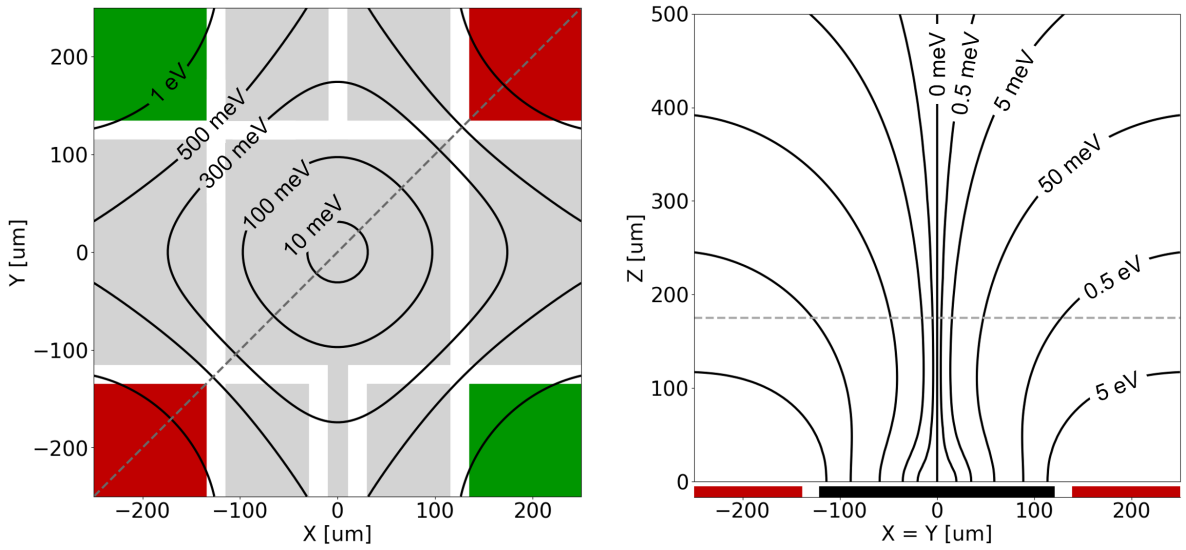

Figure 4.3: (Left) Top-down view of xy-plane RF pseudopotentials at a height of $z = 175$ µm, with electrode geometry shown for reference. The green RF electrodes are driven out-of-phase with respect to the red RF electrodes. (Right) Side view of RF potentials. The grey dashed lines in (left), (right) denote the position of the cross-sectional slice in (right), (left), respectively.

atoms is propagated through the trapping region from a resistively heated oven filled with macro-granules of calcium (Ca). Neutral ^{40}Ca atoms are selectively ionized in a two-step process using laser light at 422 and 375 nm, see Section 3.1.1.

A pair of red-detuned 397-nm and 866-nm beams addresses the λ-system consisting of the electronic states $S_{1/2} - P_{1/2} - D_{3/2}$ and cools the ion motion. Ion fluorescence at 397 nm is detected by a photomultiplier tube and used for determining whether the ion is in the $S_{1/2}$ or the $D_{5/2}$ state, see Section 3.3. In order to cool the planar motional mode, the 397-nm beam propagates in the plane parallel to the trap surface. Concurrently, the vertical motional mode is cooled with the near-vertical 866-nm beam. A 729-nm beam, which addresses the dipole-forbidden transition $S_{1/2} - D_{5/2}$ connecting our qubit states, is used for ion spectroscopy and sideband cooling. It can be switched between two propagation directions, one in the trap plane and one vertical to the trap surface.

With this configuration, we have demonstrated trapping of single ions at heights between 50 µm and 300 µm. The experimentally limiting factor for operation at both extremes is the high voltage required on the RF electrodes. At low trapping heights the trap harmonicity also decreases, resulting in ion lifetimes decreasing from several hours at 110 µm height to several minutes at 50 µm for the same secular frequencies. Typical secular trap frequencies range from $\omega_z = 2\pi \times 0.4$ MHz to $2\pi \times 1.2$ MHz and $\omega_x, \omega_y = 2\pi \times 0.6$ MHz to $2\pi \times 2.0$ MHz. The degeneracy between the two planar modes is lifted by applying a suitable DC quadrupole, resulting in a typical splitting of $|\omega_x - \omega_y|/\omega_x \sim 0.1$. Additionally, changing

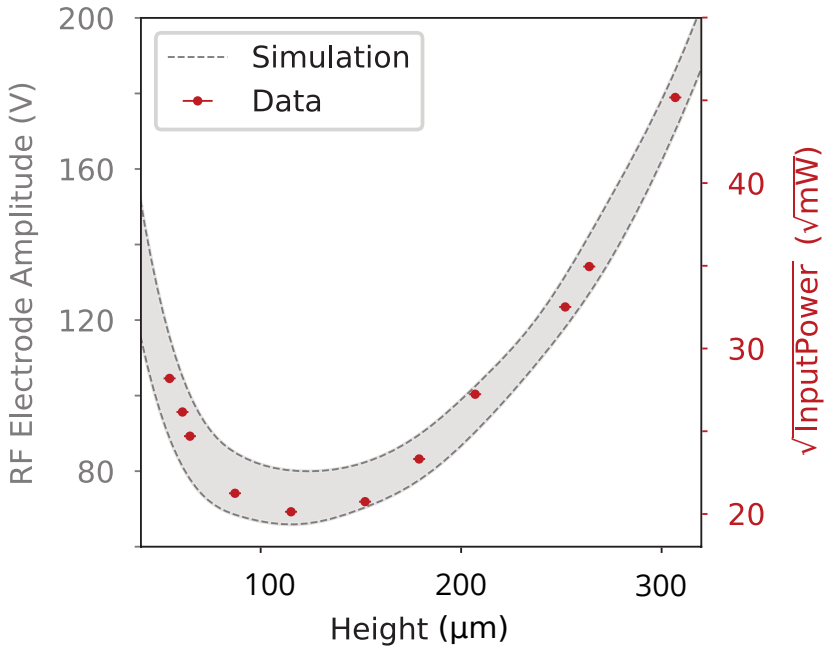

Figure 4.4: RF voltages required to achieve a planar secular frequency of $2\pi \times 1$ MHz as a function of the ion height. The grey band indicates the simulated voltages for vertical tilt angles of 0° (lower limit) and 4° (upper limit). Red dots show the square root of the power output from the rf signal generator applied to the rf resonator-trap system. Error bars correspond to one s.d. uncertainty in the ion height.

the DC quadrupole values also controls the orientation of the principal axes [46]. This ability is important as it allows us to slightly tilt the vertical mode into the trap plane, thus creating non-zero projection with the in-plane 397-nm laser which improves cooling of the near-vertical mode. Voltages on the DC electrodes are typically on the order of a few volts at intermediate trapping heights and increase to greater than 10 V for lower heights close to 50 µm and higher heights close to 300 µm.

4.2.1 RF drive

While there is no RF confinement along the vertical axis, the RF field strength in the plane of the trap surface depends on the distance to the surface. This effect can be seen in Fig. 4.3(right) where the equipotential lines are closest together around 110-µm height. Experimentally, we observe this dependence by trapping a single ion at various ion-electrode distances and comparing the RF-voltage needed to create a planar confinement corresponding to a fixed secular frequency, $2\pi \times 1$ MHz in this case. Data and simulation of our applied RF voltage and power are displayed in Fig. 4.4. The grey shaded region indicates the simulated RF voltage amplitude, with the lower and upper limits determined by a vertical tilt angle of 0° and 4°, respectively, which are typical parameters in our measurements. The data points

(red dots) show the square root of the power output from the RF signal generator, which is routed, via the amplifier, to the RF resonator-trap system. The ion trapping height is determined experimentally by maximizing ion fluorescence in the vertical direction and then translating the $\sim$ 5-µm wide 397-nm beam until it scatters from the center of the trap, taking care to avoid backlash of the motorized translation stage. The uncertainty in the ion-surface distance is estimated at ± 1.5 µm, given by the precision of repeated measurements. Overall, data and simulation agree well.

4.2.2 DC multipoles

Up to now, we have focused on the details of trapping via RF fields in the elevator trap, but without the DC fields, we cannot encompass the full three-dimensional trapping scheme. Here, we expand upon the requirements of the static DC fields and their importance in trapped ion operation. For instance, operation of the elevator trap in the out-of-phase configuration leads to cancellation of RF fields along the central vertical axis, where confinement must be established via DC fields. Additionally, static fields are used for electric dipole compensation and electric quadrupole tuning. The former allows for compensation of micromotion induced by stray electric-fields; the latter enables simple fine tuning of the trap frequencies and principle axes.

DC multipole expansion

First, we must understand the relation between DC fields and the harmonic part of the trapping potential. The approximate static-field solution to Laplace's equation in Cartesian coordinates, is given by the potential

$$\begin{aligned}\Phi_{DC}(x,y,z) \approx & - E_x \cdot (x) - E_y \cdot (y) - E_z \cdot (z) \\ & + U_1 \cdot \left(\frac{x^2 - y^2}{2}\right) + U_2 \cdot \left(\frac{2z^2 - x^2 - y^2}{2}\right) \\ & + U_3 \cdot \left(\frac{xy}{2}\right) + U_4 \cdot \left(\frac{yz}{2}\right) + U_5 \cdot \left(\frac{xz}{2}\right) + O(r^3).\end{aligned} \tag{4.1}$$

This decomposition is derived from the spherical harmonics expansion of the potential up to $l = 2$ [47], where l is the polynomial degree of the spatial coordinates. There are 3 electric dipole terms with coefficients E_x, E_y, and E_z, which we choose to have units of V/mm, along with 5 electric quadrupole terms with coefficients, U_1, U_2, U_3, U_4, and U_5, that are chosen to have units of V/mm^2. Together, these 8 coefficients are termed as the multipole coefficients of the expanded potential.

Intuition on the functionality of these multipoles may be gleaned by looking at example use cases. The E_x, E_y, and E_z are mainly used to move the ion position in x, y, and z, respectively. With these controls, we can shift the ion into the RF null of the trap, leading to a reduction in micromotion. The U_1 and U_3 terms generate different couplings between the radial modes, including the ability to alter radial trap frequencies, avoiding degeneracies,

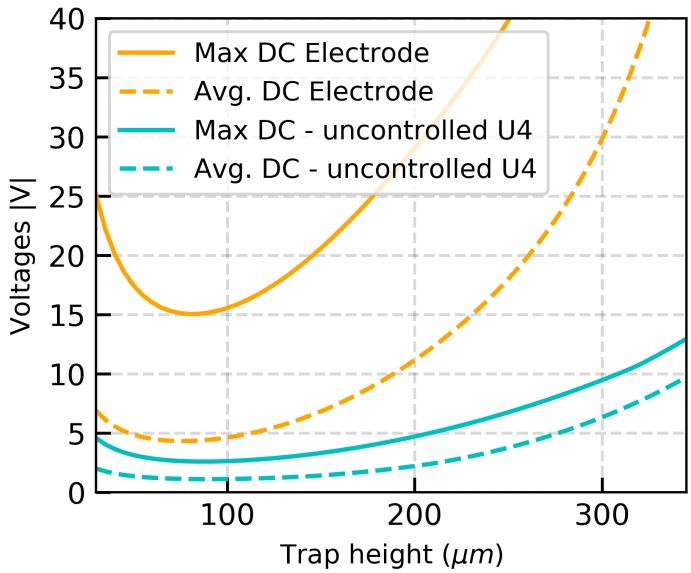

Figure 4.5: DC voltages required to establish $2\pi \times 1$ MHz trap frequency in the vertical direction. The results of two control schemes are shown. The first scheme, shown in orange, applies full control of all 8 multipoles with $l \leq 2$ of the DC potential, see Eq. (4.1). Explicitly, $U_2 = 8.18$ V/mm^2 and all other multipoles are set to zero. The solid line represents the largest voltage applied to any of the DC electrodes, the dashed represents the average of all DC voltages. The second scheme, shown in cyan, relinquishes control of the U_4 multipole. This leads to a reduction in both the maximum single electrode voltage (solid line) and the average voltage across the electrodes (dashed line).

and rotating the principal axes in the radial xy-plane. U_2 is the sole multipole that can set a confining potential in the axial, z, direction. And finally, U_4 and U_5 both provide the ability to 'tilt' the principal axes away from the standard xyz-basis, along either the yz or xz planes, respectively.

DC voltage limits

As a design concept, it is important to discern the limits of the DC field control in our elevator trap system. The DC voltages are generated with a multi-stage digital-to-analog converter (DAC) system, which takes digital input from an FPGA and converts to analog voltages with DAC chips, which have $(-10, 10)$ V range. As we occasionally require voltages larger than ± 10 V, the DAC output feeds into an amplifier board that expands the range to $(-40, 40)$ V. Under normal operation, the elevator trap has access to 9 DC electrodes, properly positioned to independently manipulate the 8 DC multipoles, i.e. up to quadratic terms in the potential. Unfortunately, electrode '18' was burnt during the assembly process, see Section 5.2.1, and we were forced to short this electrode directly to the trap ground, leaving us with 8 controllable DC electrodes.

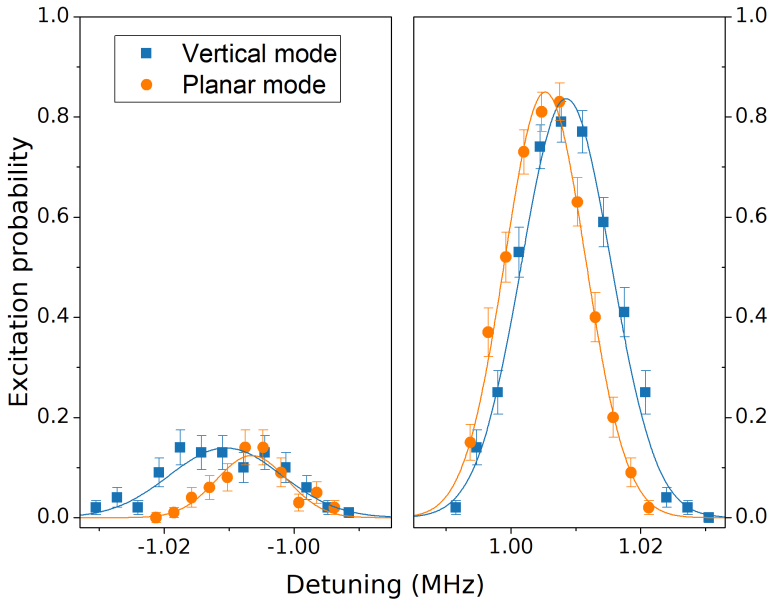

Figure 4.6: Demonstration of ground state cooling of vertical and planar modes at a trapping height of 114 µm. The left (right) panel displays the red (blue) sideband excitation probability. Data for the vertical (planar) mode are shown as blue squares (orange circles), solid lines are Gaussian fits to the data. The mean phonon numbers for the planar and vertical modes are 0.17(3) and 0.20(3) quanta at $2\pi \times 1$ MHz, respectively. Error bars are based on binomial statistics for 100 measurement repetitions and represent one s.d. uncertainty.

Technically, the 8 remaining DC electrodes provide enough degrees of freedom to fully control the 8 static multipoles. However, achieving modest trap frequencies of $2\pi \times 1$ MHz requires voltages exceeding the ± 40 V limit imposed by the DAC outputs. Rather than attempt to implement additional amplifier stages to the DAC, which may add noise, we instead release control of the U_4 multipole, which is largely affected by electrode '18'. This multipole is relatively unimportant for our experimental measurements.

With U_4 allowed to run free, the overall magnitude of the electrode voltages is reduced to workable conditions. Fig. 4.5 shows the effect of toggling U_4 as a controlled or free parameter. When controlled, the full multipole set is given by $U_2 = 8.18$ V/mm^2, with all other multipoles tuned to zero. In this scheme, trapping ions at heights above 250 µm require individual electrode voltages exceeding the 40 V threshold achievable with our DAC amplifier setup. We find a resolution to this dilemma by setting the U_4 multipole as a free parameter. The result is an order of magnitude reduction in the voltage on all electrodes, allowing us to establish vertical trap frequencies of up to $2\pi \times 2$ MHz even at the extreme trapping height of 300 µm.

4.2.3 Ground state cooling

Finally, we demonstrate ground state cooling of the ion's motion in this four-rf-electrode trap which is relevant for sensing and high-fidelity quantum control applications. Both vertical and planar motional modes are of interest for future experiments, so we perform two sets of measurements, one for the planar modes and, switching the direction of the 729-nm laser to be perpendicular to the trap surface, one for the vertical mode. We operate at a trapping height of 114 µm and tune the secular frequency to $\sim 2\pi \times 1$ MHz in both cases. During the cooling sequence we Doppler-cool on the $S_{1/2} - P_{1/2}$ transition for 2 ms, then perform sideband-cooling using the first-order secular sideband of our qubit transition for six 1-ms cycles. A measurement of the ratio of Rabi frequencies for the red and blue sidebands can be used to calculate the mean phonon number for the motional mode [1], see Section 3.5.1. Figure 4.6 displays measurements of the red (left panel) and blue (right panel) secular sidebands for the planar (orange circles) and vertical (blue squares) modes, together with Gaussian fits as solid lines. We obtain mean mode occupations of $\bar{n}_{\text{planar}} = 0.17(3)$ and $\bar{n}_{\text{vertical}} = 0.20(3)$ phonons, corresponding to a ground state occupation of 0.85 and 0.83, respectively. The achievable ground state occupation at this trapping height is limited by the intensity of the 729-nm light used for sideband cooling in conjunction with heating rates of several hundred quanta per second.

4.3 Applications

The ability to tune the ion trapping height by changing the DC fields opens up new opportunities for sensing and quantum information applications. Of immediate interest are studies of electric field surface noise as a function of ion-surface distance. The distance scaling of the spectral noise density, S_E, is an important indicator for the type and origin of surface noise [6]. Recently, two studies independently showed a d^{-4} power-law scaling for an electroplated gold surface trap [48] and a sputtered niobium trap [49]. We have also measured the distance scaling in our Al-Cu elevator trap by tuning the ion-electrode distance from 50 µm to 300 µm [50]. Moreover, we take advantage of the control and access to motional modes both vertical and horizontal to the electrode surface, which delivers additional information as to the characteristics of the surface noise.

Beyond studies of the environment noise, we foresee applications in quantum information science where the proximity of the ion to control fields is important. As with the common linear five-wire trap design, shuttling of ions can be used to spatially separate readout and control regions above a surface trap chip. For instance, when large magnetic field gradients for microwave gates are required [51, 52, 53] the ion can be brought closer to the surface for the duration of a quantum gate while readout beams are kept further away to avoid scattering from the surface and possible charging effects [54, 55, 56]. Vertical ion shuttling also has advantages for ion loading, which can be performed further away from the surface to avoid coating it with Ca atoms. In this work, we orient the Ca oven such that the Ca

atom spray is suppressed below 150 µm height. As such, loading of ions is performed at heights greater than 150 µm. Then, if desired, the ion is shuttled to an operational height below 150 µm.

We note that extending this work to multiple ions arranged in a vertical string will face new technical challenges. On such consideration is that imaging ions with high numerical aperture from the side instead of the top of the surface trap is hampered by the small trapping height compared to the extent of the trap chip and may suffer from enhanced collection of laser scatter from the surface. Careful alignment of the imaging objective at an angle may circumvent this issue and still allow for resolution of individual ions in the vertical string.

Surface traps based on our design can also be used for remote coupling of charged particles via conducting interconnects [57], where the distance to the coupling element determines the coupling strength. This approach may be interesting for linking ions in separate regions of an extended surface trap for quantum computing applications or sympathetic cooling of ions which are unreceptive to laser cooling.

Chapter 5

Experimental setup

5.1 Trap chip

5.1.1 Trap chip architecture

The work discussed in this thesis is performed on a single trap chip, with electrode layout shown in Fig. 5.1. The trap chip measures 12.7 mm × 6.8 mm × 0.5 mm and houses three separate trapping zones. The trapping potentials in each zone are predominantly affected by the central electrode pads. Voltages are routed onto the trap chip electrodes via wire bond connections on the outer electrode pads. These wire bond pads are positioned far from the central trapping zone to mitigate their influence on the trapping fields. 20-µm-wide leads are attached to the rectangular DC electrode pads to route voltages from off-chip sources. The leads are kept relatively thin to reduce their effect on the trapping fields. Empty space is filled with a ground plane. Leads to the RF electrodes are wider (40 µm width) to increase the conductivity and accommodate for high RF powers. All electrodes are separated by trenches of 20 µm width and 50 µm depth, a design element that prevents formation of shorts between adjacent electrodes.

The elevator trap introduced in Chapter 4 frames one trapping zone located in the lower half of the trap chip in Fig. 5.1. It is composed of 9 DC electrodes, labeled as 17 - 25, and 4 RF electrodes colored green. To prevent phase offsets among the RF signals, the wire lengths of all RF electrodes, from wire bond pad to central pad, are identical.

The other two zones sit in the upper half of the trap chip. By design, each individual upper trapping zone is a smaller-scale reproduction of the elevator trap from Chapter 4. We jointly term these two traps as the 'double trap', consisting of the so-called *top* and *bottom* traps. The *top* double trap is comprised of 8 DC electrodes, labeled in Fig. 5.1 as 1 - 8, and 4 RF electrodes, shown in green. The *bottom* double trap is similarly structured with 8 DC electrodes, labeled in Fig. 5.1 as 9 - 16, and 4 RF electrodes. Further details of the double trap are discussed in Chapter 7. Nevertheless, we note here that the distinguishing feature of our double trap is an electrically floating wire which connects the centers of the *top* and *bottom* traps. The center electrode (colored red in Fig. 5.1) of the double trap is the only

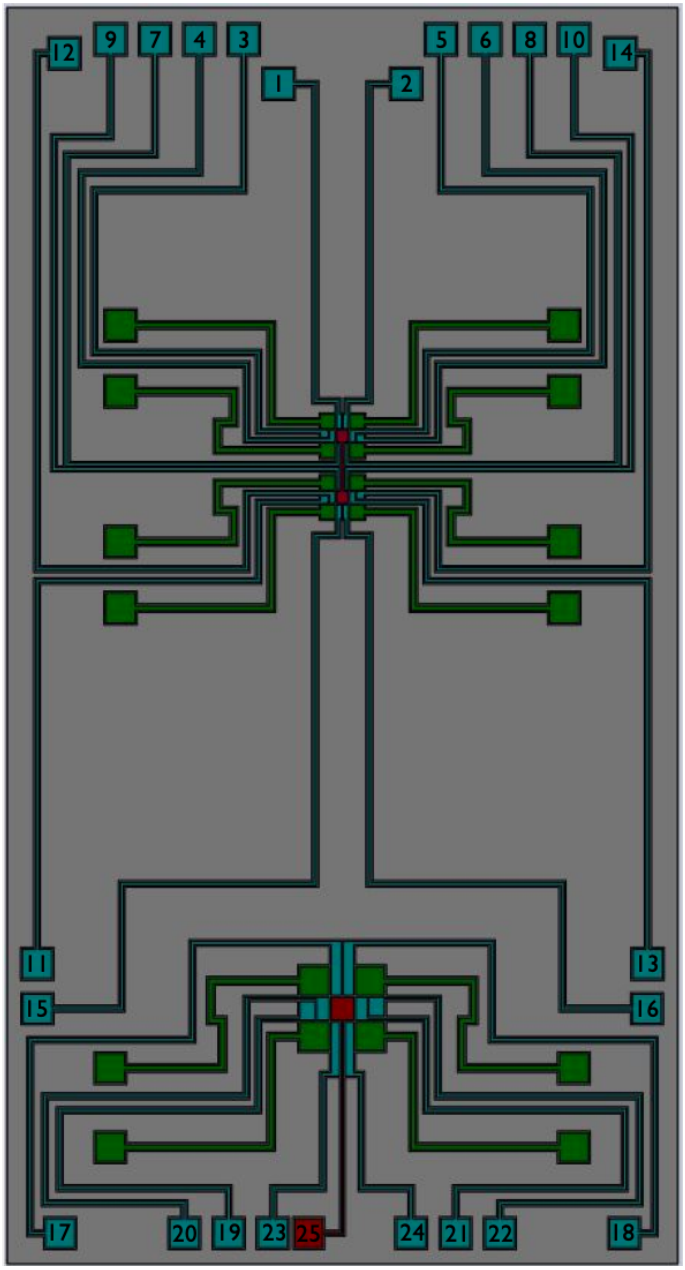

Figure 5.1: Schematic of the trap chip showing the electrode patterning for routing voltages onto three distinct trapping zones. The lower half of the trap chip contains the architecture for the elevator trap. The other two trapping zones are located in the upper half of the trap chip and jointly form the double trap. The large region in grey acts as a continuous ground plane while green electrodes are driven with RF signals and DC electrodes are colored cyan. Numerical labels of the DC pads correspond to connections with the respective numerical labels in Fig. 5.3 and Fig. 5.4.

electrode on the trap chip with no connection to external control voltages. This electrically floating element acts as the crux for novel experiments explored in Chapter 7.

With a separation of 5 mm between the elevator trap and double trap, the electric-field cross-talk between the traps is negligible, meaning we may independently operate in either trap.

5.1.2 Trap fabrication

The trap electrodes are patterned by laser-etching ultraviolet fused silica (performed by Translume, Ann Arbor, MI, United States). The surface is then layered with titanium (Ti), aluminum (Al), and copper (Cu) onto the substrate at an angle of -60° to the surface normal using electron-beam physical vapor deposition (at UC Berkeley Marvell Nanofabrication Laboratory), with respective thicknesses of 15 nm, 500 nm, and 30 nm. Subsequently, this process is repeated at an angle of 60°, coating the top surface of the electrodes and the upper walls of the trenches, thus shielding the ion from stray fields on the surface of the dielectric substrate material. In reality, the metallic layers are not necessarily distinct; they may form alloys or contain various other defects on the surface or in the bulk [58, 59]. Regardless of the potential complexities that may result from a multi-metal surface ion trap, the guiding principles behind the use of three different metals is as follows: Ti functions as a sticking layer, Al acts as the primary conducting material, and Cu protects the Al surface from rapid oxidation. Furthermore, the angled evaporation prevents metal build up inside of the trenches, which may lead to unwanted electrical shorts or noise.

5.2 Ion trap apparatus

In this section, we detail the assembly process of our ion trap apparatus and the resolutions to experimental issues faced during construction. As reference, a full-level cartoon cross-section of the trap assembly is shown in Fig. 5.2(left) along with a labeled photograph of the setup in Fig. 5.2(right). The full structure is situated in an ultra-high vacuum (UHV) chamber held at pressure $< 10^{-11}$ torr.

5.2.1 Trap assembly

After vapor deposition of the trap chip, it is mounted onto a 1-mm-thick SiO_2 spacer, which is then placed upon a custom-made ceramic leadless chip carrier (CLCC). These three components are attached together with EPO-TEK H20E silver epoxy and cured in vacuum for 2 hours at 100° C. The DC lines on the CLCC are filtered to ground with 10 nF capacitors[1] that are soldered with Kester Lead-free and fluxless solder. The purpose of the spacer is to elevate the surface of the trap above all other components, such as the CLCC capacitors

[1]Digi-Key P/N: 445-12303-1-ND, with fooprint of 1.0 mm x 0.5 mm, and detailed description: CAP CER 10000PF 50V X8R 0402

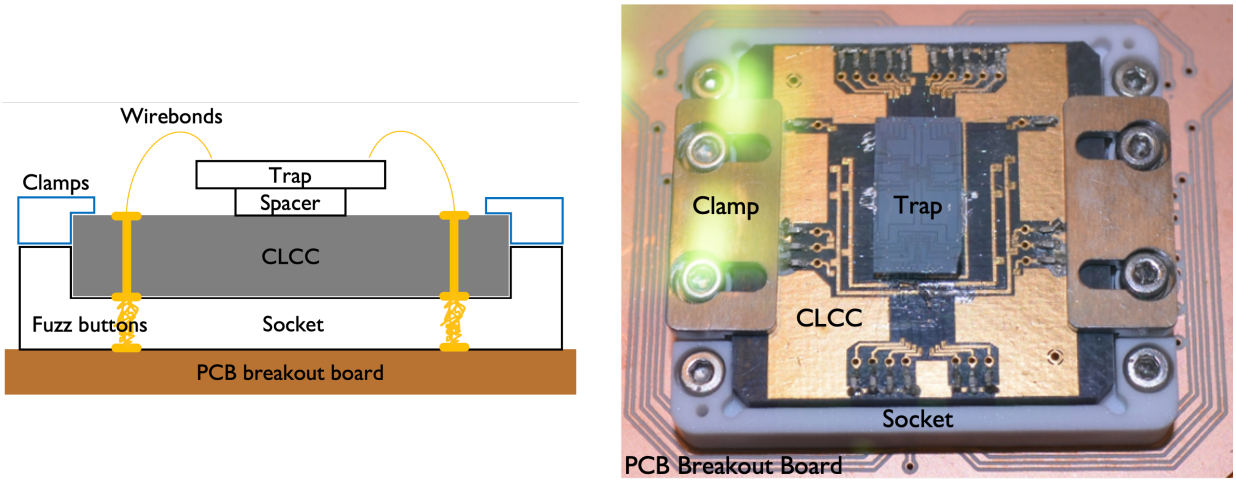

Figure 5.2: (Left) Cartoon layout of the in-vacuum trap assembly. Electrical connections routed from the PCB board to the trap are shown in gold. (Right) Photograph of the full trap assembly with relevant components labeled. For reference, the CLCC dimensions measure 33 mm × 33 mm.

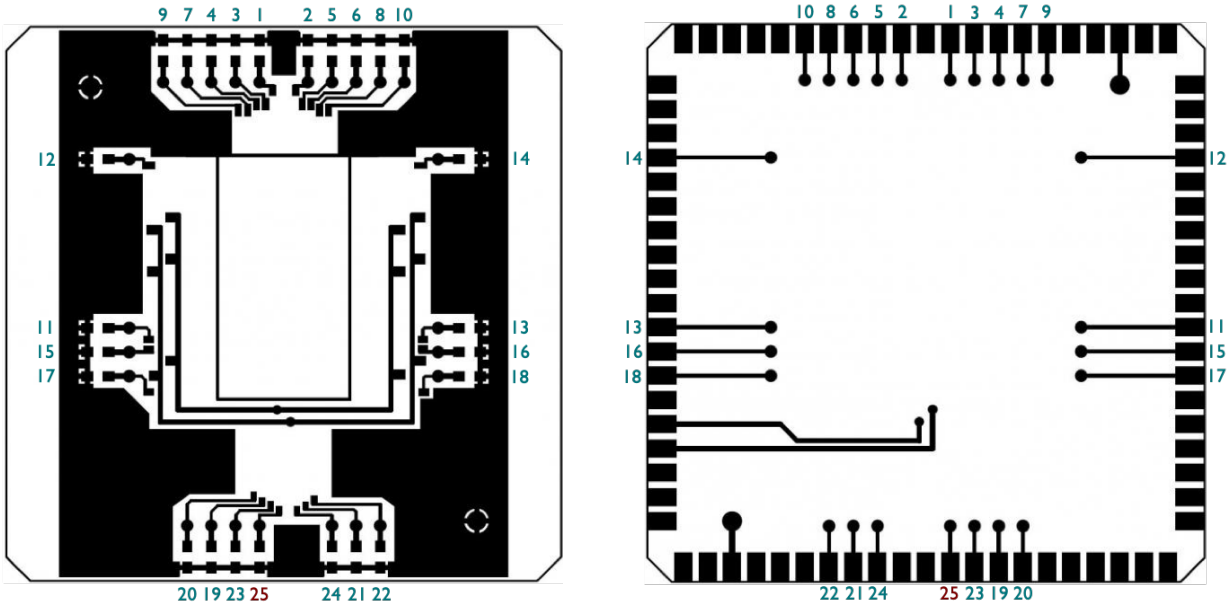

Figure 5.3: (Left) Top-view schematic of the CLCC where black regions are gold-plated. The trap chip is to be positioned in the central rectangle and the wire bond pads are positioned to be near their respective trap chip electrode pads. (Right) Bottom-view of the CLCC. Through-hole connections are shown with black circles.

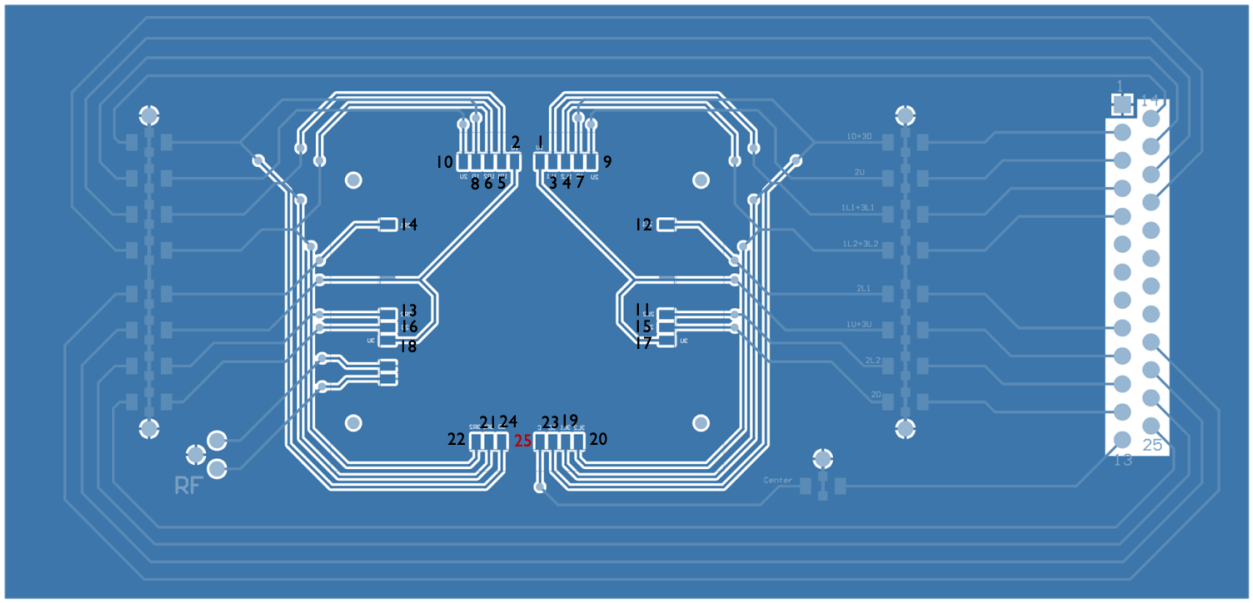

Figure 5.4: Schematic of the PCB breakout board on which the ceramic socket is mounted. Traces outlined in white are located on the top-side of the board whereas light-blue shaded traces are located on the reverse-side of the board. DC and RF voltages are routed onto the board via UHV-safe Kapton-insulated copper wires.

and clamps. This allows for unobstructed optical access from the sides of the trap chip. Following the curing process, the trap chip's outer electrode pads are wire-bonded onto their respective CLCC pads via the numerical mapping shown in Fig. 5.1 and Fig. 5.3(left). The CLCC is then physically clamped down into a ceramic socket, which is, in turn, screwed into a Roger's PCB breakout board, shown in Fig. 5.4.

UHV-safe Kapton-insulated copper wires are soldered onto the PCB board to create in-vacuum connections that route voltages from external RF and DC sources. The DC lines on the PCB board are also filtered to ground with 47 nF feed-through capacitors[2]. Electrical signals on the PCB are routed to the CLCC through fuzz buttons and hard hats that make contact between the top of the Roger's PCB board and the bottom of the CLCC [60]. The mapping of these connections can be seen by comparing Fig. 5.3(right) and Fig. 5.4.

After assembly of the full trap setup is completed, the vacuum chamber is sealed and pumped down to a pressure of 10^{-8} torr using a vacuum turbopump. The chamber is then baked at 180° C for 1 - 2 weeks, with the turbopump still attached and running. It is prudent to set the bake temperature as high as possible without negatively affecting the in-vacuum components. In our case, the maximum temperature is set by the silver epoxy, which is rated up to 200° C. The purpose of this high-temperature baking process is primarily to remove excess water and heavy hydrocarbons from the vacuum chamber. The reduction of such elements as well as the overall pressure are monitored with a residual gas analyzer

[2]Mouser P/N: 581-W3F15C4738AT1F

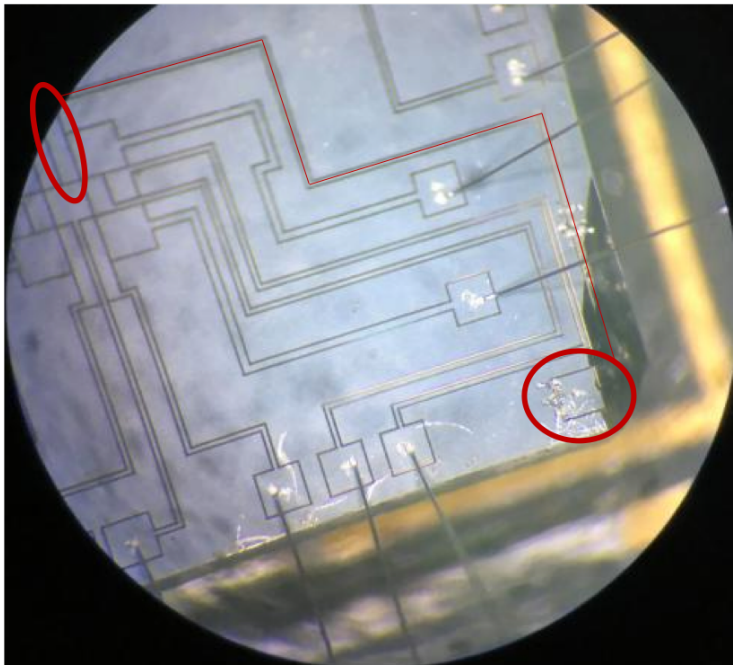

Figure 5.5: Microscope image of trap chip with a burnt lower-right corner. The isolated pad and wire path of electrode '18' are highlighted in red. All parts of electrode '18' are purposely shorted to the trap ground with several wire bond feet.

(RGA). When the chamber pressure stabilizes, it is brought back to room temperature and achieves a pressure of 10^{-10} torr. Following the bake, we further reduce the pressure by firing multiple cycles of a titanium-sublimation pump, which absorbs background gases by creating a reactive 'sticking' layer on the inner sides of the vacuum chamber. Finally, constant running of an ion pump brings the pressure below 10^{-11} torr.

5.2.2 Experimental issues

Prior to successful operation of our ion trap apparatus, we cycled through a few iterations of the trap assembly in order to overcome experimental issues that arose throughout the construction process.

One major issue was a faulty connection found on the CLCC. Our custom-made CLCC routes voltages from the bottom side, Fig. 5.3(right) to the top side, Fig. 5.3(left), via through-hole connections with metal thickness of 40 um. We discovered that both RF lines on the CLCC were disconnected at the through-hole via. The origin of the RF line disconnect remains unclear, but a likely suspect is the usage of high input RF powers causing either electrical or thermal breakdown of the through-hole vias. This issue was patched by soldering wires through the vias to explicitly establish connections between the bottom and top portions of the CLCC RF paths. Unfortunately, in the process of soldering, the lower

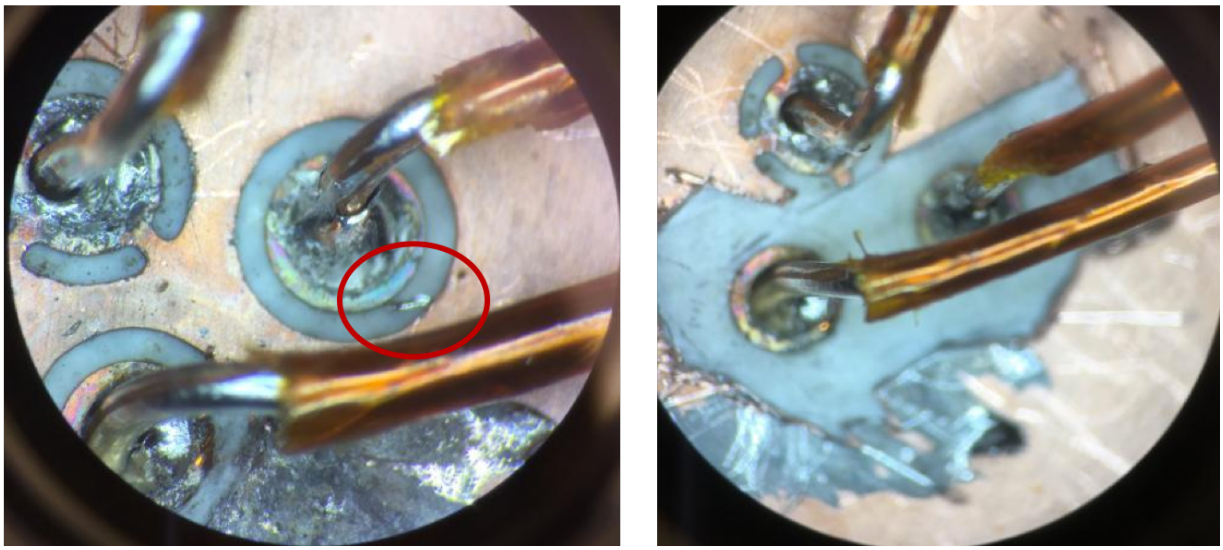

Figure 5.6: (Left) Microscope image of short on PCB breakout board caused by small solder flake, indicated by the red circle. The ground reference point for the RF is in the upper left while the other two connection lines route the oscillating RF signals. (Right) Image of the same RF connectors on the PCB breakout board following removal of the solder flake and surrounding ground plane.

right portion of the trap chip was burned, see Fig. 5.5, rendering one of the DC electrodes useless, explicitly the electrode labeled '18' in Fig. 5.1. A large portion of the trace of this DC electrode was burnt away, causing a separation between wire bond pad and the central electrode pad. As electrode '18' could no longer be controlled with external voltages, we chose to explicitly ground it to the trap ground with wire bond feet.

After fixing the CLCC, we successfully trapped ions in our system for the first time. Though after a short period, another connection issue was detected on the PCB breakout board. In particular, we observed a gradual (over the course of days) increase in required input RF power to achieve a $2\pi \times 1$ MHz radial trap frequency. This symptom worsened and resulted in the inability to trap ions regardless of RF power. We discovered that one of the RF lines was shorted to the trap ground, and the culprit was found to be a small, loose solder piece, as shown in the red circled area in Fig. 5.6(left). As this solder flake was inauspiciously dropped near an RF line, it gradually started to reflow under the higher temperatures generated by the high power RF signals and eventually connected the RF line to the ground plane of the PCB breakout board. A cautious solution was implemented by removing the solder flake as well as the ground plane surrounding the RF lines, as seen in Fig. 5.6(right).

5.3 Electronics

5.3.1 DC electronics

DC voltages are controlled from a computer and routed onto trap electrodes through a digital-to-analog converter (DAC) system. Commands to set the voltage values are sent from the computer to a field-programmable gate array (FPGA)[3] DAC controller board [15]. The DAC controller board routes these instructions via optical fibers to an on-board FPGA[4], which advances the voltages of select DAC chips[5]. The DAC chips take 16-bit input corresponding to output voltages of ± 10 V. The voltages are amplified with operational amplifiers[6] to achieve a final output of ± 40 V with 16-bit precision. The output analog voltage is routed to the vacuum chamber via a snakeskin sleeved D-SUB 25 ribbon cable. Prior to entering the vacuum chamber, each DC line is heavily filtered by a 4-stage low-pass filter with 3 dB point at 300 Hz. Each stage consists of a series 1 kΩ resistor in parallel with 94 nF and 100 pF capacitors to ground.

5.3.2 RF electronics

Standard operation of our ion trap requires RF voltages on the order of 100 V oscillating at frequency of order 10 MHz. Direct application of such a drive onto the ion trap causes several experimental issues. In particular, the impedance of ion traps are mostly capacitive (equivalent to 22 pF in our case) while the RF output from our signal generator[7] and amplifier[8] has a mainly resistive impedance of 50 Ω. This impedance mismatch results in reflection of the power from the ion trap back into the amplifier [61]. To mitigate these effects, we employ an impedance matching technique which centers on an inductively coupled half-wave resonator with two output arms that are equal in amplitude and frequency, but 180° out-of-phase. Details of the resonator design and implementation are described in Section 5.3.3.

Tuning circuit

For the vertical-linear operation mode of the elevator trap, we must generate perfectly canceling RF fields along the vertical axis of our trap, which relies on precise matching of the signal on the two diagonal pairs of RF electrodes. Ideally, they are at the same frequency and amplitude, but of opposite phase. However, any mismatch in those parameters, for instance due to fabrication imperfections or slight differences in the capacitance and inductance of wiring, leads to a residual RF field at the central trapping location, and consequently, micromotion in the vertical direction. In a real device, such a mismatch can easily occur and

[3] Opal Kelly XEM3001
[4] Altera Cyclone II
[5] Analog Devices AD660
[6] Texas Instruments OPA554
[7] Rohde & Schwarz SMB 100A
[8] Mini-Circuits ZHL-1-2W-S+

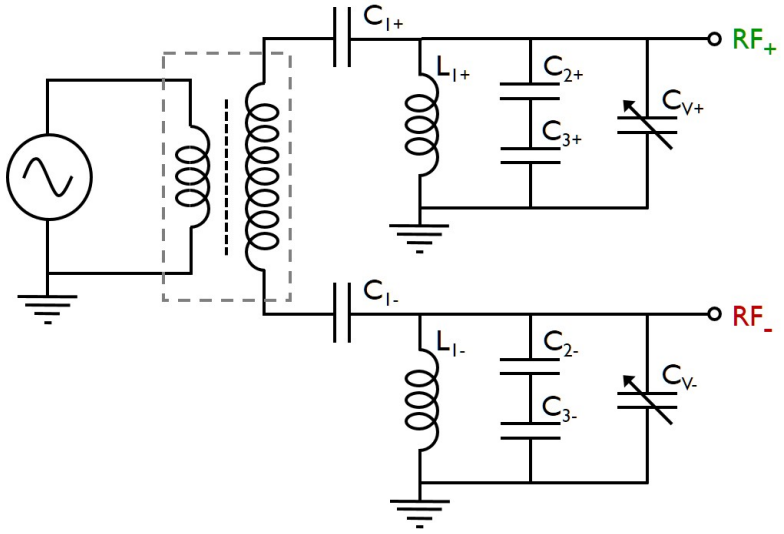

Figure 5.7: Circuit schematic for the implementation of the out-of-phase RF drive. The boxed region indicates a toroidal resonator with a powdered iron core. Each RF signal arm is equipped with a high-pass filter ($C_{1\pm}$, $L_{1\pm}$), a capacitive divider ($C_{2\pm}$, $C_{3\pm}$), and tuning capacitor ($C_{V\pm}$)

is observed in our setup. In the following we describe the circuit used to deliver the RF voltages to the trap electrodes in more detail and show how to reduce voltage mismatch between the RF lines by taking the vertical micromotion as a figure of merit.

Fig. 5.7 shows the circuitry for passively routing out-of-phase RF signals onto separate electrodes. RF signals from the source are amplified and linked to the trap electrodes via a toroidal resonator, indicated by the boxed region in Fig. 5.7. The right-hand side of the resonator forms a resonant circuit with the cumulative capacitance of the trap load, dominated by the $\mathrm{RF}_{\pm}$ electrode wiring. This resonator circuit matches the real 50 Ω resistance from the signal generator to the imaginary impedance of the trap electrodes. The two sides of the resonator output split the following circuitry into two arms with nominally equal amplitude, frequency, and opposite phase. Each arm contains a high-pass filter ($C_{1\pm} = 2$ nF and $L_{1\pm} = 100$ mH), where the inductors, $L_{1\pm}$, act as ground references for the RF signal. The amplitude and phase mismatch between the two RF arms can be measured with the capacitive dividers consisting of $C_{2\pm} = 2$ pF and $C_{3\pm} = 100$ pF. To correct for discrepancies, tunable capacitors, $C_{V\pm}$, with a range of 2 - 7 pF are added in parallel to the trap electrodes. These allow us to tweak the amplitude, frequency, and phase of the resonant circuit, thus reducing the mismatch of the two RF arms.

Out-of-phase RF optimization

Imperfect cancellation of RF fields along the vertical z-axis manifests on the ion as excess micromotion in the z-direction. Micromotion, in turn, provides a much more relevant and

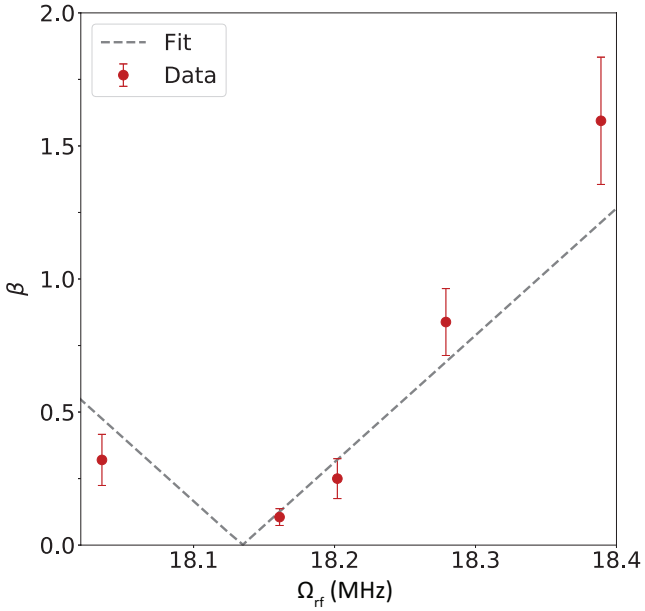

Figure 5.8: Measured micromotion modulation index β, which is defined to first order as $2\Omega_1/\Omega_0$ at a trapping height of 200 µm. The RF drive frequency, Ω_{rf} reflects the resonance of the RF circuit which is tuned via the capacitors $C_{V\pm}$. Here we change only one of the two tunable capacitors and the dashed line shows the expected linear dependence of the modulation index on the circuit resonance.

sensitive measurement of differences in the resonator arms as compared to the capacitive divider signal. By tuning the capacitor on one arm, we can measure changes in the ratio of the first order micromotion sideband Rabi frequency, Ω_1, and the Rabi frequency of the direct carrier transition, Ω_0. Using electrostatic and lumped circuit simulations we find the modulation index, $\beta \approx 2\Omega_1/\Omega_0$ should depend to first order linearly on the resonance frequency and theoretically vanishes when both arms match amplitudes and phases perfectly, i.e. when the resonance frequencies in each arm match [62]. Experimental constraints, such as a finite resonator quality factor, naturally limit how closely we can approximate the perfect case. In our case, cf. Fig. 5.8, the modulation index could be reduced to $\beta \approx 0.1$, a considerable improvement over the un-optimized modulation index, $\beta \approx 1.5$. We have repeated the procedure for vertical micromotion compensation with a several toroidal resonators with different inductances and quality factors and found similar behaviours.

RF amplitude modulation

Certain trapped ion experiments require modulation of the RF amplitude. For instance, we may utilize RF modulation to implement parametric coupling of separate trapped ion

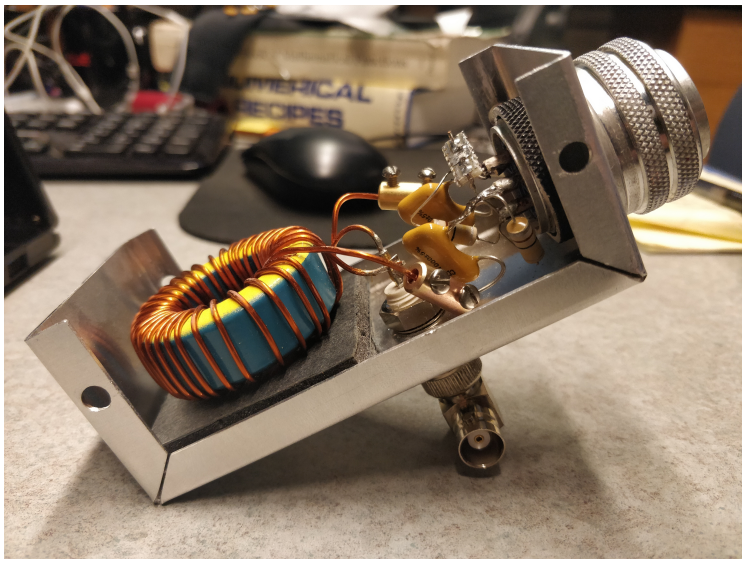

Figure 5.9: Image of toroidal half-wave ($\lambda/2$) resonator made from 1-mm-thick insulated copper wire wrapped around a ferrite core of inner diameter 2.4 cm and outer diameter 4.1 cm. The aluminum housing (shown uncovered) shields the resonator and RF circuitry from external fluctuating fields. The RF circuit in this particular iteration includes only the high-pass filters ($C_{1\pm}$, $L_{1\pm}$) for each arm of the $\lambda/2$ resonator output.

motional modes [63] or measure ion motional coherences [64]. We apply the modulation onto the RF electrodes with an external signal source[9] connected to our RF signal generator. We work with modulation on the order of the trap frequencies, which is typically < 2 MHz, and the source is toggled on a TTL trigger for precise timing of the modulation with respect to experimental pulse sequences.

5.3.3 Resonator

A core element of the RF impedance matching circuit described in Section 5.3.2 is the resonator which acts as a transformer to provide high-voltage gain as well as frequency filtering of noise.

Physical implementations

There are several possible physical implementations of resonators for the purposes of trapped ion RF circuits. A common type is the helical resonator which provides adequately high Q factors and appropriate handling of the high power requirements for trapped ion RF systems [61, 65]. However, these resonators are large, bulky, and difficult to tune and customize. As an alternative, we work with toroidal resonators throughout this thesis, which

[9] Agilent 33220A

have a smaller form factor and simpler fabrication, making them ideal for testing and tailoring to specific needs. These resonators are modeled after inductively coupled transformer coils wrapped around a ferrite core, as shown in Fig. 5.9. The drawback of this architecture is a limited power output due to the thermal properties of the ferrite core, which cannot withstand high temperatures.

Other resonator builds include transmission line coaxial cables [66] and lumped-element circuits [67]. Coaxial cables can handle high powers and are known to create resonators with high Q factors at the cost of large form factors, since the length of cable directly corresponds to the desired resonant wavelength, i.e. ~ 2 m to create a $\lambda/4$ resonator at 20 MHz drive frequency. Lumped-element circuits replace the physical resonator component with an RLC circuit. Their compact nature allows for in-vacuum and cryogenic implementations as well as designs which require multiple RF drives. Additionally, the RLC resonator may be placed as close as possible to the ion trap to avoid RF power dissipation through long in-vacuum cables.

Design guide

One of the most important quantities of a resonator is the Q factor defined as the ratio between the resonant drive frequency, Ω_{RF}, and the full-width at $1/\sqrt{2}$ of the maximum resonant voltage, $\delta\Omega_{RF}$,

$$Q = \frac{\Omega_{RF}}{\delta\Omega_{RF}}. \tag{5.1}$$

We desire to maximize the Q factor, since a higher Q factor passively improves the voltage gain and the bandpass filtering around Ω_{RF}. The Q factor of the resonator is dependent on the effective RLC parameters of the full RF circuit,

$$Q = \frac{1}{R}\sqrt{\frac{L}{C}}. \tag{5.2}$$

This relation implies that the Q factor is maximized when our resonator design achieves minimum resistance, R_r, and self-capacitance, C_r. In addition, by modifying the number and spacing of output turns on the resonator, we may tune the self-inductance L_r and, consequently, tune the Q factor and resonant frequency Ω_{RF}. In terms of the full RF circuit, we note that the self-inductance, L_r, of the toroidal resonator dominates L while R and C are dominated by the in-vacuum ion trap connections.

For impedance matching, the main tuning parameter is the number and spacing of input turns on the toroidal resonator. Experimentally, we determine the quality of the matching circuit by measuring the reflected power from the ion trap with a standing wave ratio (SWR) meter[10]. For all operational resonators in this thesis work, the input turns are adjusted until the SWR meter reads a value of < 1.2, corresponding to a reflected power of $< 0.8\%$.

[10] MFJ-892

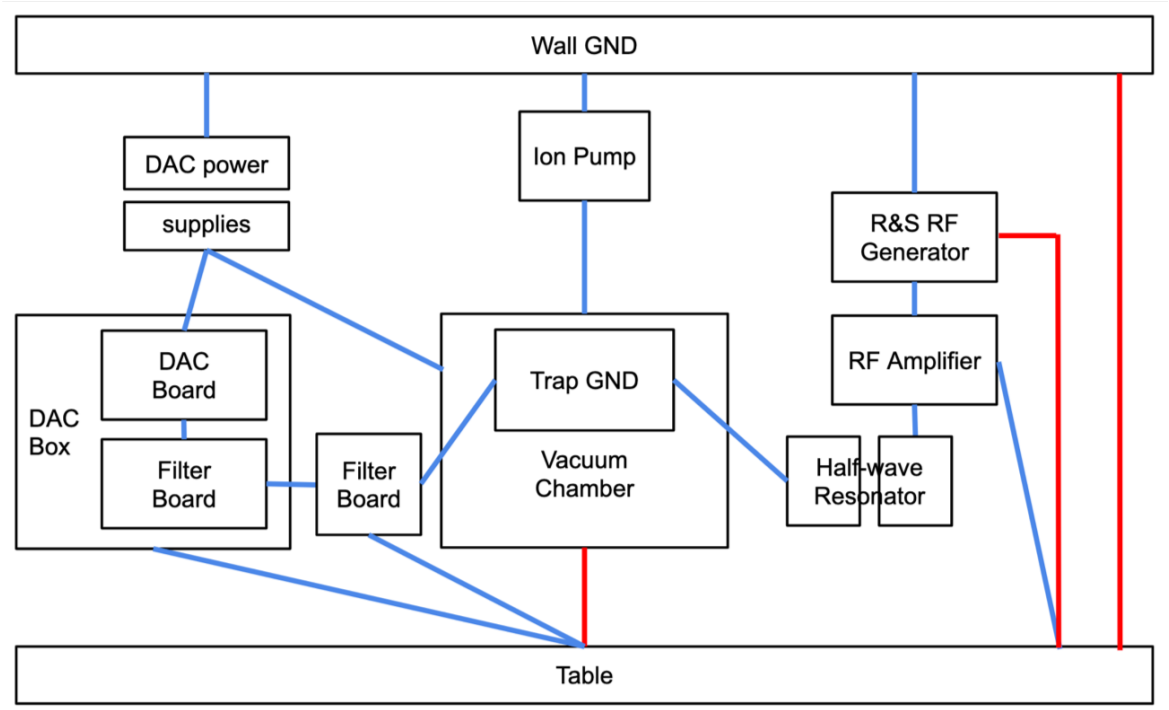

Figure 5.10: Block-diagram of the experimental ground configuration used in this thesis. Ground connections are shown in blue, and connections which greatly affect the the noise are highlighted in red. Points where the grounding connections join on the diagram correspond to physical star-ground points in the setup.

Finally, we note a limitation of the toriodal resonator design is the unstable thermalization of the ferrite core. When working with high powers ($\gtrsim 2$ W), we observe gradual fluctuations in the temperature of the toroidal resonator on the order of hours. In accordance with the temperature, the resonance frequency of the RF system shifts, leading to slow drifts of the RF power which causes slow drifts of the radial trap frequencies. To stabilize the thermalization, we submerge the entire wire-wrapped ferrite core in STYCAST epoxy, which has a high thermal conductivity. Following this improvement, we measure minimal trap frequency drifts of < 1 kHz over the course of a couple hours. However, addition of the STYCAST changes the electrical properties of the resonator, so care must be taken to re-tune the resonator coils for good impedance matching and high Q factor.

5.3.4 Grounding

In an effort to reduce electronic noise in our trapped ion system, we find that proper grounding is essential. A schematic of our experimental grounding is shown in Fig. 5.10, where electrical elements of the trap apparatus are labeled in black boxes and ground connections are shown as colored lines. Red lines indicate connections that significantly affect the noise

in our system while blue lines represent connections required for functional operation of each element. As a general rule of thumb, we strive to establish good connections among all ground references. In our optimal configuration, the grounds of all pairwise components are connected with measured resistances of no more than 1 Ω.

To quantify the effect of different ground connections on the noise in our system, we measure the spectral noise on each electrode relative to the trap ground. Measurements are performed directly off the electrode ports of the vacuum chamber in order to extract the noise characteristics as close to the trap chip as possible. With the ground configuration from Fig. 5.10, we establish spectral noise below −105 dBm/Hz at 1 MHz for all electrodes, with reference background noise of −108 dBm/Hz at 1 MHz. Though this grounding scheme works in our particular case, it does not necessarily address the underlying cause of noise, and thus may require modification for different trapped ion setups.

5.4 Optics

5.4.1 Lasers

The six continuous wave (CW) laser sources for loading, trapping, and manipulation of $^{40}Ca^{+}$ ions are located in a room separate from the experiment and routed onto the experimental optical table through 20 m long optical fibers. All lasers used in our experiments are diode lasers. The 397 nm and 422 nm laser light is frequency doubled with an external bow-tie cavity from 794 nm and 844 nm diodes, respectively. While the photoionization laser light is free-running, the 794 nm, 854 nm, and 866 nm lasers are locked to external reference cavities. Further details of the laser setup may be found in T. Pruttivarasin's thesis [33]. Since the 729 nm laser addresses the $^{40}Ca^{+}$ qubit transition, we require sub-kHz linewidth and high power output. This is achieved by locking to a high finesse cavity, running the laser light through an injection lock scheme [15], and amplifying the light with tapered amplifiers. In addition, we may implement fiber noise cancellation, see Section 5.4.2, to maintain narrow linewidth at the output of the fiber transporting laser light from the 729 nm laser to our set-up.

On the experimental optical table, the photoionization laser light is sent directly into the vacuum chamber, taking care to orient the 422 nm beam perpendicular to the Ca oven in order to avoid large Doppler shifts caused by the velocity of Ca atoms ejected from the oven. The 397 nm, 729 nm, 854 nm, and 866 nm laser light passes through acousto-optic modulator (AOM) networks, which allow for amplitude and frequency control of each individual laser prior to entering the vacuum chamber. The AOMs are driven with RF signals generated by direct digital synthesizer (DDS) boards which take commands from an FGPA[11] connected to a computer, see T. Pruttivarasin's thesis [33] for a detailed setup description.

[11] Opal Kelly XEM6010

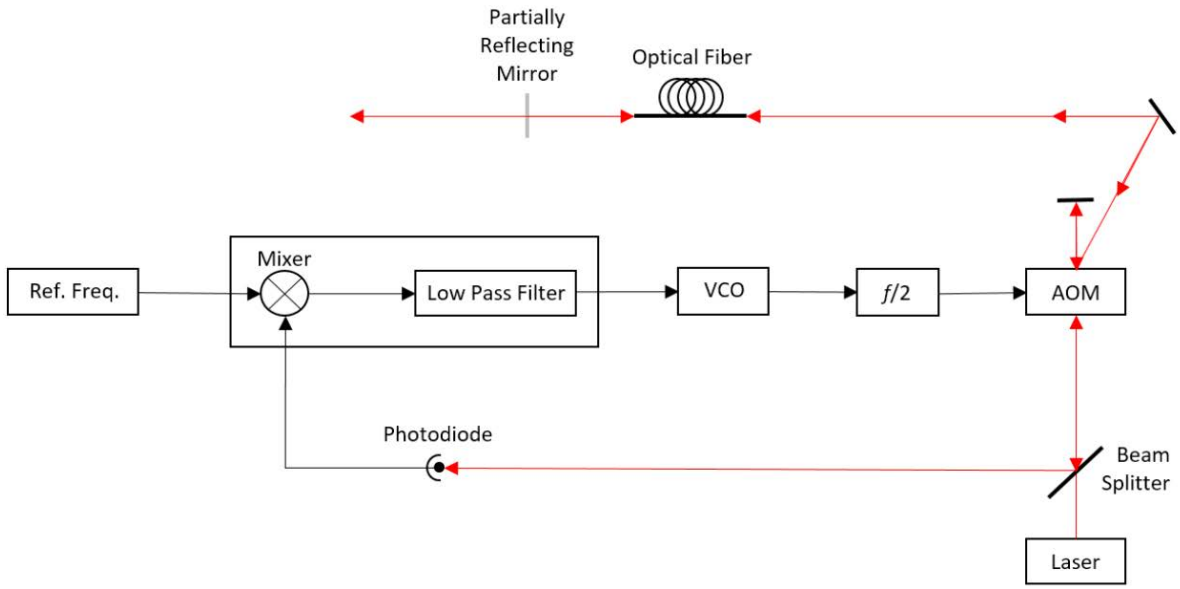

Figure 5.11: Experimental setup of the PLL-based fiber noise cancellation scheme. Red arrows represent optical paths and black arrows indicate electrical connections.

5.4.2 Fiber noise cancellation

Motivation

Long fibers are easily stressed and strained from environmental effects such as acoustic noise and fluctuations in temperature and air pressure. Stress and strain cause local changes in the index of refraction of optical fibers, thus altering the optical path length (OPL) through them. Fluctuations in the OPL result in frequency and phase noise at the output of the fiber, which broaden the linewidth of the output light.

A narrow linewidth of the 729 nm beam is required for long coherence times and high-fidelity quantum operations. To mitigate the noise and reduce the output laser linewidth, we test a method developed by the NIST Boulder group [68] and utilized by the Quantum Optics Group at Innsbruck [69]. In short, a control system constantly monitors the phase noise caused by the fiber and applies an out-of-phase signal to cancel the noise. For this regulation to work, it is required that the phase noise is slow as compared to the bandwidth of the control system.

Theory and Setup

The experimental scheme for stabilization of 729 nm laser light propagating through a 20 m long fiber is shown in Fig. 5.11, where electronic connections are denoted with black arrows and optics are denoted with red arrows. We start by passing 729 nm light through an AOM

driven at $\Delta_{AOM} = 80$ MHz. The incoming light has the form

$$E^i = E_0 \cos(\omega_l t), \tag{5.3}$$

where ω_l is the laser frequency and E_0 is the electric-field magnitude. The 0^{th} order is unaffected by the AOM and immediately back reflected and detected with a fast photodiode (PD). At the PD, we expect this beam to be

$$E^0 = E_{0r} \cos(\omega_l t). \tag{5.4}$$

The first pass of the 1^{st} order diffraction of the AOM is then

$$E^1 = E_1 \cos((\omega_l + \Delta_{AOM})t - \phi_{AOM}), \tag{5.5}$$

with a detuning given by Δ_{AOM} and phase shift of ϕ_{AOM}. This light is sent through the fiber and partially reflected back, which causes a phase shift, ϕ_{fiber}, from the fiber and a reduction in magnitude from E_1 to E_{1r}

$$E^1 = E_{1r} \cos((\omega_l + \Delta_{AOM})t - \phi_{AOM} + 2\phi_{fiber}). \tag{5.6}$$

Finally, this beam passes back through the AOM, and we take the +1 order again, which outputs a counter-propagating beam to the incoming E^i beam. This final output beam acquires another detuning and phase shift,

$$E^1 = E_{1r1} \cos((\omega_l + 2\Delta_{AOM})t - 2\phi_{AOM} + 2\phi_{fiber}), \tag{5.7}$$

before detection at the same PD as E^0. Assuming $E_{0r} = E_{1r1}$, the PD detects light of the form,

$$E^{PD} = E^0 + E^1 = 2E_{0r} \cos(\omega_{beat}/2) \cos(\omega_l t + \omega_{beat}/2), \tag{5.8}$$

with a beat note signal between E^0 and E^1 at frequency

$$\omega_{beat} = 2\Delta_{AOM} t - 2\phi_{AOM} + 2\phi_{fiber}. \tag{5.9}$$

This signal is then fed to the phase-locked loop (PLL) circuit. A phase detector[12] mixes the beat note with a reference signal of 159.959 ± 0.016 MHz, and then a voltage-controlled oscillator (VCO)[13] receives the low frequency output from the mixer and outputs a reactive phase-modulated frequency. This signal is passed through a frequency divider[14] before ultimately driving the AOM. In this way, the electronics set $\phi_{AOM} = \phi_{fiber}$, thus canceling the phase noise from the fiber.

[12] Analog Devices AD8302
[13] Vectron VS-705
[14] Analog Devices HMC432

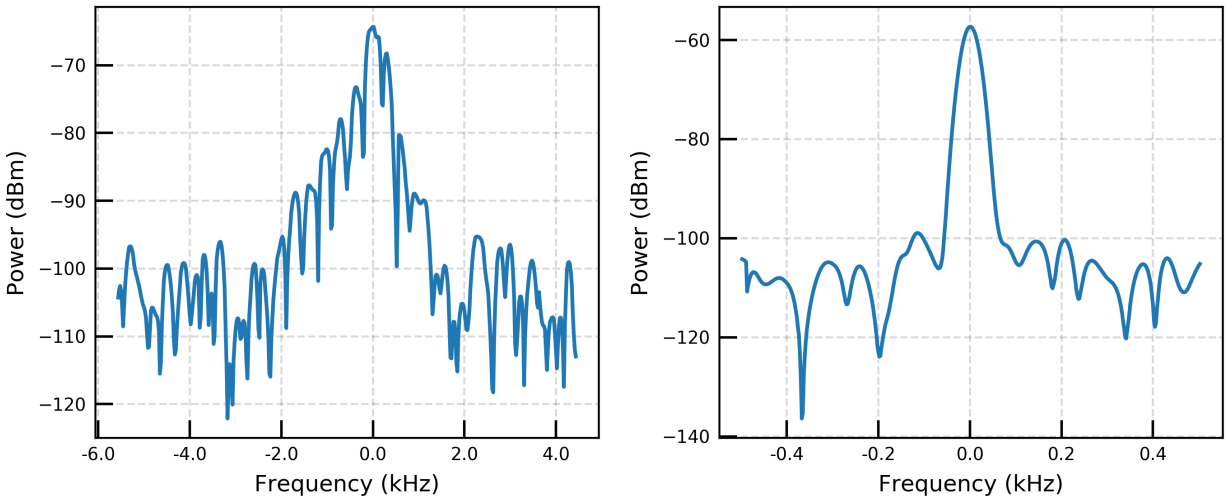

Figure 5.12: (Left) Frequency spectrum of beat note signal with PLL regulation turned OFF. Notice a full-width of $\sim$ 4 kHz. (Right) Frequency spectrum of beat note signal with PLL regulation turned ON. The full-width is now reduced to 100 Hz. Both spectra are centered around 159.959 MHz, roughly twice the AOM frequency.

Performance

To characterize the performance of our fiber noise cancellation system, we monitor the frequency spectrum of the beat note signal on the PD. The results are shown in Fig. 5.12. Without the PLL regulation, we not only see large linewidth, Fig. 5.12 (left), but there are also slower fluctuations of the center frequency as the fiber is bent or heated/cooled. With the PLL regulation on, Fig. 5.12 (right), the slow fluctuations are eliminated and the linewidth significantly reduces to 100 Hz. It is likely the linewidth is even narrower than measured, but this measurement is limited by the spectrum analyzer bandwidth.

5.4.3 Imaging

To experimentally readout the quantum state of a trapped ion, an objective lens[15] is positioned above the top viewport of the vacuum chamber with direct line of site to the trap. The fluorescence of ions are collected into the objective and directed into either an EMCCD camera[16] or PMT[17]. These imaging paths are illustrated by the solid blue lines in Fig. 5.13.

The Sill objective is engineered to have similar focal length at 397 nm and 729 nm wavelengths. Thus, in addition to collection of photons from trapped ions, the objective also functions as a lens for focusing collimated 729 nm light at the ion position. The 729 nm path is shown as solid red lines in Fig. 5.13. To achieve ideal focusing, we overlay the beam

[15] Sill S6ASS2241
[16] Andor DV885LC-VP (Serial #: X-2579)
[17] Sens-Tech P25PC

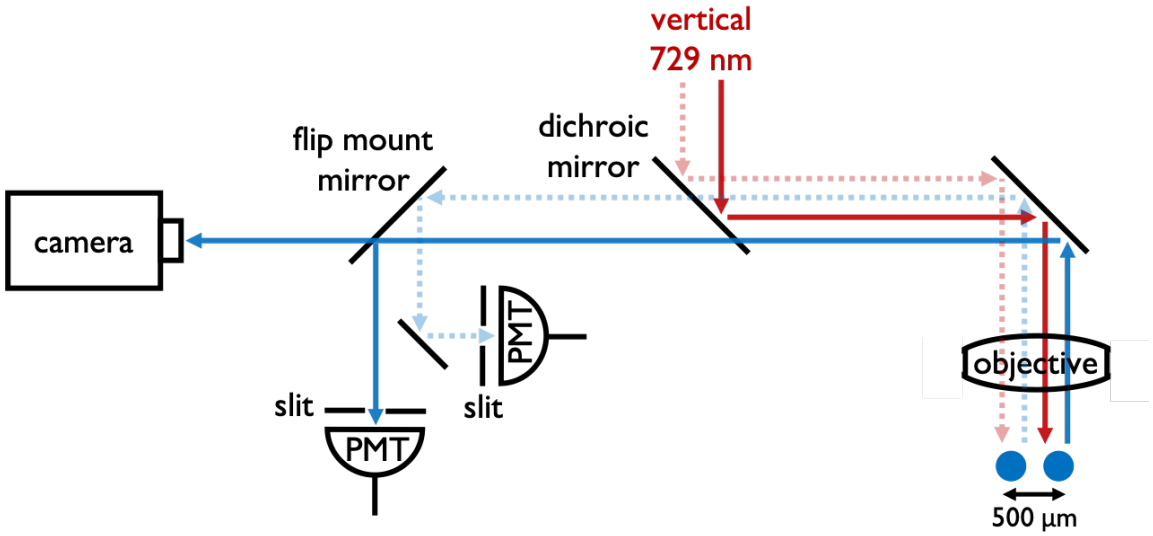

Figure 5.13: Schematic of imaging system. Solid lines show the beam paths for operation of a single trap. When operating the double trap, we add another vertical 729 nm beam for ion addressing and a second PMT for ion detection. The beam paths for these auxiliary functions are shown as transparent dotted lines. The double trap separates the ions by 500 µm, making it possible to image each ion on a separate PMT by inserting a pick-off mirror.

paths of the 729 nm light and the ion fluorescence with a dichroic mirror which reflects red light and transmits blue light.

When operating in the double trap, the second ion is imaged onto a separate PMT by picking off its fluorescence with a mirror. This auxiliary imaging path is shown as transparent dotted blue lines in Fig. 5.13. Additionally, a second 729 beam is added to address the second ion, shown as transparent dotted red lines in Fig. 5.13.

Chapter 6

Electric-field noise

Strong coupling between the charge of an ion and external electric fields is essential for 3-D confinement of ions. However, this interaction manifests as a double-edged sword, as ions are also sensitive to residual fluctuations of electric fields in the environment. This electric-field noise couples to the electric dipole moment of the ion, $|\vec{p}| = e|\vec{x}_0|$ where $|\vec{x}_0| = \sqrt{\hbar/(2m\omega_t)}$ is the extent of the motional ground-state wavefunction, and induces unwanted transitions between ion motional states, ultimately leading to increased ion energies, a process we term as heating.

Ion heating is an impediment in many trapped ion applications. It lowers the fidelity of gate operations involving the quantized motional states [70] and it contributes to fractional uncertainties in optical clock experiements [71]. On the upside, we can take advantage of the ion's sensitivity by probing the electric-field noise in ion traps with measurements of the ion heating rate, $\dot{\bar{n}}$, where $\bar{n} = \langle a^\dagger a \rangle$ is the average occupation number of the harmonic oscillator mode.

6.1 Single-ion motional heating

Let us start with a theoretical treatment of the heating rate to understand its dependencies. In the case of heating an ion from the motional ground state, $|0\rangle$, to the first excited state, $|1\rangle$, we can define a rate, Γ_h, from Fermi's golden rule [72]. This rate holds under the assumption that the ion is located in the RF null, allowing us to neglect micromotion contributions.

$$\Gamma_h \simeq \frac{e^2}{4m\hbar\omega_t} S_E(\omega_t), \tag{6.1}$$

$$S_E(\omega_t) = 2\int_{-\infty}^{\infty} d\tau \, \langle \delta E_t(\tau)\delta E_t(0)\rangle \, e^{-i\omega_t\tau} \tag{6.2}$$

where e and m are the ion charge and mass, ω_t is the trap frequency, and S_E is the spectral density of the electric-field noise that only includes positive frequencies. Thus for ions close to the motional ground state, we have $\dot{\bar{n}} = \Gamma_h$.

6.1.1 Master equation

A more general approach to understanding the heating rate can be seen from writing out the master equation for the motion of the ion with the density matrix formulation, $\hat{\rho}$. When the ion motion is coupled to a bath of harmonic oscillators at thermal equilibrium, we have [73]

$$\dot{\hat{\rho}} = -\Gamma(N_b+1)[\hat{a}^\dagger\hat{a}\hat{\rho} - 2\hat{a}\hat{\rho}\hat{a}^\dagger + \hat{\rho}\hat{a}^\dagger\hat{a}] - \Gamma N_b[\hat{a}\hat{a}^\dagger\hat{\rho} - 2\hat{a}^\dagger\hat{\rho}\hat{a} + \hat{\rho}\hat{a}\hat{a}^\dagger] \tag{6.3}$$

where $\hat{a}^\dagger$ and $\hat{a}$ are the creation and annihilation operators of the ion's motional quanta, N_b is the average occupation of the environment bath at temperature T and will be defined implicitly in Eq. (6.4). Physically, the $\Gamma(N_b+1)$ terms account for spontaneous and stimulated emission, or energy transfer from the ion system to the bath, and the ΓN_b terms describes absorption of energy from the bath to the ion system. Eq. (6.3) holds under the Born-Markov approximation, meaning the time-evolution is valid in the Markovian limit of $t \gg \tau_b$, where $\tau_b = 1/\omega_{bc}$ is the correlation time of the bath, and ω_{bc} is the high frequency cutoff of the bath. Under this assumption, we can derive the time-evolution of the average ion motional occupation [74],

$$\bar{n}(t) = N_b(1 - e^{-\Gamma t}) = \frac{1 - e^{-\Gamma t}}{e^{\frac{\hbar\omega_t}{k_B T}} - 1}. \tag{6.4}$$

With this, we can solve for the heating rate,

$$\dot{\bar{n}}(t) = \Gamma N_b e^{-\Gamma t} \approx \Gamma N_b \equiv \Gamma_h. \tag{6.5}$$

Typically, we operate our traps at room temperature ($\sim$ 300 K), so we find ourselves in the regime of $N_b \sim 10^6$. Notice that in general, the heating rate is non-linear as a function of time, but our experiments typically operate under the conditions of $\Gamma \sim 10^{-4}$/s and $t \sim 1$ ms. Thus the combined condition of $\Gamma t \to 0$ allows us to approximate the heating rate as constant in time, as seen in right side of Eq. (6.5). Lastly, it should be mentioned that this analysis of the heating rate does not hold in the non-Markovian regime of $t \lesssim \tau_b$. Naively applying the above solution in the short time regime will continue to give a linear time-evolution of $\bar{n}$, whereas the true, non-Markovian, time-evolution for short times should follow a quadratic trend [74].

6.1.2 Spectral density

A physical understanding of the mechanism behind ion heating is rooted in the spectral density of electric-field noise sources. In general terms, the spectral density may be a complicated function of the trap frequency ω, distance from the ion to electrode surfaces d, and trap temperature T. In most experimental studies, however, only a local parameter range can be scanned. Under this restriction, the spectral density is assumed to follow a power-law scaling with respect to ω, d, and T [6]

$$S_E(\omega, d, T) \sim \omega^{-\alpha} d^{-\beta} T^{\gamma}. \tag{6.6}$$

The predicted values of α, β, and γ vary depending on the theoretical noise model and the respective parameter regime. Many physical noise models have been considered in the literature, including blackbody radiation, electromagnetic pick-up, patch potentials, two-level fluctuators, adatom dipoles, adatom diffusion, Johnson noise, and technical noise [6], and much experimental data in regards to the spectral density has been published. Unfortunately, solid conclusions are difficult to draw from the collection of data, as the measurement conditions drastically vary among experiments. To solve this, an ideal experiment for understanding electric-field noise in ion traps would allow for measurement of S_E as a function of ω, d, and T, with a large workable range for each parameter. To this end, some of the experiments performed in this thesis aim to collectively measure the ω and d dependencies in a single ion trap.

6.2 Distance scaling

6.2.1 Previous experiments

At present, a small number of experiments have directly measured electric-field noise as a function of the ion-surface distance. The first of these were performed in traps with non-planar geometries, using needle-shaped tungsten electrodes in one case [75] and a gold-plated 'stylus trap' design in the other [76]. These experiments found electric-field noise scalings of $\beta = 3.5$ [75] and $\beta = 3.1$ [77], respectively. More recently, two additional experiments employed planar surface traps for distance scaling measurements of noise parallel to the trap surface. The first study used a standard five-wire trap with gold electrodes and application of radio-frequency (RF) voltages to the central three electrodes to obtain a distance-scaling exponent of $\beta = 3.8$ [48]. The magnitude of electric-field noise in this experiment was about an order of magnitude higher than the best published results for untreated surface traps. The second study found $\beta = 4.0$ for a multizone niobium surface trap [49]. Here, the ion trap contained several trapping zones spaced on the order of 1 mm, where the electrodes at each zone were physically scaled to trap ions at different distances from the surface. The magnitude of electric-field noise was comparable to very good untreated surface traps. Collectively, these previous measurements are naively consistent with a noise mechanism of microscopic nature, i.e. the length scale of the electric-field noise fluctuations are much smaller than the ion-surface distance.

6.2.2 Experimental Overview

In our experiment, we investigate the electric-field noise as a function of ion-surface distance for a single $^{40}Ca^{+}$ ion trapped in a unique surface Paul trap with a simple planar geometry. Our room-temperature elevator trap enables tuning of the ion-surface distance at a fixed planar position using DC voltages [30]. Furthermore, we find that the magnitude of noise for this trap is comparable to the best untreated traps. We measure electric-field noise in both

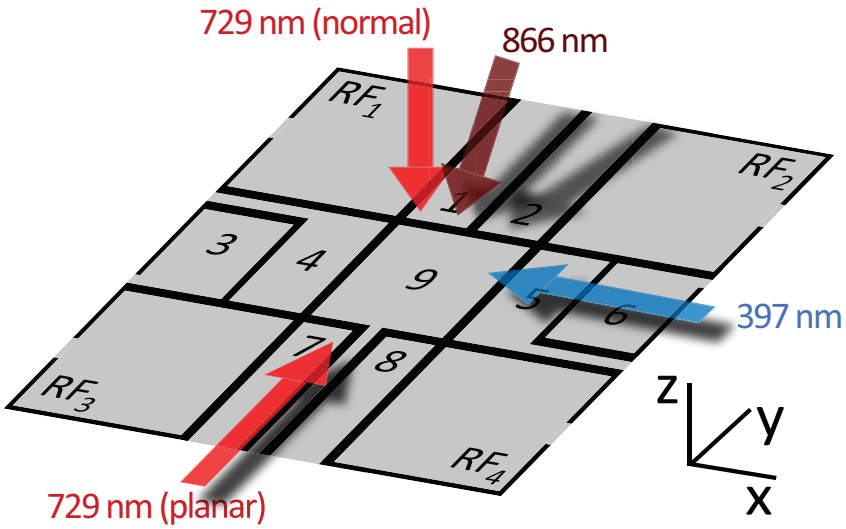

Figure 6.1: Isometric view of the trapping region of the elevator trap. Static voltages are applied to numerically labeled DC electrodes, and RF electrodes are labeled RF_{1-4}. $RF_{1,4}$ are driven out-of-phase relative to $RF_{2,3}$. The orientation of the qubit addressing laser beam (729 nm) and Doppler cooling beams (397 nm and 866 nm) are indicated by the arrows and their labels.

the normal and planar directions with respect to the surface and extract a distance scaling exponent of $\beta \approx 2.6$ for ion-surface distances in the range of 50 - 300 µm, significantly departing from the previous measurements discussed above. In Section 6.4, we provide evidence that the measured field noise is not limited by technical noise (defined to be noise whose origin is external to the properties of the trap surface, for example, from power supplies or electromagnetic pickup). Following that, we discuss in Section 6.5 how spatial correlations of the surface noise may explain our observed distance dependency. Finally, we place the results in a larger context with respect to previous measurements in Section 6.6.

6.2.3 Experimental Setup and Methods

Experimental Setup

We first reiterate the functionality of our elevator trap, shown in Fig. 6.1, which is operated with an out-of-phase RF drive such that the two diagonal pairs of RF electrodes ($RF_{1,4}$ and $RF_{2,3}$) are driven with the same amplitude, but opposite phase. This generates a radio-frequency-null along the axis normal to the trap surface [30]. Thus, the trapping potential in this direction is fully controlled with DC electrodes (labeled 1 to 9 in Fig. 6.1), allowing for continuous variation of the ion-surface distance without introducing excess micromotion. RF fields provide confinement in the xy plane parallel to the trap.

We adjust the DC voltages such that the principal axes of the total potential have a tilt

of 5° with respect both the z and y-axes. This ensures that all three motional modes have some projection onto the 397 nm Doppler cooling beam propagating along $\hat{x}$. To provide additional cooling for the near-normal mode, the repumping 866 nm beam is sent in at a near-normal angle with respect to the trap surface (z axis) and detuned red with respect to resonance.

The beam at 729-nm wavelength addressing the long-lived quadrupole qubit transition of $^{40}Ca^{+}$ can be switched between two orientations to measure the ion's response to electric-field noise in two directions. The '729 nm (normal)' orientation in Fig. 6.1 is used for measuring noise normal to the trap surface (along the $\hat{z}$-direction), while the '729 nm (planar)' orientation allows noise measurements in the $\hat{y}$-direction of the trap plane.

Measurement Methods

As the strength of electric-field noise changes by two orders of magnitude over the ion-surface distance explored here, we employ two methods for measuring heating rates. When the ion is cooled close to the motional ground state, that is $\bar{n} \leq 1$ (possible if $\dot{\bar{n}} \lesssim 1000\ \mathrm{s}^{-1}$ for our system), the amplitude of the phonon-subtracting transition (red sideband) is significantly less than that of phonon-adding one (blue sideband). Then, the mean phonon number $\bar{n}$ can reliably be found by comparing the excitation amplitude of red and blue first-order motional sidebands [41]. When cooling into the ground state is difficult ($\dot{\bar{n}} \gtrsim 1000\ \mathrm{s}^{-1}$), the sideband method is no longer sensitive to $\bar{n}$. In this regime, a better measure of the heating rate is via the decay of carrier Rabi oscillations [78], with coupling strength given by Eq. (3.15). These carrier Rabi flops can be fitted to extract the thermal motional distribution parameterized by $\bar{n}$ and thereby the heating rate $\dot{\bar{n}}$.

6.2.4 Experimental results

The scaling of electric-field noise with d is determined from measurements of the heating rate at a fixed secular frequency of $\omega = 2\pi \times 1.00$ MHz. The two planar motional modes are closely aligned with the x and y-axes and we measure the heating rate of the $\hat{y}$ planar mode. Using DC voltages, the $\hat{x}$ planar mode is set higher in frequency by typically $2\pi \times 50$ kHz than the $\hat{y}$ mode frequency. When measuring the planar mode at $2\pi \times 1$ MHz, the normal $\hat{z}$ mode is set to about $2\pi \times 0.75$ MHz, while for measurements of the normal mode at $2\pi \times 1$ MHz, the planar mode frequencies are tuned to about $2\pi \times 1.25$ MHz. The range of ion-electrode distances accessible with the trap is limited by the high RF voltages needed when trapping close to and far away from the surface [30]. Additionally, we find that when the normal 729 nm beam is focused close to the trap surface, back-reflections generate a standing wave pattern which significantly modulates the intensity in the $\hat{z}$ direction. Intensity fluctuations caused by drifts in the standing wave pattern limit the ion-surface distances where we can reliably measure electric-field noise in the normal direction to above 60 µm.

The heating rates for the planar (blue symbols) and normal (red symbols) mode are plotted in Fig. 6.2. We distinguish between the two measurement methods mentioned earlier:

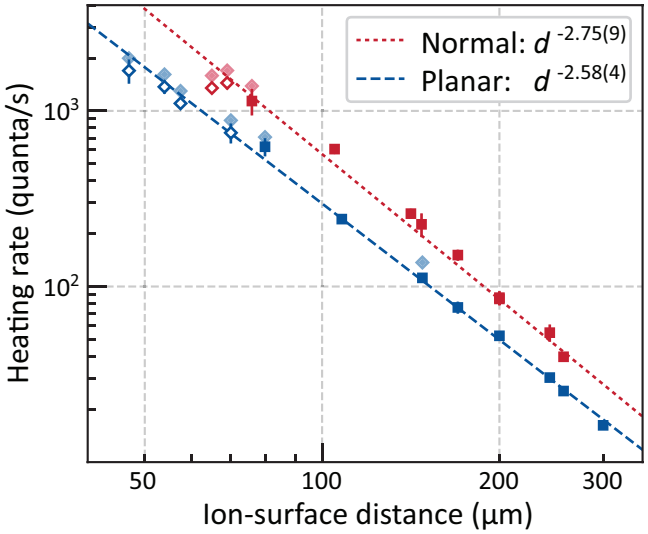

Figure 6.2: Planar (blue) and normal (red) heating rates as a function of ion-surface distance for a fixed secular frequency of $\omega_t = 2\pi \times 1$ MHz. Data are taken with two measurement methods: (■) sideband method, (◆) Rabi method. (◇) show data from the Rabi method scaled to match results from the sideband method (see details in Sec. 6.2.4). Power-law fits for both motional modes take into account the data taken with the sideband-asymmetry (■) method and the scaled Rabi method (◇).

filled squares (■) correspond to measurements taken with the sideband method. Below 80 µm ion-surface distance, the carrier Rabi-oscillation method is used instead, and the raw heating rate data are marked with filled diamonds (◆).

To validate the compatibility of the two methods, we compare both measurement techniques in the intermediate regime of $\dot{\bar{n}} \sim 1000$ s^{-1} and also for $\dot{\bar{n}} \sim 100$ s^{-1}. We find that the Rabi method gives heating rates that are systematically about 17% higher than for the sideband-asymmetry method. This difference is consistent with findings from other groups [26, 49] and may be linked to the non-zero projection of other motional modes on the measurement laser or laser intensity noise, which manifests as premature dephasing of the Rabi oscillations. To simplify comparison of the electric-field noise across the full range of ion-surface distances, we scale the data from the Rabi-oscillation method by a constant factor of 0.85. The resulting adjusted values are marked in Fig. 6.2 as open diamonds (◇).

Power-law fits to the filled squares (■) and open diamonds (◇) are shown as dashed lines in Fig. 6.2. We observe a scaling of $\dot{\bar{n}} \sim d^{-2.6}$ for both modes, with normal heating rates consistently about a factor two higher than planar heating rates.

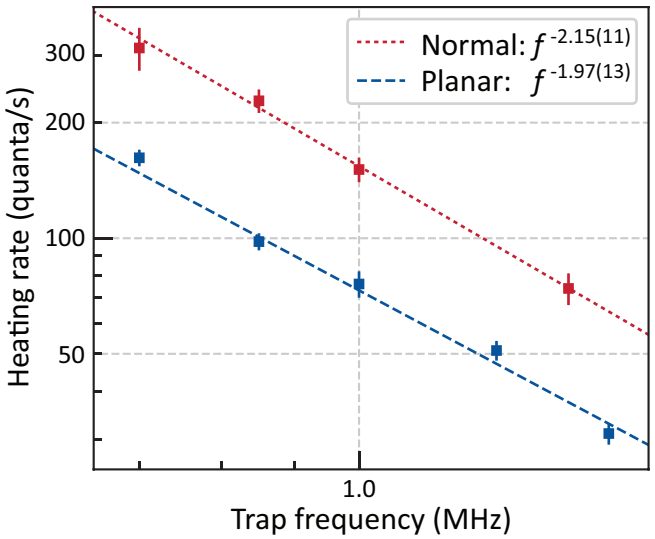

Figure 6.3: (b) Planar (blue) and normal (red) heating rates as a function of secular frequency for a fixed ion-surface separation of $d = 170$ µm. Power-law fits for both modes are shown as dashed and dotted lines.

6.3 Frequency scaling

In addition to the distance scaling, we measure the scaling of noise with frequency, which is another key parameter to characterize the electric-field noise. In Fig. 6.3 we show the noise frequency dependence of both normal and planar modes at a fixed ion-surface distance of 170 µm, where all measurements are performed with the sideband-asymmetry method. From a power-law fit of the data and Eq. (6.1), we find that the electric-field noise spectral density, $S_E(2\pi \times f, d)$, scales as $f^{-0.97(13)}$ and $f^{-1.15(11)}$ for the planar and normal modes, respectively. This frequency dependence is consistent with $1/f$-noise that is ubiquitous in solid-state experiments [79] and a number of ion trapping experiments [6]. We observe again that the normal heating rates are about a factor of two higher than the planar heating rates. Additionally, we measure the frequency scaling of the planar electric-field noise at 70 µm ion-surface distance and find $S_E(2\pi \times f, d) \propto f^{-1.2(3)}$. The $1/f$-like noise scaling for different ion-surface distances and electric-field projections in our system suggests that our measurements are not described by proposed models for noise from adatom dipole fluctuations [80] or adatom diffusion [81], or by broadband technical noise [6] since the expected frequency scaling in these cases is not $1/f$.

6.4 Technical noise

Having presented our measurement results, we note that the distance scaling for this ion trap differs strongly from the d^{-4} dependence that for planar trap geometries is expected from

microscopic noise sources and has been observed in recent experiments [48, 49]. A scaling exponent of $\beta \approx 2$ is commonly associated with technical noise; however, this scaling only appears if the trap size is scaled with the ion-surface distance. This is not the case in our system. Thus, understanding how technical noise manifests in this trap and determining to what degree it affects our measurements are critical issues that we address in the following.

Two types of electric-field noise sources at the ion secular trap frequency can affect the motional ion heating: surface noise and technical noise. Surface noise encompasses the mechanisms originating from the ion trap surface itself, that is, physical processes generating noise at the trap surface. Technical noise is defined as noise whose origin is external to the properties of the trap surface, and thus can be mitigated by proper filtering and shielding. Technical noise may be caused by noise from voltages sources powering the ion trap or electromagnetic radiation in the environment which is picked up by the trap electronics and electrodes. This type of noise is typically correlated over the area of trap electrodes, and thus depends specifically on the trap electrode geometry and the ion's position relative to the electrodes. As we are interested in the fundamental physical noise sources that could limit the performance of trapped ion qubits, it is important that our electric-field noise measurements are dominated by surface noise. Therefore we perform several checks to verify that our heating rates are not limited by technical noise.

We can translate the contribution of technical noise to the heating rate of an ion as

$$\dot{\bar{n}}_{tech} = \frac{e^2}{4m\hbar\omega_k} \sum_e \frac{S_{V_e}(\omega_k)}{D_{e,k}^2}, \tag{6.7}$$

where $S_{V_e}(\omega_k)$ is the voltage noise spectral density on electrode e and $D_{e,k}$ is the characteristic ion-electrode distance defined by

$$D_{e,k} = \frac{V_e}{E_k}, \tag{6.8}$$

where V_e is the applied voltage on electrode e and E_k is the resulting electric field at the ion position in the $\hat{k}$ motional mode axis. Relating this to the electric-field spectral density, S_E that we have been discussing, we find the general relation,

$$S_{E_e}(\omega_k) = \frac{S_{V_e}(\omega_k)}{D_{e,k}^2}. \tag{6.9}$$

This relation is often naively cited in the literature to infer that technical noise scales as $S_E \sim d^{-2}$. However, it is not generally true that a $D_{e,k}^{-2}$ scaling implies a d^{-2} scaling, as the former is a characteristic distance with dependence defined in Eq. (6.8) and the latter is simply a physical ion-electrode distance. In order to extract the true distance scaling, we must understand the behavior of the electric-field, E_k, as a function of the distance, d.

One particular instance where the simple $D_{e,k}^{-2} \sim d^{-2}$ relation does hold, is if a full surface trap electrode architecture is scaled uniformly. In this case, as the electrode sizes increase (decrease), the location of the RF-null, i.e. ion height d, increases (decreases) proportionally. This particular setup has been experimentally demonstrated by Sedlacek et. al. [49], where

they inject technical noise into five different zones of a surface trap, where each zone is essentially a scaled model of the others. They measure a distance scaling of $d^{-2.4\pm0.3}$ with controlled technical noise injected into particular electrodes.

6.4.1 Electrode noise simulations

Individual electrodes

For each trap electrode, we simulate $S_{E,i}$ as a function of the ion-surface distance under the assumption that technical noise dominates at the ion position. E_i is analytically approximated by a method which assumes an infinite ground plane surrounding electrode i [45, 82]. From the geometry of our trap (cf. Fig. 6.1), we see that only electrodes 1, 2, 7, 8, 9, and RF_{1-4} generate electric fields with projection onto both the y and z axes, which correspond to the directions of the measured ion motional modes. Also, from the symmetry of our trap, we expect electrodes 1, 2, 7, and 8 to generate similarly polarized electric-field noise in the yz plane, as is the case for all four RF electrodes. So, we will discuss here the distance scaling for the relevant cases of electrodes 1, 9, and RF_1. Fig. 6.4 visualizes the simulated electric-field noise in the planar and normal directions for 3-µV noise amplitude on DC electrodes 1 through 9 while Fig. 6.5 shows the same simulation with the RF_1 electrode geometry. The simulated distance scalings confirm our intuitive expectation: For electrode 9, the center electrode, the planar electric-field components mostly cancel from symmetry, such that the field is mostly normal to the surface. For all the outer electrodes, including 1 and RF_1, the normal electric-field vector changes sign when d is near the approximate separation between the electrode in question and the trap center. The electric-field vector points away from the trap surface when d is greater than the trap-center-to-electrode separation and points towards the trap surface at lower distances. Hence, the normal components in Fig. 6.4(top left) and Fig. 6.5 show dips at about 180 µm and about 250 µm for electrodes 1 and RF_1, respectively. Very close to the conductive trap surface, the electric-field vector must be normal to the surface, thus reducing the planar component, which we observe in all cases of Fig. 6.4 and Fig 6.5.

Comparing the simulations with the overlaid scaled data, we find none of the cases match the data. Similarities are only partial and do not apply simultaneously to both projections of noise. In general, for correlated noise from trap electrodes, the electric-field noise polarization as a function of the ion-electrode distance is not constant, that is, the ratio of the noise magnitudes in normal and planar directions is not constant, in contrast to our data. Thus, we conclude that no single electrode can generate noise consistent with our measured electric-field noise data.

Combinations of electrodes

Beyond noise from individual electrodes, one could imagine technical noise contributions with various amplitudes from all electrodes to play a role, conspiring to give rise to the

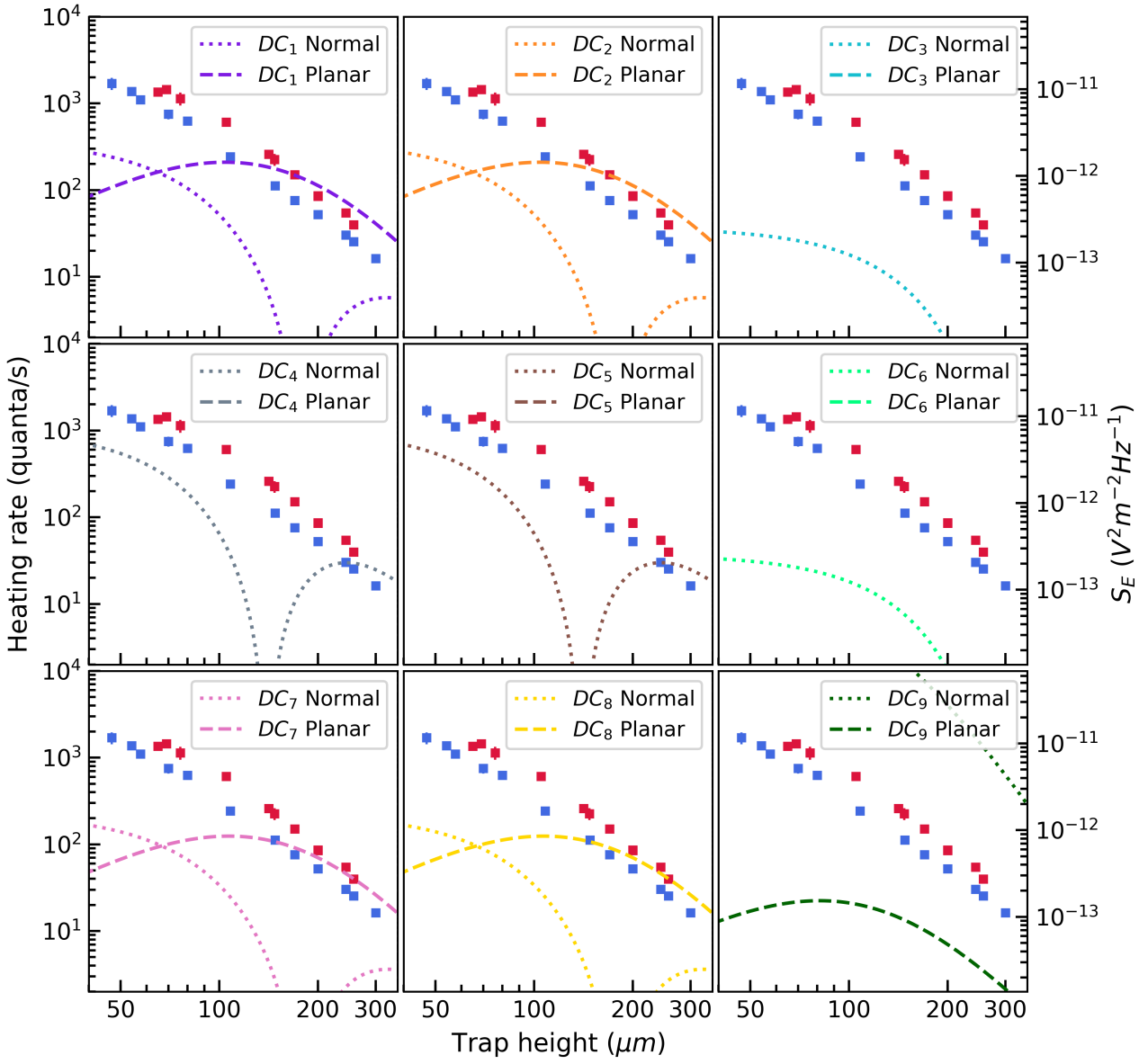

Figure 6.4: Simulated S_E distance scaling from 3-μV amplitude noise on DC electrodes 1 through 9. The planar contributions are shown as dashed curves and the normal contributions are shown as dotted curves. Plots for DC electrodes 3, 4, 5, and 6 do not display dashed curves because the planar noise contributions are negligible. Scaled data measurements are overlaid for reference.

particular distance dependence we measure. To check the possibility of such a scenario we fit the measurements with a linear combination of contributions from all electrodes, assuming noise from each electrode is uncorrelated with the others. Even for this contrived scenario,

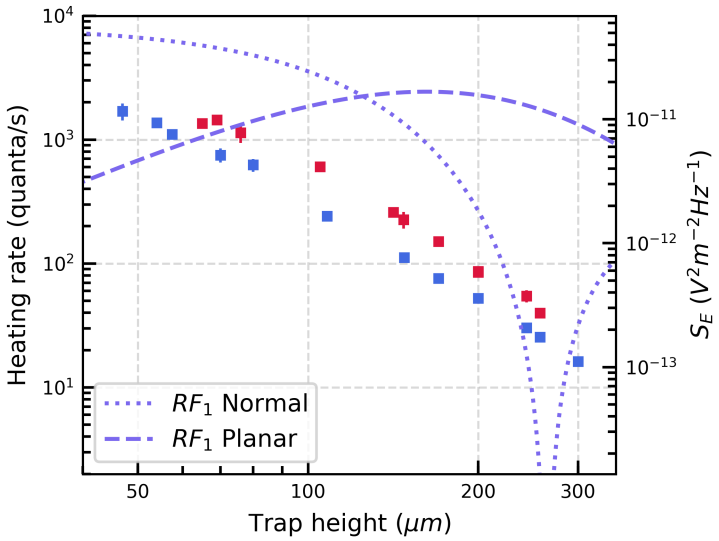

Figure 6.5: Simulated S_E distance scaling from 3-μV amplitude noise on RF electrode RF_1. The scaling is similar for all RF electrodes. The planar contributions are shown as dashed curves and the normal contributions are shown as dotted curves. Scaled data measurements are overlaid for reference.

see fit in Fig. 6.6, we do not find any agreement with our data.

This may seems counter-intuitive at first, since the fits have 10 degrees of freedom (one for each distinct electrode). However, the heating rate distance scalings derived from each electrode are strongly correlated, meaning our 10 degrees of freedom are not independent. This leads to necessary features in the linear combination, such as the dip in noise in the normal direction seen in Fig. 6.6 around 180 μm ion-surface distance, and a fundamental inability to accurately fit to the measured data.

Furthermore, allowing correlations between multiple electrodes does not yield better fits to our data. This is expected from our intuition above, as the electric-field vectors from correlated electrodes can be added together. In general terms, correlating multiple electrodes will increase noise in the normal direction and introduce a preferred orientation of the electric-field in the trap plane.

Given the strong disagreement between the simulated noise from electrodes and our experimental results, we conclude that our measurements are not limited by technical noise correlated over the area of individual or multiple trap electrodes. These arguments also hold for electromagnetic pickup and Johnson noise on the voltage supply and filter electronics, since we expect noise sources of these types to be correlated over the area of electrodes as well. We have performed an additional test where we deliberately inject noise on electrode 7 and measure the distance scaling. The results are described in Section 6.4.2 and confirm our assessment above.

Other types of technical noise considered in the literature [6] include direct interaction

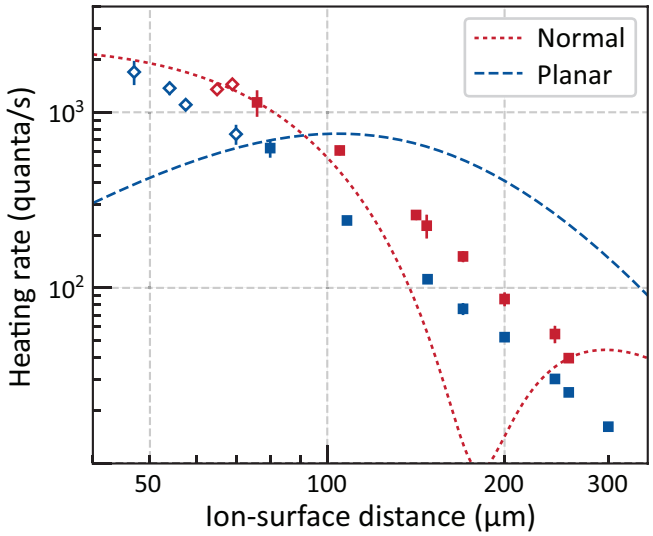

Figure 6.6: Simultaneous fit of the measured distance dependence for planar and normal motional modes assuming motional heating is caused by technical noise from all electrodes. The voltages on different electrodes are assumed to fluctuate independently from each other such that the fit is parameterized by the amplitudes of noise on each electrode.

of the trapped ion with electromagnetic interference and space charges. We tested for electromagnetic interference by adding a Faraday cage around the vacuum chamber and found no effect on the heating rates. Space charges due to field emission from the trap electrodes should depend on the applied voltages, but we also found no dependence of heating rates on DC voltages and RF power.

In addition to noise at the secular trap frequency, ω, the ion may also be sensitive to technical noise at $\Omega_{RF} \pm \omega$. In our measurements, we expect this effect on the heating rate to be small, since we take care to minimize the ion's micromotion in both the normal and planar directions (see Ref. [30]). To confirm the absence of $\Omega_{RF} \pm \omega$ noise in our system, we deliberately increase the pseudopotential gradient (in both modes) and find no effect on the heating rate.

6.4.2 Technical noise injection

To experimentally validate the technical noise simulations from Section 6.4.1, we measure the effect of injecting white noise into the system, employing a technique that has been used in experiments at MIT Lincoln Laboratory and our own lab at University of California, Berkeley [46, 49, 83]. Electrode 7, see Fig. 6.1, is chosen for this purpose. Voltage noise is generated with a RIGOL DG4162 arbitrary waveform generator, which produces white noise in the 10 Hz to 100 MHz band. When choosing a noise source, it is important to measure the frequency spectrum around the trap frequency, as some signal generators, such as Agilent 33220A, do not have exactly flat noise spectra around typical ion trap frequencies.

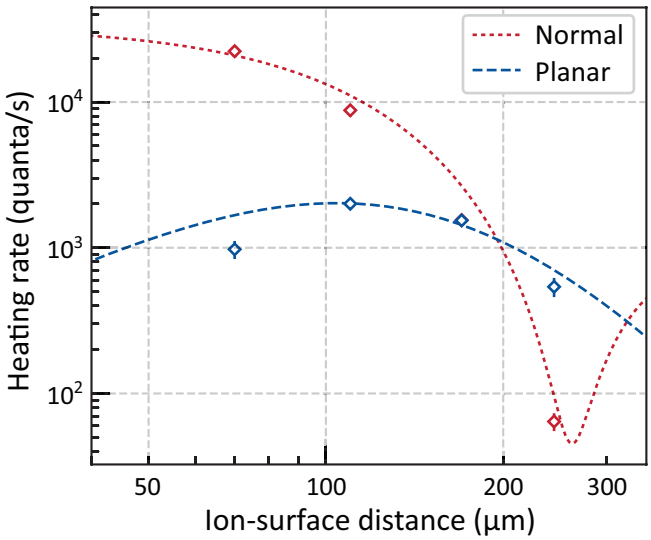

Figure 6.7: Planar (blue) and normal (red) heating rate contributions from injected technical noise. Measurements are performed with the scaled Rabi method (◇). Results from Fig. 6.2 provide baseline heating rates. The data shown are the isolated heating rates due to injected noise, derived by subtracting the corresponding baseline values from the raw measured values with injected noise. Dashed curves show the distance scaling from technical noise in both the planar and normal directions when fitting the data to the technical noise simulation (see text).

Preliminary attempts at the injection utilized a band-pass filter centered around 1 MHz, but did not induce any significant rise in ion heating rates. The band-pass was replaced with an in-line 22 pF capacitor, which acts as a high-pass filter as not to accidentally bias the static DC fields.

To isolate the heating rate contributions due to the injected noise from surface noise we subtract the heating rates measured when no noise is injected. We first verify that the baseline-corrected heating rates scale with the square of the noise voltage and then measure the noise scaling for ion-surface distances between 70 and about 245 μm. Fig. 6.7 shows the resulting data in both planar and normal directions as open diamonds.

We find that the measurements can be reproduced in our technical noise simulations for a noise voltage of 9.3 μV on electrode 7 and, additionally, voltage noise with 8.5 μV amplitude that is correlated on the four RF electrodes. The distance scaling for these parameters is shown as dashed curves in Fig. 6.7. We note that the correlated noise on the four RF electrodes cancels in the planar direction due to symmetry, in contrast to noise from a single RF electrode, which we discussed in Fig. 6.5.

The reason for seeing noise on the RF electrodes when injecting noise on to any DC electrode lies in the filtering required for operating the out-of-phase drive in our setup. The trap ground is defined by the ground electrode on the trap chip which has some impedance to the true experiment ground outside of the vacuum chamber. Capacitive filtering of the

injected noise to the trap ground then causes the trap ground to fluctuate with respect to the true ground. The RF electrodes are referenced to the trap ground via a 100 mH inductor [30], however, providing a good reference at very low frequencies, but a high impedance at 1 MHz. Then, from the ion's perspective the RF electrodes are noisy relative to the trap ground. These measurements support arguments in Section 6.4 that we are not limited by technical noise from noise correlated across the area of electrodes.

6.5 Spatial surface noise correlations

In light of the strong evidence for uncorrelated microscopic noise sources in ion traps given by the observed d^{-4} scaling in previous measurements [48, 49, 84], it is surprising that our results ($\sim d^{-2.6}$) deviate so clearly from this scaling. We have shown in the last section that measurements in our trap are very likely not limited by technical noise, leading us to conclude that we must be observing surface noise. There are immediate questions as to how such a scaling can arise, what the noise sources are, and why this trap behaves differently compared to others. In the following we concentrate on the first of these questions.

A general model for surface noise with finite correlations considers metallic surfaces to be covered with patches of varying potential [7]. Physically, patches may arise from work function differences across crystal grains, locally varying strain, surface roughness, or adsorption of atoms and more complex compounds on the surface [85]. Fluctuations in the patch potentials (amplitude or size) lead to electric-field noise then. In the 'patch-potential' picture, the behavior of electric-field noise is quantified by a spatial length scale, ζ, over which the surface fluctuations are correlated. While the model exists independently of the physical origins of the patches, and as such does not constrain the frequency or temperature scaling of the noise, a certain correlation length may support the presence of specific noise sources over others.

In the limit of spatial correlations that are very small compared to the ion-surface distance, $\zeta \ll d$, the electric-field noise from different locations on the surface stems from independent microscopic noisy patches and adds in quadrature at the ion position. Then, for a planar trap geometry, the electric-field magnitude scales as d^{-4} with distance. Further, there is a polarization to the electric-field noise such that the projection on the normal direction is twice that for the planar directions [9, 46]. In the opposite limit of very large spatial correlations, $\zeta \gg d$, the fields only vary weakly with distance from the surface. Depending on the specific arrangement of patches or the form of the spatial correlation function, the noise may, for instance, be independent of distance or scale as d^{-1} and the noise may be strongly polarized in the normal direction. At intermediate distances, the scaling coefficient varies smoothly from one limit to the other.

Measurements of the electric-field noise distance scaling then probe the spatial extent of noise correlations on the surface. With regard to our data, the measured scaling exponent of $\beta = 2.6$ being smaller than $\beta = 4$ may be taken as an indication of macroscopic correlation lengths, as compared to the ion-surface distance. To further understand the role of the

correlation length ζ in describing our data, we will review a general framework for modeling correlated patch-potentials and also give an example for a specific physical realization of patch potentials in our surface trap.

6.5.1 Analytic model

Starting from the characteristic length, ζ, over which the noisy potential patches are correlated, we can explicitly calculate the electric-field noise spectral density vector following Refs. [8, 9, 86]. We assume an exponential spatial autocorrelation function,

$$C_\zeta = e^{-\sqrt{x^2+y^2}/\zeta}, \tag{6.10}$$

which arises naturally from random variations of a variable in two or three dimensions, for instance in Poisson-Voronoi tessellations [87, 88]. Then, the expected planar noise spectral density S_E^p is given by

$$S_E^p(\omega_t, d) = 2\frac{N\zeta^2}{d} S_V(\omega_t) \int_0^\infty dk \frac{k^3 e^{-2k}}{(d^2+\zeta^2 k^2)^{3/2}} , \tag{6.11}$$

and the spectral density of noise in the normal direction is higher by a factor of two.

With this analytic model, we find that for $\zeta \ll d$, we recover d^{-4} scaling for both the planar and normal heating rates, as expected from similar microscopic noise models. As the ratio between d and ζ inverts, there is a smooth transition in the exponent of the power law towards the limiting case of $\zeta \gg d$, where the distance scaling approaches a d^{-1} behavior.

We use Eq. (6.11) to simultaneously fit both the measured planar and normal distance scalings (see Fig. 6.8), and extract a correlation length of $\zeta = 106$ µm. This provides a good fit to the data, that is comparable to the power-law fit with $\beta = 2.6$ from Fig. 6.2.

While we can describe our data with a single parameter, the correlation length, the same autocorrelation function can arise from many distinct patch configurations. The curves in Fig. 6.8 effectively show the distance scaling for an average over all patch configurations with the same correlation length. Reproducing this exact scaling with well-defined patches at the trap surface would require either a superposition of overlapping patches or fast switching of patch configurations.

Neither scenario is likely to manifest on a simple metallic surface, but the trap used here has a considerably more complex structure. The combination of features like an oxide layer [89] on the aluminium-copper electrodes, adsorbates on the surface, and the influence of surface roughness [90], may allow for more complex arrangements of charges and fluctuating dipoles. The presence of an insulating layer (the oxide), for example, could separate patch potentials both above and below it, creating a structure of overlapping patches. One might also imagine dynamic patches that shift, rearrange or reassemble on timescales much faster than the experiment (of order one second) [91]. Measuring the surface potentials of this trap directly with a technique like Kelvin probe or scanning tunneling microscopy may provide additional insight on the noise origin.

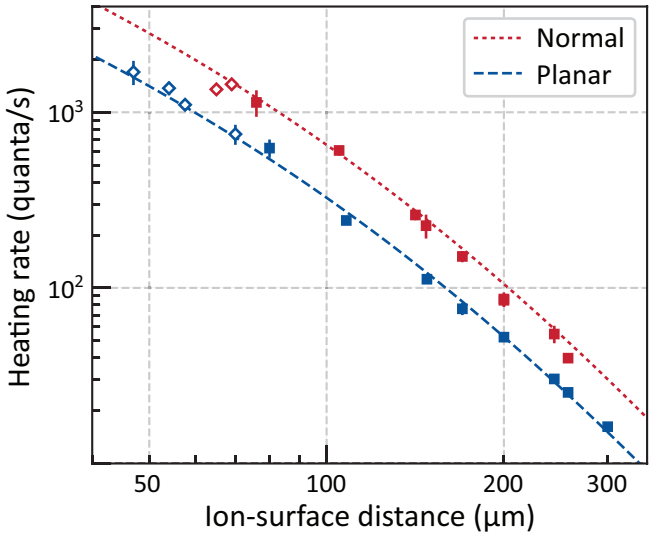

Figure 6.8: Heating rate as a function of distance with a fit based on exponential spatial noise correlations. Fitting both data sets to Eq. (6.11) gives a characteristic length $\zeta = 106$ μm.

The general correlation length model used here also assumes an infinite planar metallic surface, which does not quite translate to our surface trap that is composed of many planar electrodes separated by 20-μm wide trenches. Such gaps between conducting surfaces should act as natural boundaries over which noise correlations cannot be established.

6.5.2 Fixed patch potentials

For a more concrete realization of a noise correlation length, we consider non-overlapping patches of fixed size and position while imposing the constraint that correlations cannot form across electrode boundaries. We generate many random patch configurations based on bounded two-dimensional Poisson-Voronoi diagrams with a fixed number of patches in a 4 mm^2 area around the trap center [92]. We can extract a correlation length for a particular patch configuration via an exponential fit to its calculated spatial autocorrelation function [88]. An example configuration with 100 patches is shown in Fig. 6.9(a), where the corresponding correlation length is $\zeta = 140$ μm.

Each patch is assumed to generate noise independently of other patches and the noise amplitude on each patch is a parameter for fitting the patch potential distance scaling to our data. The fit result for the example patch configuration in Fig. 6.9(a) is shown in Fig. 6.9(b). A consequence of moving from the analytic correlation length model (previous subsection, Fig. 6.8) to a defined tiling of patches is a general anisotropy of noise in different planar directions, as exemplified by the noise spectral densities 'Planar X' and 'Planar Y' in Fig. 6.9(b). Here the simulated 'Planar Y' and 'Normal' distance scaling matches the data well, but this is not a unique solution. Many patch configurations with similar average patch sizes reproduce fit results similar to the example given in Fig. 6.9. Among these well fitting

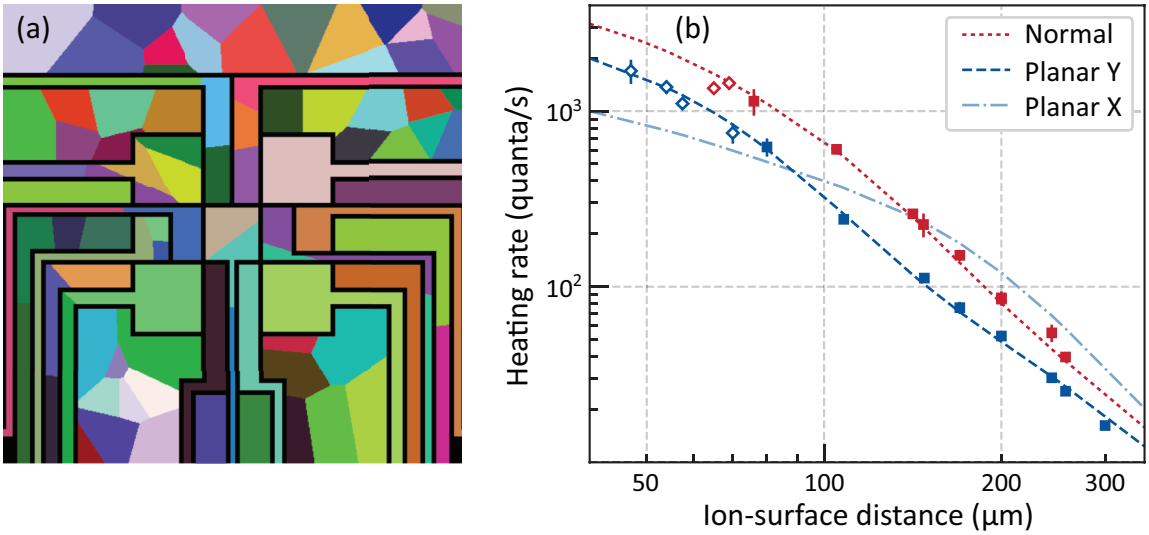

Figure 6.9: (a) Example of a randomly generated patch configuration based on Poisson-Voronoi tesselation with a calculated correlation length $\zeta = 140$ µm. (b) Weighted sequential least squares fit to experimental data for the distance scaling in the 'Planar Y' and 'Normal' direction based on the patch configuration in (a) and variable voltage amplitude on the patches. The ratio between the largest and smallest voltage is constrained to be less than four. The 'Planar X' distance scaling takes no part in the fit, but is shown to demonstrate the noise anisotropy in the planar directions.

configurations, we find that the center electrode, DC 9, must contain at least two patches, else the distance scaling behaves similarly to the technical noise case shown in Fig. 6.4(bottom right). Matching distance scalings in the planar X and Y directions can be found when the center electrode is diagonally bisected by two patches, or when it contains several patches that meet close to the electrode center.

Comparing the fixed patch configuration to the general correlation length picture, we observe that the constraints posed by the electrode geometry lead to slightly longer correlation lengths, but still ζ is about 100 µm. The key difference, as explained earlier, lies in the expected polarization of electric-field noise. The general model in Sec. 6.5.1 is an effective averaging over many random configurations, without preferential patch orientations. Thus, the electric-field noise is isotropic in all planar directions. In contrast, the fixed patch configuration generally features different electric-field noise in the planar directions.

We measured the planar electric-field noise in both the y and $x + y$-directions at an ion-surface distance of 170 µm and found them to be the same within the experimental uncertainty, ruling out some patch configurations that otherwise fit the observed distance scaling in the y-direction alone. Further work on measuring the electric-field noise in three dimensions would be needed in order to achieve a better understanding of the nature of noise correlations in this trap.

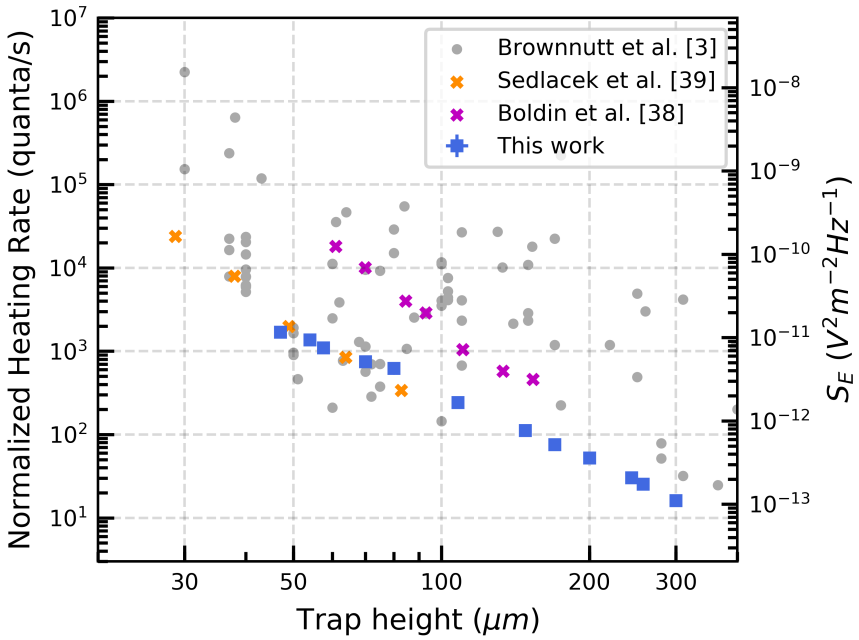

Figure 6.10: Comparison of the heating rates in this paper with those of other ion traps. The filled gray circles reproduce the data compiled in Ref. [6] for single-ion motional heating, with the exception of surface-treated traps. Blue (dark) and yellow (light) crosses show the results of distance scaling measurements in the same trap from Ref. [48] and Ref. [49], respectively.

6.6 Heating rate comparison

Finally we look at the magnitude of electric-field noise in our trap compared to other measurements in the community. Data collected in the review of Brownnutt et *al.* [6] form the basis of comparison, see Fig. 6.10, where we also included the recent data from Ref. [48] and Ref. [49] (highlighted as colored crosses). All data shown have been taken in room temperature traps with untreated surfaces. Following the convention in Ref. [6], both the heating rate and the electric field spectral noise density are scaled to $2\pi \times 1$ MHz secular frequency, assuming $S_E \propto \omega^{-1}$. Additionally, the heating rate is scaled to correspond to the case of a $^{40}Ca^+$ ion.

In comparison to all data on the plot, our heating rates are on the low end across the measured ion-surface distances. Looking specifically at the measurements for distance scalings performed in the same trap, our results are about a factor 5 - 20 lower than the ones reported by Boldin et *al.* [48], and of similar magnitude to measurements of Sedlacek et *al.* [49].

The similarities in the absolute noise magnitudes between the traps is also interesting, since one would generally expect that, given some density of microscopic noise sources, longer correlation lengths should increase the noise magnitude in our device.

Regardless of the physical origin of noise in the different traps, it is worth noting that with

regards to device miniaturization, the distance scaling we observe ($d^{-2.6}$) scales favourably compared to the d^{-4} dependence observed in other traps. This observation provides us with some motivation to understand the origin of noise in this device and work towards further miniaturization of ion traps.

6.7 Concluding remarks

To summarize, we have presented measurements of the distance scaling of electric-field noise in a surface ion trap, together with measurements of the frequency dependence. In contrast to previous results, the noise distance scaling for our trap is described by a $d^{-2.6}$ power-law behaviour. The data cannot be explained by noise from independent microscopic sources at the surface; we require the addition of a macroscopic length scale for the noise that extends to about 100 µm. The presence of a macroscopic length scale indicates a non-trivial surface structure and/or correlated dynamics of noise sources taking place at the trap electrode. We note that our results do not rule out microscopic noise sources, if they can give rise to spatially correlated dynamics at the frequencies of our measurements. Further, some abstract noise models, for instance the thermally activated two-level systems commonly used to explain $1/f$ noise [93, 79], are agnostic to distance scaling, as they only consider temperature and frequency [94]. In contrast, the patch potential model used here only considers spatial noise correlations, but not the frequency or temperature properties. A self-consistent description of the noise dependence on frequency, temperature and distance at the same time likely requires identifying a physical system (or several [84]) in place of an abstract model. In conclusion, our results add to the growing body of experimental results on electric-field noise in ion traps, and specifically show that the scaling of electric-field noise with distance is not universal in surface traps of similar size.

6.8 Two-ion motional heating

Up to now, we have focused on the one-dimensional heating rate of a single ion, which has eigenstates of motion that are characterized by the trap frequencies of the principal axes. As we scale up to multiple ions, e.g. in a linear chain, additional motional degrees of freedom are introduced, and the eigenstates of motion become more complex. These new eigenstates allow us to probe different projections of electric-field noise, which may aid in determining its origins. In this section, we will step through the case of a two-ion linear chain to demonstrate the potential advantage of heating measurements with multiple ions. We also offer a general formulation for multi-ion heating rates, which follows closely from the single ion analysis done in Section 6.1.

Figure 6.11: Illustration of normal modes oriented along the axial direction for a two ion chain.

6.8.1 Theory

Let's focus on the axial direction of a two-ion string, which has separation given by

$$d_{ion-ion} = \left(\frac{e^2}{2\pi\epsilon_0 m\omega_z^2}\right)^{\frac{1}{3}}, \tag{6.12}$$

which is ~ 5 µm at $\omega_z = 2\pi \times 1$ MHz axial trap frequency. In this dimension, there are two modes of motion, shown in Fig. 6.11, which are termed as the center-of-mass (COM) mode and the stretch/breathing mode. From the illustrations, we can see that the COM mode is mostly sensitive to dipole electric-field noise, whereas the stretch mode is mostly sensitive to quadrupole noise. The general form for the heating rate of multiple ions in the k-th mode is given by,

$$\dot{\bar{n}}^{(k)} = \frac{e^2}{4m\hbar\omega_k} S_E^{(k)}(\omega_k), \tag{6.13}$$

where

$$S_E^{(k)}(\omega) = 2\sum_{i,j}\int_{-\infty}^{\infty} d\tau \, \langle \delta E_i^{(k)}(\tau)\delta E_j^{(k)}(0)\rangle \, e^{-i\omega\tau}, \tag{6.14}$$

is the spectral density for multiple ions interacting with electric-field noise, where the summation is over all pairwise permutations of ions i and j, and we define $\delta E_i^{(k)}(t) = \delta\mathbf{E}(t, \mathbf{r}_i)\cdot\mathbf{c}_i^{(k)}$ to be the projection of the electric-field noise onto the k-th mode at the i-th ion. $\mathbf{c}_i^{(k)}$ is the normalized mode function that satisfies

$$\sum_{i=1}^{N} \mathbf{c}_i^{(k)}\cdot\mathbf{c}_i^{(k')} = \delta_{k,k'}. \tag{6.15}$$

for N ions. In the case of two ions, we have

$$\mathbf{c}_1^{(com)} = \mathbf{c}_2^{(com)} = \frac{\hat{e}_i}{\sqrt{2}}, \text{ and } -\mathbf{c}_1^{(str)} = \mathbf{c}_2^{(str)} = \frac{\hat{e}_i}{\sqrt{2}} \tag{6.16}$$

where $\hat{e}_i$ is the unit vector in the $i \in (x, y, z)$ direction. Assuming spatially correlated electric-field noise at ion 1 and ion 2, i.e. $\delta\mathbf{E}(t, \mathbf{r}_1) = \delta\mathbf{E}(t, \mathbf{r}_2)$ we can calculate the common

mode spectral density experienced by the two-ion system,

$$\begin{aligned} S_E^{(com)}(\omega_{com}) &= 2\int_{-\infty}^{\infty} d\tau \left[\frac{\langle \delta E_1(\tau)\delta E_1(0)\rangle}{2} + \frac{\langle \delta E_2(\tau)\delta E_2(0)\rangle}{2} + \langle \delta E_1(\tau)\delta E_2(0)\rangle\right] e^{-i\omega_{com}\tau} \\ &= 2S_E(\omega_{com}), \end{aligned} \tag{6.17}$$

where $S_E(\omega_{com})$ is the single ion spectral density. And we can calculate the stretch mode spectral density

$$\begin{aligned} S_E^{(str)}(\omega_{str}) &= 2\int_{-\infty}^{\infty} d\tau \left[-\frac{\langle \delta E_1(\tau)\delta E_1(0)\rangle}{2} - \frac{\langle \delta E_2(\tau)\delta E_2(0)\rangle}{2} + \langle \delta E_1(\tau)\delta E_2(0)\rangle\right] e^{-i\omega_{str}\tau} \\ &= 0. \end{aligned} \tag{6.18}$$

In the general case, it should be noted that the COM mode can be excited by a uniform electric field, $E(t)$. But the stretch mode is sensitive to differential motion, and thus is excited only by electric-field gradients, which we can estimate to be $E(t)/D$, where D is the characteristic distance from the trap electrodes to the ion [6]. So for a stochastic electric field, the COM mode heating rate scales roughly as the variance of the electric-field fluctuations, assuming zero-mean, $\dot{\bar{n}}^{(com)} \sim \langle E^2(t)\rangle$; and the stretch mode heating rate scales roughly as the variance of the corresponding field-gradient, $\dot{\bar{n}}^{(str)} \sim \langle [d_{ion-ion} \cdot E(t)/D]^2\rangle$ [95].

6.8.2 Simulated noise sources

Heating rates of two ions in the stretch mode may provide additional insight into the mechanisms behind electric-field noise on ion trap surfaces. Here, we lay the groundwork for future studies of stretch mode heating rates by calculating the expected noise as a function of ion-surface distance. The simulations iterate through three distinct noise models mentioned previously for modeling the single-ion heating rates: microscopic surface noise, macroscopic surface noise, and technical noise. For each case, we find the stretch mode heating rates to differ in d-dependency and noise amplitude as compared to single-ion heating rates.

Microscopic noise

As discussed in Section 6.1, there are a multitude of possible models for microscopic noise sources which include two-level fluctuators, adatom dipoles fluctuations, and microscopic patch potentials. In terms of distance scaling, all these microscopic noise sources contribute to the single-ion heating rate as d^{-4} [50].

For the two-ion case, the COM mode acts as a heavy single ion, and also exhibits d^{-4} behavior. The stretch mode, however, does not follow the same trend because it is sensitive to differential electric-field noise. This means that quadrupolar fluctuations, i.e. fluctuations in the curvature of the trapping potential, effect the heating of the stretch mode. To study

the distance scaling of the stretch mode heating, let us consider microscopic surface dipole fluctuations. Following the analysis in [64], we find that the autocorrelation of the electric-field is

$$\langle E_z(t)E_z(0)\rangle = \frac{3\pi\sigma_d}{8(4\pi\epsilon_0)^2 d^4}\langle \mu(t)\mu(0)\rangle\,, \tag{6.19}$$

where $\mu(t)$ is the surface dipole and σ_d is the dipole surface density. We also find that the autocorrelation of the quadrupole field is

$$\langle Q_{zz}(t)Q_{zz}(0)\rangle = \frac{45\pi\sigma_d}{32(4\pi\epsilon_0)^2 d^6}\langle \mu(t)\mu(0)\rangle\,. \tag{6.20}$$

Thus, the spectral density of the quadruatic potential fluctuations is

$$S_{Q_{zz}} = \frac{15}{4d^2}S_{E_z}. \tag{6.21}$$

Converting this to a stretch mode heating rate [96], we find that

$$\dot{\bar{n}}^{(str)} = \frac{e^2(d_{ion-ion})^2}{4m\hbar\omega_s^2}S_{Q_{zz}}. \tag{6.22}$$

Combining Eq. (6.20), (6.21), and (6.22), we see that the stretch mode heating rate scales as $\dot{\bar{n}}^{(str)} \sim d^{-6}$ for microscopic surface noise sources.

Macroscopic patch potentials

In Section 6.5.2, we argued that microscopic noise was not the main mechanism behind our experimentally measured ion heating, since we observed a distance scaling of $\sim d^{-2.5}$ for the single-ion heating rate. In fact, we required a macroscopic noise model to describe our data. Specifically, we revisit the model of fixed macroscopic patch potentials from Section 6.5.2, taking the same fixed patch configuration and voltage noise amplitudes as in Fig. 6.9(a). The simulated results of the stretch mode heating is shown in Fig. 6.12. We find a rough distance scaling of d^{-4} in both the planar and normal polarizations in contrast to the single-ion heating rate d-scaling of $\sim d^{-2.6}$. Additionally, the stretch mode heating rate is smaller in magnitude than the single-ion case, which may allow for more precise measurements of the heating rates and consequently the distance scaling.

Technical noise

The two-ion stretch mode heating rates may also act as a probe for technical noise on the trap electrodes. Following a similar analysis as in Section 6.4, we simulate the stretch mode heating as a function of ion-surface distance under the assumption that the heating rate is dominated by 3 μV amplitude noise on individual trap electrodes. From the symmetry of our elevator trap, we need only consider the effects of electrodes 1, 3, and 9 in order to the

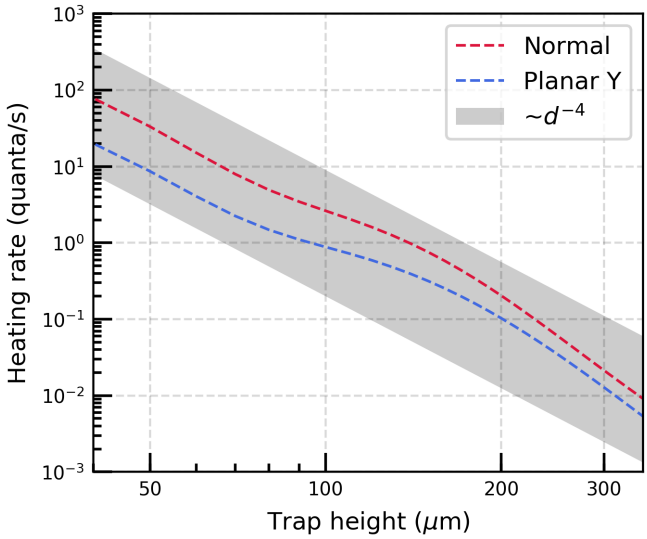

Figure 6.12: Simulation of two-ion stretch mode heating rates as a function of the ion-electrode distance, with COM frequency of $\omega_t = 2\pi \times 1$ MHz. These simulations describe noise with projection in both the normal (red) and planar y-axis (blue) axial stretch modes. The particular patch configuration and voltage noise amplitudes are taken from Fig. 6.9. The shaded region acts a guide for the eye to illustrate a d^{-4} dependence.

fully characterize the technical noise from all other DC electrodes. The simulation results are shown in Fig. 6.13.

In contrast to the single-ion technical noise d-scaling, we find that stretch mode noise in both the planar and normal directions evolve similarly with d. In particular, the 'dip' feature present in most of the normal-axis heating rates from Fig. 6.4 is eliminated since the stretch mode is largely agnostic to the absolute electric-field noise magnitude. Additionally, the stretch mode heating rate is maximum around a trap height of order 100 µm, and decreases as the ion heights approach both the low and high extremes. This trend suggests that two-ion stretch mode operations in our elevator trap may be less sensitive to technical noise at low and high ion heights.

Furthermore, we note that the stretch mode heating between 50 µm and 100 µm scales linearly with d from technical noise on electrode 3 and remains roughly constant from technical noise on electrodes 1 and 9. This leveling off of the stretch mode heating below 100 µm significantly differs from the predicted distance scalings of d^{-6} for microscopic noise and d^{-4} for macroscopic noise models. This disparity implies that measurement of the stretch mode heating rates below 100 µm along a single polarization may be a sufficient check for the presence of technical noise.

In terms of the local distance scaling in this regime, we expect to measure a distance scaling exponent of $\beta \approx 0$ in the presence of technical noise as compared to $\beta \approx 4(6)$ if the noise is dominated by macroscopic (microscopic) surface noise. Such a large signal

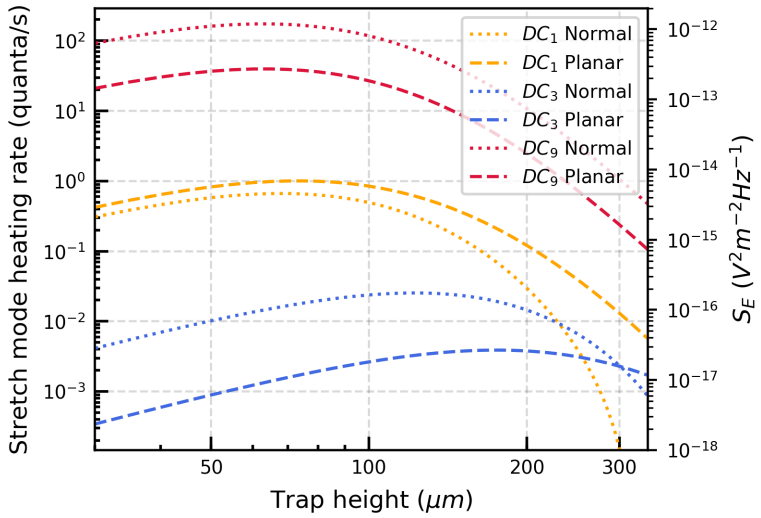

Figure 6.13: Two-ion stretch mode heating rates as a function of the trap height, with COM frequency of $\omega_t = 2\pi \times 1$ MHz. The simulations are evaluated with 3 µV amplitude noise on DC electrodes 1 (orange), 3 (blue), and 9 (red). Planar stretch mode contributions are shown with dashed lines while normal stretch mode contributions are shown with dotted lines

can be clearly observed by measurement on a single stretch mode, especially with small errors associated with low stretch mode heating rates. This may be useful when physical or practical limitations prevent measurement of multiple motional modes. The two-ion stretch mode technical noise signal is more prominent than the single-ion case, where any one mode may exhibit a technical noise distance scaling in the range $-2 \lesssim \beta \lesssim 1$ between trapping heights 50 µm and 100 µm. This large variation of β for single-ion heating rates makes it difficult to distinguish technical noise from other potential noise sources such as macroscopic or microscopic surface noise, which lead to β values between -1 and -4. Thus, in order to validate the presence or absence of technical noise with a single ion, we must turn to measurement of additional motional polarizations.

Chapter 7

Wire-mediated long-range ion-ion coupling

In the context of quantum information processing, individual trapped ions make ideal qubits with long coherence times and high-fidelity state initialization, manipulation, and readout. Multi-qubit gates are mediated by quantized motional states shared among the trapped ion qubits, and this collective motion of trapped ions is generated by ion-ion and ion-field Coulomb interactions. As we discussed in Chapter 2, ion trap systems typically consist of linear chains of crystallized ions, where the ion-ion separation within these chains is ~ 5 µm. At this separation distance, the Coulomb coupling between the ions is strong, leading to fast multi-qubit gates. With the linear ion string design, several groups have demonstrated high-fidelity gate operations [2, 3, 4] and employed fully-controllable small quantum computers up to 11 ions [97, 22]. Currently the challenge remains to scale up trapped ion systems to more qubits and more ion-ion interactions, which will ultimately allow for nontrivial gate operations and implementation of quantum supreme algorithms. As we scale to greater number of qubits, the physical distance between ions becomes large, making a necessity for efficient long-range ion-ion communication.

The trapped ion community has investigated several methods of long-range interactions between ions. One viable strategy is to control small ion chains and physically shuttle these small chains into various zones for operation [44, 42, 26, 98]. Another scheme is to transfer quantum information via optical fibers and establish non-deterministic photonic links between ions [99, 100, 101, 102, 103, 104].

In this thesis, we present a novel ion-ion coupling mechanism for long-range interaction: motional dipole-dipole coupling of two ions in separate traps enhanced via an electrically floating metallic wire. Here, two ions are held in separate trapping zones, and their motions induce oscillating charges in a shared wire, which acts as an intermediate bus to communicate between the ions. A cartoon schematic of this system is illustrated in Fig. 7.1.

Coulomb-mediated coupling of atomic ions in separate potential wells has been demonstrated for ion separations of ~ 50 µm [105, 106]. However, this direct coupling is limited to close-range interactions, as the Coulomb interaction strength, Ω_{ex}, falls off as $1/r^3$, r

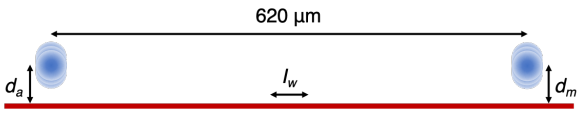

Figure 7.1: Schematic of the ion-wire-ion system, with ions separated by 620 µm. The vertical motion of each ion induces image currents in the wire and vice-versa.

being the ion-ion separation. With direct Coulomb coupling between two ions separated by $r = 620$ µm, we expect ~ 600 ms exchange rate between the motional states of the ions. In comparison, our wire-mediated coupling achieves an order of magnitude improvement in the energy exchange rate.

The main motivation behind this project is the demonstration of ion-ion entanglement via a classical wire. This achievement would have immediate implications for the development of trapped ion quantum systems, suggesting that a noisy quantum bus does not preclude the transfer of quantum information.

Furthermore, this wire-mediated coupling also allows for sympathetic cooling between ions in different zones. This technique allows for cooling of qubit ions without affecting their internal quantum states. Such functionality may be necessary to quench the anomalous heating of ion motion or remove excess energy from shuttling, separation, and recombination operations. This may also open a path for cooling and trapping ion species that cannot be laser cooled, allowing precision measurements of such particles.

Though the concept of sympathetic cooling is well established, experiments as of present have only been able to sympathetically cool co-trapped ions [107, 108, 109, 110, 111, 112]. Because these ions have to be in the same trapping potential, this limits the types of particles that may be probed. For example, ions with widely different masses cannot be co-trapped, and therefore could not be sympathetically cooled. Our scheme consists of separate trapping zones with independent field control, thus allowing simultaneous trapping of such different ions and wire-mediated interactions between them. This architecture may also lead to trapping of single electrons and protons as well as their antiparticles [113].

7.1 Coupling Mechanism

The central feature in our experiment is the wire-mediated interaction between ions, which is characterized by the electrostatic ion-wire coupling strength, $\kappa \equiv g/(2m\omega)$. In this section, we describe ion motions in the presence of κ and develop a classical method for the calculation of the ion-wire coupling strength.

7.1.1 Classical dynamics

We begin with an abstract picture of the two-ion interaction, agnostic to the coupling mechanism or physical architecture that is implemented. We may model the system as a pair of

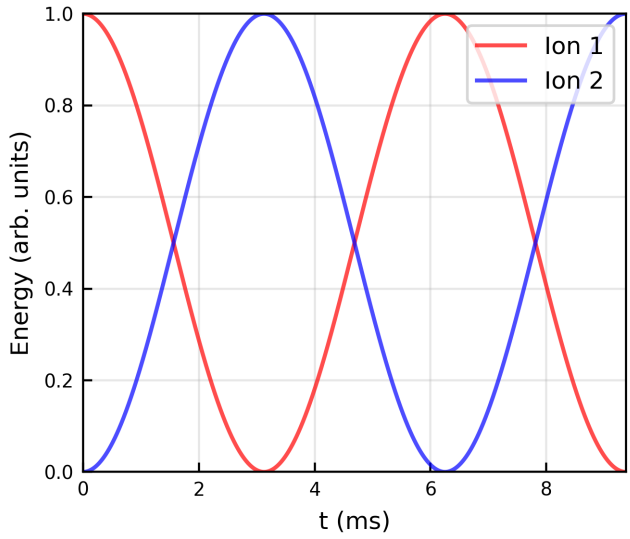

Figure 7.2: Analytic classical energy evolution of two resonant trapped ions coupled with coupling strength $\kappa = g/(2m\omega) = 2\pi \times 80$ Hz. In this idealized case, full exchange of the energies occurs at $t = 3.2$ ms.

coupled harmonic oscillators, with the classical Hamiltonian for such a system given by

$$\hat{\mathcal{H}} = \sum_{i=1}^{2} \frac{1}{2} m_i v_i^2 + \sum_{i=1}^{2} \frac{1}{2} m_i \omega_i^2 x_i^2 + g x_1 x_2, \tag{7.1}$$

where m_i, ω_i, v_i, x_i are the mass, frequency, velocity, and position of ion i, respectively. Again, the g parameter represents the coupling strength between ion 1 and ion 2, and its physical origin is detailed in Section 7.1.2. For pedagogy, let us consider the dynamics of identical ions in the resonant case such that $m_1 = m_2 = m$ and $\omega_1 = \omega_2 = \omega$. Then solving for each ion's equation of motion gives

$$x_1(t) = A_1 \cos(\nu_+ t) + B_1 \sin(\nu_+ t) + A_2 \cos(\nu_- t) + B_2 \sin(\nu_- t), \tag{7.2}$$

$$x_2(t) = A_1 \cos(\nu_+ t) + B_1 \sin(\nu_+ t) - A_2 \cos(\nu_- t) - B_2 \sin(\nu_- t), \tag{7.3}$$

where $\nu_\pm^2 = \omega^2 \pm g/m$ are the eigen-frequencies of the normal modes. Now inserting initial conditions of $x_1(0) = A$ and $x_2(0) = \dot{x}_1(0) = \dot{x}_2(0) = 0$, we can simplify the above equations to

$$x_1(t) = \frac{A}{2}[\cos(\nu_+ t) + \cos(\nu_- t)] = A \cos\left(\frac{\nu_+ - \nu_-}{2} t\right) \cos\left(\frac{\nu_+ + \nu_-}{2} t\right), \tag{7.4}$$

$$x_2(t) = \frac{A}{2}[\cos(\nu_+ t) - \cos(\nu_- t)] = -A \sin\left(\frac{\nu_+ - \nu_-}{2} t\right) \sin\left(\frac{\nu_+ + \nu_-}{2} t\right). \tag{7.5}$$

The experiments in this thesis are operated in the weak coupling limit, $g/m \ll \omega$, where we have

$$\nu_{\pm} \approx \omega \pm \frac{g}{2m\omega}, \tag{7.6}$$

meaning the system has a beat frequency of $\omega_{beat} = \nu_+ - \nu_- = g(m\omega)^{-1}$ and a beat oscillation period of $t_{beat} = 2\pi m\omega/g$. Thus, we expect to see a full transfer of the energy at an exchange time of

$$t_{\text{ex}} = \frac{\pi m\omega}{g}. \tag{7.7}$$

An illustration of this resonant interaction using the results from Eq. 7.4 and Eq. 7.5 is shown in Fig. 7.2, where we have set $\omega = 2\pi \times 400$ kHz, and $g/(2m\omega) = 2\pi \times 80$ Hz.

7.1.2 Equivalent circuit model

To further study the coupled ion dynamics and calculate g, we map our ion-wire-ion system to a lumped element circuit. Because the ion is harmonically trapped, the harmonic motion induces flow of image charges in the wire, creating image currents. As such, we may perform analysis on an electrically equivalent model of the ion motions and the image currents following the formulation by D.J. Wineland, H.G. Dehmelt, and D.J. Heinzen [114, 115].

Ion-wire interaction

We start with the assumption that the ion-wire interaction can be modeled by a trapped ion held between two conducting parallel plates, as shown in Fig. 7.3(left). Assuming that the plate dimensions are much larger than the separation, we neglect edge effects and find that the current induced by a harmonically trapped ion is

$$I = \frac{e\dot{z}}{D_{\text{eff}}}, \tag{7.8}$$

where $D_{\text{eff}} \equiv U_w/E_z^w$ is the effective distance of a trapped ion to the wire and determined by ratio of the voltage on the wire, U_w, to the generated electric-field at the trapped ion position, E_z^w. D_{eff} may be approximated by the physical ion-wire distance, but its exact value depends on the geometry of the wire. In this picture, the equation of motion for a trapped ion is given by

$$m\ddot{z} = -m\omega_z^2 z + F_w \tag{7.9}$$

where F_w is the force exerted by the wire onto the ion,

$$F_w = \frac{eV}{D_{\text{eff}}} + F_{\text{ind}}. \tag{7.10}$$

F_{ind} is an additional back-action force on the ion from the induced charges in the wire, but for a single ion, this term is small and may be neglected [114]. Combining Eq. (7.8), Eq. (7.9),

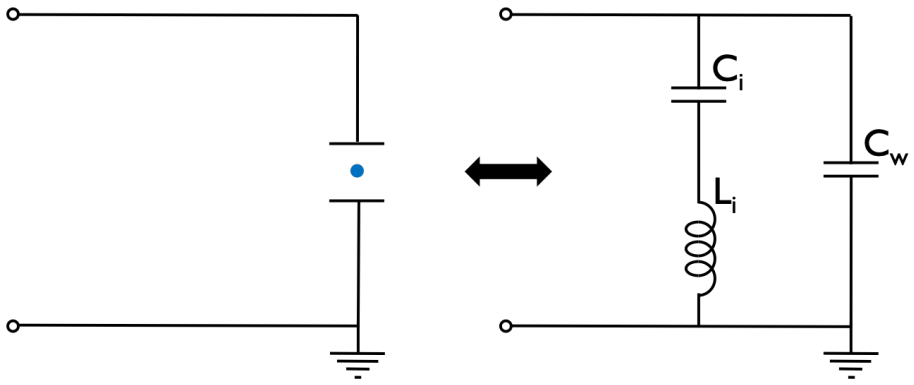

Figure 7.3: (Left) Electromechanical circuit diagram of ion between plates of a parallel-plate capacitor which is grounded on one end and floating on the other. (Right) Electrically equivalent circuit model of a single harmonically trapped ion, represented with a series L_iC_i circuit coupled to (i.e. parallel with) a floating wire with capacitance C_w to ground.

and Eq. (7.10), we arrive at

$$V = L_i \frac{dI}{dt} + \frac{1}{C_i} \int I dt. \tag{7.11}$$

Here, we have translated the ion and its image current into a series LC system that shunts the electrode capacitor, with an equivalent ion inductance and capacitance of

$$L_i = \frac{m D_{\text{eff}}^2}{e^2} \ , \ C_i = \frac{1}{\omega_z^2 L_i}. \tag{7.12}$$

For typical trapped ion parameters, we find that the equivalent inductance is rather large, $L_i \approx 5 \times 10^4$ H, while the equivalent capacitance is rather small, $C_i \approx 2 \times 10^{-18}$ F. These equivalences allow us to relate the dynamics of the circuit in Fig. 7.3(right) with the dynamics of the circuit in Fig. 7.3(left).

Ion-wire-ion coupling

Equipped with the understanding that a single harmonically trapped ion can be modeled as a series LC circuit, we can now tackle the case of two ions coupled via a shared electrode wire. In this case, we now have two resonant systems that are electrically connected, see Fig 7.4(left), and the equivalent circuit which models the system is shown in Fig. 7.4(right).

C_w is the capacitance of the wire to ground, which we calculate both analytically and numerically with finite-element simulations. We have also added the resistance, R, of the wire to model a more physically realistic system.

The classical solution to the dynamics of this circuit in the resonant case with identical ions may be expressed in terms of the circuit parameters as [57]

$$t_{\text{ex}} = \frac{C_w}{\omega_z C_i} = \frac{m\omega_z}{e^2} C_w D_{\text{eff}}^2. \tag{7.13}$$

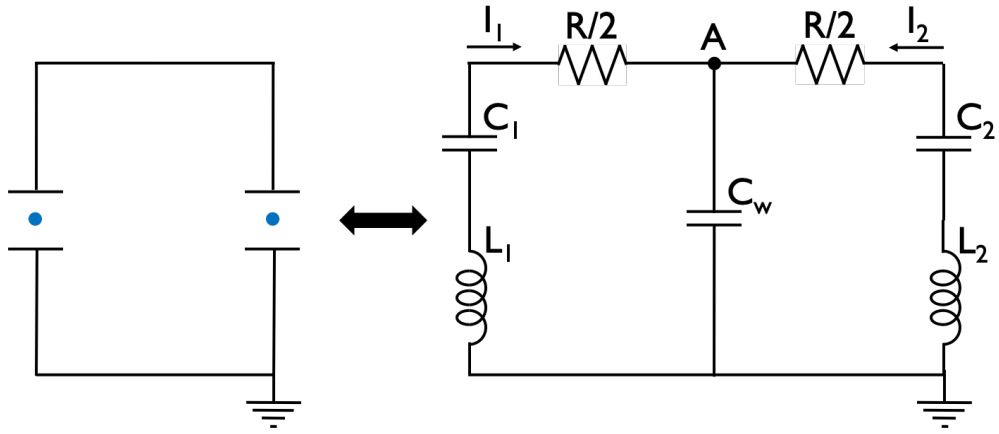

Figure 7.4: (Left) Schematic of two ions between parallel-plate capacitors; they are connected via a floating wire and a common ground. (Right) Equivalent circuit of two harmonically bound ions coupled to each other through a shared wire with resistance R and capacitance C_w to ground. Each ion is represented with inductance L_i and capacitance C_i. The current I_i in each branch corresponds to the velocity its respective ion.

Analogously, we may define the coupling strength, κ, as

$$\kappa = \frac{g}{2m\omega_z} = \frac{\pi}{2}\frac{1}{\sqrt{L_i C_w}} = \frac{\pi}{2}\frac{e^2}{m\omega_z}\frac{1}{C_w D_{\text{eff}}^2}. \tag{7.14}$$

In this form, we immediately see various parameters that affect the exchange time, t_{ex}, which we desire to minimize for optimal performance. Heuristically, there are two categories of parameters in Eq. 7.13: operational parameters, which may be adjusted *in-situ*, and design parameters, which are derived from the geometry of the wire and trap.

The operational parameters include the ion charge e and mass m as well as the trap frequency ω_z. In terms of these parameters, we find that low mass and highly charged ions with low trap frequency ω_z lead to an increase in the exchange rate. Intuitively, we are increasing the electric dipole of each ion, and thus increasing the coupling strength. Additionally, increasing the number of ions leads to faster exchange times, though the improvement is only linear due to the e^2/m dependence.

The design parameters consist of the wire capacitance to ground C_w and the effective ion-wire distance D_{eff}. Eq. 7.13 suggests we must engineer the wire to have minimum capacitance to ground, C_w, in order to maintain the image currents in the wire. This logic also shows why the coupling wire must be electrically floating and not directly connected to ground. As we detail in Section 7.2.1, the wire geometry, vis-à-vis the electric fields, may be designed to maximize the ion-wire coupling at specific physical ion heights. Though in general, D_{eff} increases as the ion gets closer to the wire.

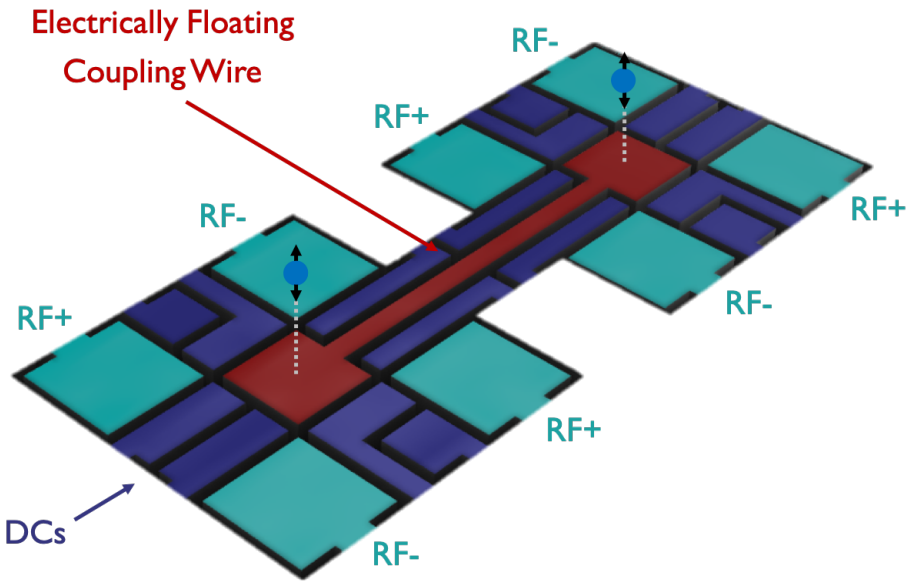

Figure 7.5: Isometric view of the double trap. Ions are held above two distinct trapping regions with mirrored electrode layout. In each trapping region, there are 8 DC electrodes colored blue and 4 RF electrodes (operated in the out-of-phase configuration) colored green. The two regions are connected with an electrically floating center electrode wire, colored red.

7.2 Double trap

Up to this point, we have discussed the ion-wire-ion coupling dynamics while remaining agnostic to the physical implementation. In this section, we turn our attention towards the physical design of the ion-wire-ion system, detailing the optimally engineered aspects as well as challenges faced.

Figure 7.5 shows an isometric rendering of our two surface traps separated by 620 µm. We jointly term these two traps as the 'double trap', consisting of the so-called *top* and *bottom* traps. Both the *top* double trap and *bottom* double trap comprise of 8 DC electrodes, colored blue in Fig. 7.5, and 4 RF electrodes, shown in green. The distinguishing feature of our double trap is a central electrically floating wire which connects the centers of the *top* and *bottom* traps and acts as the coupling wire between ions in the separate traps. This center wire electrode, colored red in Fig. 7.5, is the only electrode on the trap with no connection to external control voltages.

Similar to the elevator trap discussed in Chapter 4 and detailed in ref. [30], the double trap is operated with out-of-phase RF drives. Thus, the planar confinement in each trapping region is controlled by the RF pseudo-potential while the vertical trapping potential at each site is fully controlled by DC fields. This feature provides greater trap frequency stability in the vertical axis. The stability in this direction is particularly important as our trap is engineered to maximize coupling of the vertical ion motion to the wire.

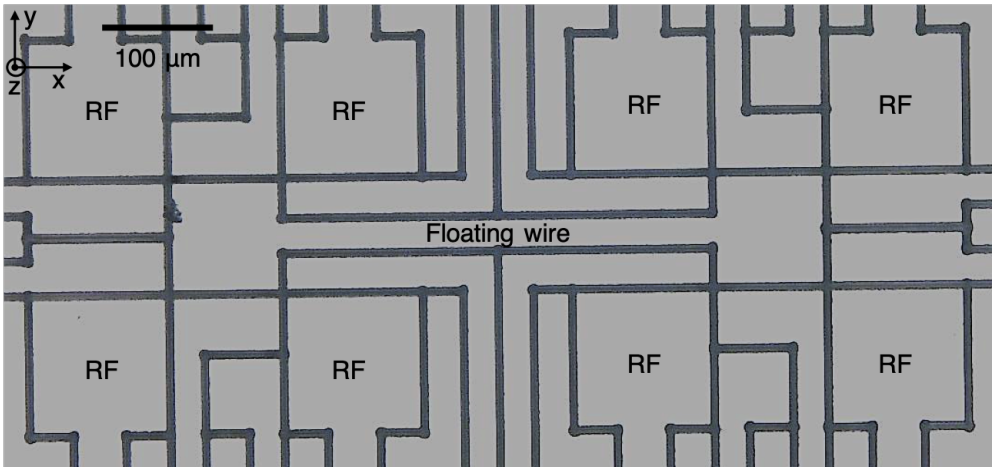

Figure 7.6: Microscope image of the double trap.

7.2.1 Design parameters

Figure 7.6 shows a microscope image of the double trap, providing a more accurate representation of the dimensions. Our trap is coated with 1-µm-thick aluminum-copper using the process discussed in Section 5.1.2. The RF electrode pads have dimensions of 145 µm × 145 µm with 30-µm-wide leads. The DC electrodes in each trap are arranged in a mirrored geometry across the midpoint of the double trap. The two traps are separated by 620 µm, measured from the center of each trapping region, and share an electrically floating central wire. This coupling wire consists of two square paddles connected together by a narrow strip. The paddle geometry, with dimensions 120 µm × 120 µm, optimizes the ion-wire coupling strength at a trapping height of 50 µm by maximizing the vertical electric-field from the coupling electrode. The strip connecting the paddles is kept at a narrow 30 µm width to minimize the total capacitance of the wire to ground.

Each trapping site holds a single $^{40}Ca^{+}$ ion, where pseudo-potential confinement in the planar directions is generated with an out-of-phase RF drive at 36 MHz and $\sim$ 100 V_{pp}, giving planar trap frequencies of $\omega_{x,y} \approx 3$ MHz. In the vertical axes, the motional trap frequencies are tunable up to $\omega_z = 2\pi \times 2.5$ MHz, limited by the ± 10 V range on each DC electrode. This allows simple control of the interaction by tuning the ion vertical trap frequencies in and out of resonance.

Coupling strength optimization

From Eq. 7.14, we saw that the coupling strength, measured in Hz, is characterized by $\kappa = g/(2m\omega_z)$. Here, we discuss the design aspects of our trapped ion system which maximize the coupling strength, κ, to achieve strong ion-wire-ion interactions. Though various wire geometries may be investigated, we focus on the minimalist design of two square paddles connected by a narrow strip in order to maintain manageable simulation and fabrication.

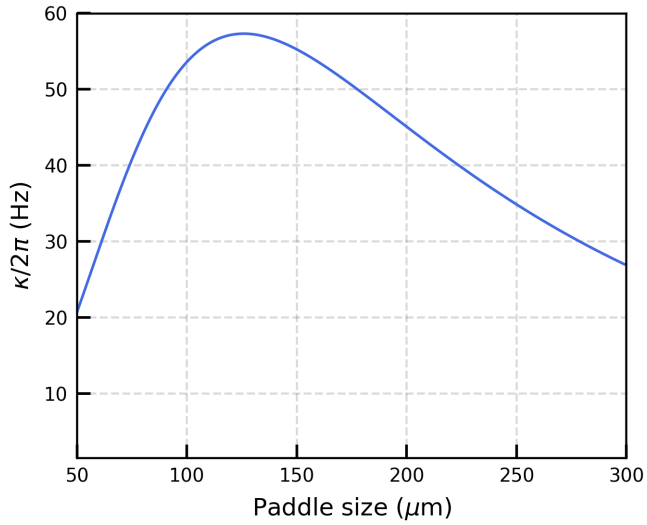

Figure 7.7: Ion-wire coupling strength, $\kappa/(2\pi)$, as a function of paddle size for a fixed ion height of 50 µm and 500 kHz trap frequency. The coupling strength $\kappa/(2\pi)$ is maximized around $2\pi \times 57$ Hz with a paddles size of 120 µm $\times$ 120 µm

First, we wish to minimize the effective ion-wire distance D_{eff} by adjusting the paddle size. Because $D_{\text{eff}} \equiv U_w/E_z^w$, the paddles must be designed to maximize the electric-field (at particular ion positions in each trap) generated by a voltage on the coupling electrode, thus also maximizing the interaction between the ion and the wire. We choose to optimize the electric-field at an ion height of 50 µm in both traps as a balance between poor coupling strength at high heights and large electric-field noise and trap instabilities at low heights.

Figure 7.7 shows the ion-wire coupling strength as a function of the edge-length of the square paddle for a fixed ion height of 50 µm. This specific calculation is evaluated at $\omega_z = 2\pi \times 1$ MHz trap frequency using the gapless plane approximation [45] mentioned in Section 4.1 and Section 6.4.1. From this, we find that the coupling strength at 50 µm is maximized for a square paddle of size 120 µm $\times$ 120 µm. With this chosen paddle size, an ion located 50 µm above the wire has an effective distance of $D_{\text{eff}} \approx 133$ µm and a coupling strength of $\kappa \approx 2\pi \times 57$ Hz.

For this set geometry, We may additionally investigate the coupling strength for various ion heights. The simulated results for this are shown in Fig. 7.8. We find that the coupling strength, κ, roughly follows a d^{-3} scaling, originating from the D_{eff}^2 dependence of our wire's finite geometry.

The other design parameter of concern is the total capacitance of the wire to ground, C_w, which should be minimized in order to maximize κ. With the paddles sizes fixed, the remaining free parameters are the length and width of the strip connecting the paddles. The length is set to 500 µm in order to separate the ions enough such that the electric field from electrodes in the *bottom* trap will have negligible effect on an ion in the *top* trap and vice-versa. The strip width is set to a narrow 30 µm to minimize C_w while still maintaining

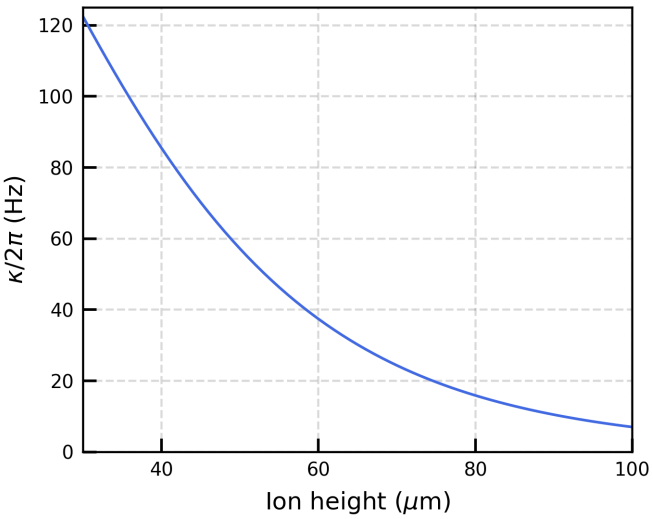

Figure 7.8: Ion-wire coupling strength, $\kappa/(2\pi)$, as a function of physical ion height, measured from the center of a 120 µm × 120 µm paddle. The coupling strength $\kappa/(2\pi)$ is calculated at a trap frequency of 500 kHz and roughly follows a d^{-3} scaling.

sufficient current flow from one end of the wire to the other. With these parameters, we calculate a capacitance of $C_w = 30$ fF using a finite-element solver.

Decoherence sources

In order to observe the coupling signal, the decoherence caused by noise inherent in the wire as well as instability of the ion motions must occur on a slower time-scale than the coupling. This is especially important in the quantum regime, where coherent coupling of the quantized ion motions vanishes in the presence of noise. We review the effect of several noise sources following the analysis in ref. [57] and show that the noise in our double trap wire design may be sufficiently suppressed to allow coherent coupling, even with a normal conducting material.

One source of decoherence is leakage of the induced current in the wire to ground. We may model this in the equivalent circuit, Fig. 7.4, with a large resistor, $R_g > 10^{13}$ Ω, in parallel to the capacitor C_w between node A and ground [57]. In this simple picture, the decay constant for the current is $4R_gC > 1.2$ s, much larger than the predicted coupling exchange time, $t_{\text{ex}} \sim \mathcal{O}(1)$ ms.

Decoherence also originates from current dissipation in the wire due to its finite resistance, which we estimate to be 0.1 Ω. From Eq. 7.8, the induced current in the wire may be calculated to be $I = e\dot{z}/D_{\text{eff}} \approx e\sqrt{\hbar\omega_z/m}/D_{\text{eff}} \approx 0.1$ fA at a trap frequency of $\omega_z = 2\pi \times 1$ MHz and optimized $D_{\text{eff}} \approx 133$ um. Thus, we expect it takes 6.6×10^5 s to dissipate one motional quanta due to the wire resistance, a negligible effect compared to $t_{\text{ex}} \sim \mathcal{O}(1)$ ms.

Another byproduct of the finite wire resistance is Johnson noise, which contributes to

the motional decoherence of ions trapped above the wire. The Johnson noise power is given by

$$P = k_B T \Delta f, \tag{7.15}$$

where $k_B T$ is the thermal energy of the wire and Δf is the bandwidth over which the ion is sensitive to noise. The heating rate generated by Johnson noise in terms of motional quanta is

$$\dot{\bar{n}}_J = \frac{P}{h f_z} = \frac{k_B T \Delta f}{h f_z} = \frac{k_B T}{h Q}. \tag{7.16}$$

In our equivalent circuit model, Fig. 7.4, the Q-factor is given by

$$Q = \frac{1}{R}\sqrt{\frac{L_i}{C_i}}. \tag{7.17}$$

With the values we have used up to now, the expected heating from Johnson noise is $\dot{\bar{n}}_J = 0.09$ quanta/ms at room temperature. This heating contribution may be significantly improved by operating the trap system at cryogenic liquid helium temperatures. Assuming a resistivity ratio of $\rho_{300K}/\rho_{4K} \approx 50$ for the wire [57], the Johnson noise heating rate is reduced to $\dot{\bar{n}}_J^{4K} = 0.02$ quanta/s at 4 K. Thus, at cryogenic temperatures, the Johnson noise is not expected to affect the coherent coupling.

Finally, we mention a decoherence source not unique to our double trap geometry: excess electric-field noise in trapped ion systems (often termed as anomalous heating), which causes heating and decoherence of the ion motion as discussed in Chapter 6. According to our room temperature measurements in Section 6.2.4, we expect such noise to contribute a heating rate of order 1 quanta/ms at 50 µm ion-surface distance. This magnitude of noise would be detrimental to the coherent coupling with $t_{\text{ex}} \sim \mathcal{O}(1)$ ms. Fortunately, reduction of this noise by two orders of magnitude may be realized with in-situ Ar^+ bombardment [116, 117] or operation at cryogenic temperatures [75, 118, 119, 43, 120, 49], bringing the excess electric-field noise heating effect to a negligible $\dot{\bar{n}}_{ex} = \mathcal{O}(10)$ quanta/s.

For both techniques to reduce motional heating, either cooling or Ar^+ bombardment, there is concern that the electrically floating coupling wire may accumulate a large amount of charge, generating a large electric field that may degrade the trapped ion confinement. This problem is addressed in the following Section 7.2.2, where we demonstrate controlled photoelectric charging and discharging of the floating wire in order to neutralize extraneous charge.

7.2.2 Floating wire

The lynch pin of the double trap is the floating electrode wire that connects the two trapping zones. We have seen that its design is optimized to allow fast inter-zone ion-ion coupling of vertical motional modes with minimal decoherence. However, the innate electrical properties of the floating wire (explicitly charge build-up) create challenges for experimental measurement and control.

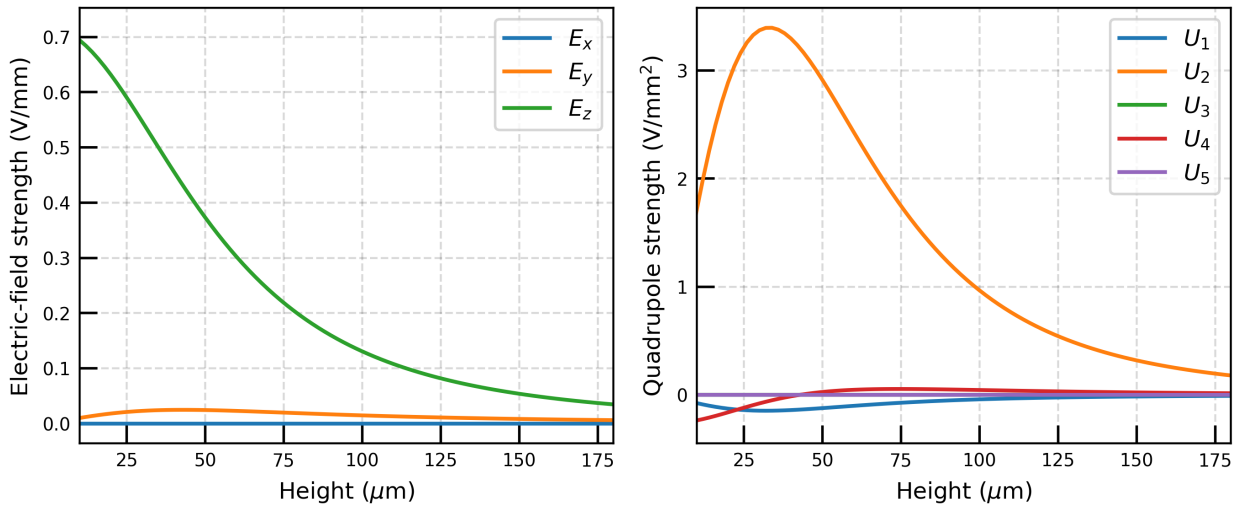

Figure 7.9: (Left) Simulated electric-field strength originating from the center floating wire held at 50 mV. The main contribution is in the E_z direction. (Right) Simulated quadrupole strengths from the charged center electrode. The main contribution is in the U_2 quadrupole

Charge effect and measurement

To begin, we must understand the effect of charge accumulation on our trapped ion system. As the floating wire builds charge, it distorts the confinement fields generated by the controlled DC and RF electrodes. By symmetry of the paddles and the central ion position, we expect this effect to be largely in the vertical axis of each trapping zone. To verify this intuition, we simulate the floating wire's contribution to all experimental multipoles as the ion height is scanned with respect to the trap surface. The results, calculated for a floating wire held at a static voltage of 50 mV, are shown in Fig. 7.9. As expected, there are mainly two multipoles, E_z and U_2 (both oriented along the vertical axis), affected by the excess charge, and there is little effect seen on the other multipoles.

We explicitly note that if the center electrode is held at -50 mV, we see the inverse effect on each multipole. This sign becomes important when working with the U_2 multipole, which controls the vertical trap confinement. If the center electrode is positively charged, the vertical trap frequency is increased. On the other hand, if the center electrode is negatively charged, a large anti-confinement potential is induced in the vertical direction. In the extreme case of large negative charge build-up on the floating wire, the vertical anti-confinement from the center electrode exceeds the maximum achievable U_2 confinement from the controllable DC electrodes, and so we are unable to trap ions in the system.

The benefit attached to this relation of the U_2 multipole to the floating wire charge is the capability to measure the charge by measuring a shift in U_2, i.e. a shift in the vertical trap frequency. In our current experimental setup, we have demonstrated the ability to measure trap frequencies with $2\pi \times 100$ Hz standard error using 729 nm spectroscopy. Accordingly,

the U_2 quadrupole may be controlled with 0.001 V/mm^2 accuracy, which corresponds to a controllable vertical trap frequency resolution of $\approx 2\pi \times 100$ Hz around $\omega_z = 2\pi \times 1$ MHz trap frequency. From Fig. 7.9, we find that the ion sensitivity, $\partial U_2/\partial U_w$, at 50 µm height is approximately 0.06 V/mm^2 per 1 mV on the floating wire. Coupled with our trap frequency resolution, this implies that we are sensitive to changes in the floating wire voltage of $\Delta V_w \approx 17$ µV. Under the assumption of $C_w = 30$ fF, this corresponds to a charge sensitivity of $\sim 3e$. Thus, we may utilize the vertical trap frequency as an extremely sensitive tool to probe the charge of the floating wire.

Controlling the charge

In addition to charge measurement, the ability to control the floating wire charge is essential for proper operation of the double trap.

One such control method is to install a movable in-vacuum mechanical arm which can make contact with the electrodes on the double trap. With the metallic arm grounded properly, this may provide an avenue to discharge any residual charge build-up on the floating wire, allowing for a 'reset' of the voltage. Unfortunately, this iteration of our vacuum system does not include such a mechanism, forcing a search for alternative *in-situ* non-contact methods of controlling the charge.

Ultimately, we found such a method by taking advantage of the photoelectric effect. Typically, the photoelectric effect is considered to be harmful for ion traps [54, 56], but if used correctly, it may be beneficial to operating our double trap. Conceptually, we shine high-energy photons onto the trap surface and excite movement of electrons across trap electrode boundaries. By exposing laser light onto the floating wire, we expect that electrons flow off of the floating wire. Conversely, exposing other nearby electrodes to the same light is expected to induce flow of electrons onto the floating wire.

Controlling the charge - Results

To measure the magnitude of the photoelectric effect on the center floating wire, we take advantage of the ion's sensitivity to electric fields. As we have seen from Fig. 7.9, charge build-up alters the electric dipole and quadrupole fields at the ion position. Consequently, by using the ion to measure shifts in both E_z and U_2 as a function of laser flux onto the trap surface, we can infer the magnitude of charge on the floating wire.

The experimental setup for this measurement consists of sending blue (422 nm) and near-UV (375 nm) light onto the double trap surface. The location of light is chosen to be either centered on the paddle of the *top* trap (exposing the floating wire directly to laser light) or 200 µm offset from the center, such that the laser does not contact the floating wire. Both the 422 nm and 375 nm beams are measured to have power of 100 µW prior to entering the vacuum chamber, and both beams form an angle of $\sim 10^\circ$ with respect to the trap surface.

The results are shown in Fig. 7.10, where the left (right) plot shows the change in E_z (U_2) compensation required to maintain the original ion position (trap frequency). As the

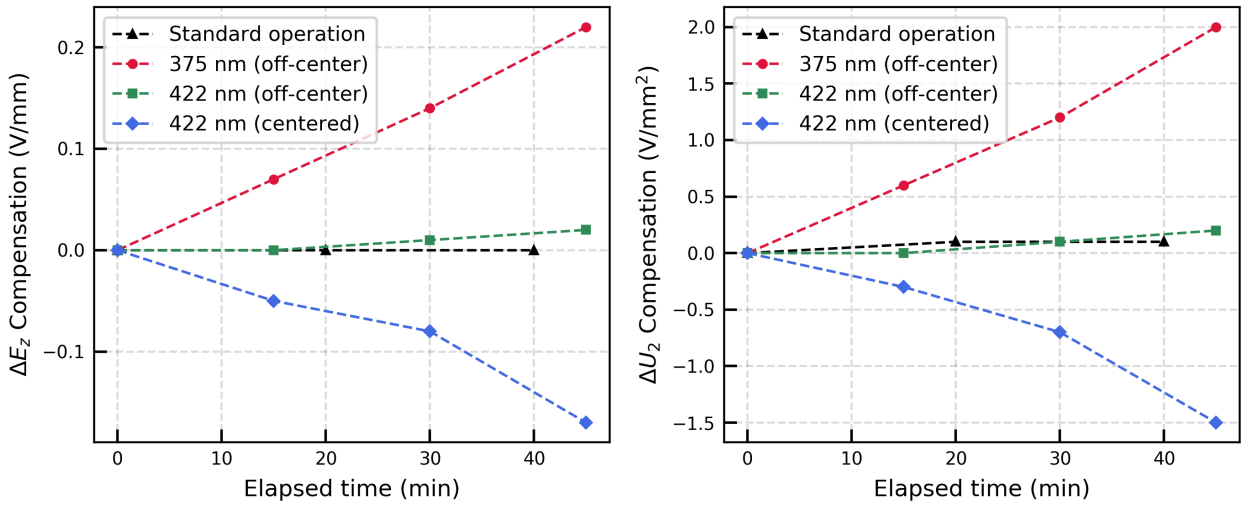

Figure 7.10: Demonstration of the photoelectric effect on the floating wire charge. Measurements are taken with 375 nm exposure, 422 nm exposure, and standard operation in the *top* trap (see text). 'Centered' beams are directed onto the *top* trap paddle center at $\sim 10^{\circ}$ from the surface while 'off-center' beams are displaced 200 µm from the center. (Left) E_z compensation required to maintain the original ion height as a function of exposure time. (Right) U_2 compensation required to maintain the original trap frequency as a function of exposure time.

cumulative intensity of the laser light on the trap surface increases, we see a gradual trend in the ΔE_z and ΔU_2 values, which implies net charging of the center floating wire. Note that positive ΔE_z and ΔU_2 values correspond to culmination of negative charge on the center electrode, and vice-versa.

Exposing the trap surface to 422 nm and 375 nm beams offset from the center floating wire (respectively shown in green and red in Fig. 7.10), such that the light does not shine onto it, causes electrons to flow from the grounded trap onto the floating wire, resulting in a pile-up of negative charge on the floating wire. This negative charge attracts our $^{40}Ca^{+}$ ion towards the trap, in the $-\hat{z}$ direction, and we must apply a positive ΔE_z to compensate for this positional shift, see Fig. 7.10(left). Additionally, negative charge on the floating wire leads to anti-confinement quadrupole fields in the axial $\hat{z}$ axis, as discussed above. In order to negate this effect, we must apply positive ΔU_2 to maintain the original trap frequency, as shown in Fig. 7.10(right).

By exposing the center floating wire directly to blue light (shown in blue in Fig. 7.10), we excite electrons which flow to the surrounding electrodes, implying an induced positive charge on the center electrode. In this case, our $^{40}Ca^{+}$ ion tends away from the trap surface in the $+\hat{z}$ direction, and we need to apply negative ΔE_z to re-center the ion position. Analogously, the geometry of the positively charged center electrode causes an increase in the axial, $\hat{z}$, confinement. So we must apply negative ΔU_2 to re-stabilize the trap frequency to its original

value. Notice that in Fig. 7.10, we do not show the effect of exposing the floating wire to 375 nm light. The reason being the photoelectric effect caused by 375 light is so strong that exposure onto the center floating wire results in a rapid shift of the ion position. We estimate the effect to cause a shift of $\Delta E_z \gtrsim -1$ V/mm per minute, leading to rather immediate ion loss.

A comparison of Fig. 7.10(left) and Fig. 7.10(right) indicates strong agreement of our measurements with the theory from Fig. 7.9. For an ion-surface distance of 100 µm, we expect a scaling between ΔE_z and ΔU_2 to take the form of $\Delta E_z = \alpha \Delta U_2$. According to the simulations from Fig. 7.9, we extract a theorized $\alpha = 0.1$ mm. This is in agreement with the measured scaling of $\alpha \sim 0.11$ mm from Fig. 7.10.

Under standard operation of the ion trap (shown in black in Fig. 7.10), the center electrode is exposed to 397 nm scatter, continuous and direct 866 nm light on the order of ~ 10 µW, and periodic direct 729 nm light with power ~ 1 mW. We do not observed any shift in the ion position or trap frequency during prolonged normal operation, leading us to rule out any significant photoelectric effect due to light at 729 nm or 866 nm. Additionally, we conclude that a negligible fraction of power from the 397 nm beam is scattered onto the trap surface.

7.2.3 RF and DC electrodes

In addition to the photoelectric effect, excess charge on the floating wire may also originate from its capacitance to neighboring electrodes. Specifically, we consider both RF and DC electrodes as potential sources of time-dependent and static shifts in the overall floating wire potential.

RF voltage mismatch

Let us first investigate the influence of the RF-electrode voltage on the floating wire's voltage. With a finite-element solver, we calculate the capacitance matrix for all 8 RF electrodes and the central floating wire. As previously stated, we find that the center floating wire has capacitance $C_w = 30$ fF to ground and the 8 RF electrodes have capacitances of ~ 0.5 fF to the center wire. Treating this system as 8 parallel capacitive dividers to ground, we compute the magnitude, $V_{pp}/2$, of oscillating RF pick-up on the center electrode as a function of the voltage mismatch between the two out-of-phase RF arms. The simulation results are shown in Fig. 7.11(left) up to a voltage mismatch up to 15% deviation of each RF arm from the mean voltage of 100 V, i.e. 15% deviation corresponds to $V_{RF+} = 115V$ and $V_{RF-} = -85V$. When $V_{RF+} = V_{RF-}$, the RF pick-up is nearly zero, as the geometrical symmetry and out-of-phase nature of the RF drive electrodes destructively interferes on the center electrode. As we increase the RF voltage deviation, we see an expected linear increase in the RF pick-up.

Additionally, we quantify the effect of the RF voltage mismatch (proportional to RF pick-up) on the ion confinement potential. As shown in Fig. 7.11(right), we see quadratic shifts in the trap frequency at a fixed height of 50 µm. From our experimental measurements,

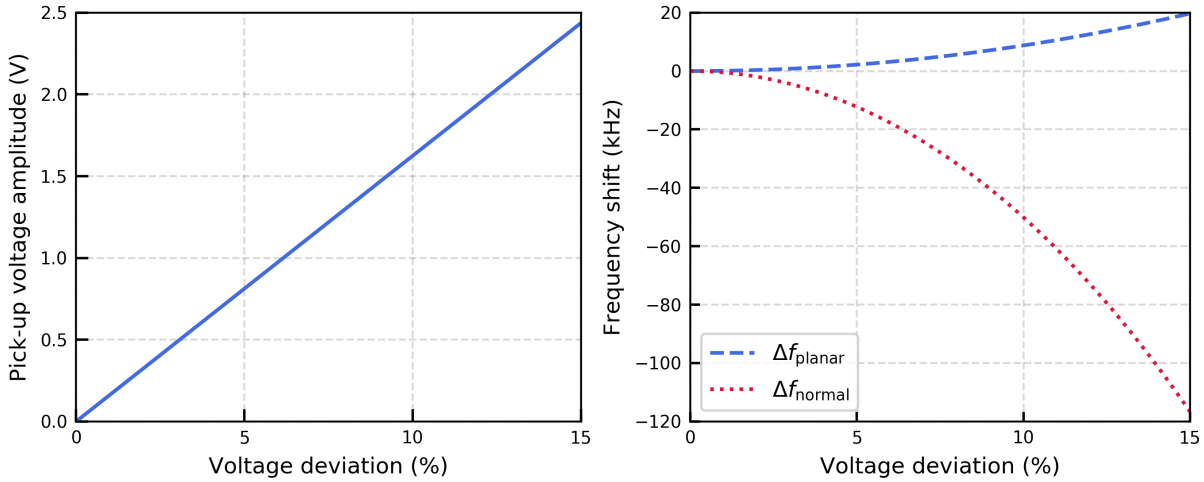

Figure 7.11: (Left) Simulated pick-up voltage on floating wire as a function of RF voltage mismatch on the two RF arms. (Right) Simulated shift of the trap frequencies at 50 µm oriented planar and normal to the trap surface as a function of the RF voltage deviation. Note that a 1% deviation is referenced to a mean voltage of 100 V, i.e. 1% deviation corresponds to $V_{RF+} = 101$ V and $V_{RF-} = -99$ V.

see Section 5.3.2, we find that the RF voltage deviations for each arm are $\sim 10\%$, and can be tuned to be $\lesssim 1\%$. At this level of RF mismatch, the center electrode RF pick-up effect, $\Delta f \sim 500$ Hz, is small compared with typical trap frequencies of $f_t \sim 1$ MHz.

DC cross-talk

Another side-effect of the capacitive coupling between the floating wire and the rest of the trap is a DC shift of the voltage on the floating wire. Specifically, changing the voltage V_i on electrode e_i induces a voltage V_f on the floating wire e_f. This unwanted V_f affects the multipoles at the ion location, and its dependence is shown in Fig. 7.9. Furthermore, the floating wire is shared between the *top* and *bottom* traps of the double trap. Thus, changing any DC electrode voltage in one trap affects the multipoles in both traps.

This cross-talk among the DC electrodes in the double trap leads to difficulties when simultaneously trapping ions in both the *top* and *bottom* traps. From experimental measurements and Fig. 7.9, we find that the primary impact of the cross-talk is a shift in ion height and vertical trap frequency. As such, use of our standard multipole control from Section 4.2.2 is no longer feasible since we may no longer assume all electrode voltages are independent. To be explicit, we must modify our electrode-multipole mapping from the standard,

$$\vec{M} = \mathbf{A}\vec{V}, \tag{7.18}$$

where $\vec{M}$ is the multipole vector, $\mathbf{A}$ is the control matrix that maps electrode voltages to multipoles (each column of $\mathbf{A}$ represents the multipole contributions from one particular

electrode), and $\vec{V}$ is the voltage vector which represents the voltage values for each electrode. For our double trap setup, this standard mapping is given by

$$\begin{pmatrix} M_1^t \\ \vdots \\ M_8^t \\ M_1^b \\ \vdots \\ M_8^b \end{pmatrix} = \begin{pmatrix} \mathbf{T} & \mathbf{0} \\ \mathbf{0} & \mathbf{B} \end{pmatrix} \begin{pmatrix} V_1^t \\ \vdots \\ V_8^t \\ V_1^b \\ \vdots \\ V_8^b \end{pmatrix} = \begin{pmatrix} T_{11} & \dots & T_{18} & & & \\ \vdots & \ddots & \vdots & & \mathbf{0} & \\ T_{81} & \dots & T_{88} & & & \\ & & & B_{11} & \dots & B_{18} \\ & \mathbf{0} & & \vdots & \ddots & \vdots \\ & & & B_{81} & \dots & B_{88} \end{pmatrix} \begin{pmatrix} V_1^t \\ \vdots \\ V_8^t \\ V_1^b \\ \vdots \\ V_8^b \end{pmatrix}, \tag{7.19}$$

where $\mathbf{T}$ and $\mathbf{B}$ are independent control matrices for the *top* trap and *bottom* trap, respectively.

In order to account for the cross-talk among the DC electrodes, we insert a compensation term into the standard multipole control matrix,

$$\vec{M} = \mathbf{A}\vec{V} + \xi \mathbf{mc}\vec{V}. \tag{7.20}$$

Here, our compensation matrix is composed of $\xi\mathbf{mc}$, where $\mathbf{m}$ a diagonal matrix describing the multipole contributions from the floating wire and $\mathbf{c}$ is the capacitance matrix (calculated with a finite-element solver) between each electrode and the floating wire. ξ is a constant scaling factor which allows a degree of freedom for tuning the magnitude of compensation, though $\xi = 1$ is the default value. Explicitly writing out the matrices from Eq. 7.20 gives

$$\begin{pmatrix} M_1^t \\ \vdots \\ M_8^t \\ M_1^b \\ \vdots \\ M_8^b \end{pmatrix} = \begin{pmatrix} \mathbf{T} & \mathbf{0} \\ \mathbf{0} & \mathbf{B} \end{pmatrix} \begin{pmatrix} V_1^t \\ \vdots \\ V_8^t \\ V_1^b \\ \vdots \\ V_8^b \end{pmatrix} + \xi \begin{pmatrix} m_1^t & 0 & \dots & & \dots & 0 \\ 0 & \ddots & & & & \vdots \\ \vdots & & m_8^t & & & \\ & & & m_1^b & & \vdots \\ \vdots & & & & \ddots & 0 \\ 0 & \dots & & \dots & 0 & m_8^b \end{pmatrix} \begin{pmatrix} c_1^t & \dots & c_8^t & c_1^b & \dots & c_8^b \\ \vdots & & \vdots & \vdots & & \vdots \\ c_1^t & \dots & c_8^t & c_1^b & \dots & c_8^b \end{pmatrix} \begin{pmatrix} V_1^t \\ \vdots \\ V_8^t \\ V_1^b \\ \vdots \\ V_8^b \end{pmatrix}. \tag{7.21}$$

With this compensation applied, we find that adjusting DC voltages in one trap no longer shifts the ion height in the other trap. This improvement was imperative for independent control of the *top* and *bottom* traps. However, the cross-talk is not fully compensated, as evidenced from shifts of the vertical trap frequency in one trap when voltages are applied to the other trap. Currently, the trap frequency in one trap shifts on the order of 1 kHz per 100 mV applied to the other trap. Further improvement upon this compensation will require more accurate modeling of the electrode capacitances and potentials.

7.3 Wire mediated ion-ion energy exchange

7.3.1 Experimental overview

In this section, we present experimental results for measured ion-ion coupling and energy exchange enhanced through the use of an electrically floating metallic wire. In our system, two trapped ions, which we distinguish as *auxiliary* (a) and *measurement* (m), are separated by 620 µm. Each is harmonically bound with dc-tunable vertical trap frequencies, ω_a and ω_m. When brought on resonance, $\omega_a = \omega_m$, the vertical motion of ion a induces motion of image charges in the coupling wire, modifying its potential and in turn, influencing the motion of ion m, and vice-versa. Under this resonance condition, the energy of each ion is expected to swap as shown in Fig. 7.2.

Our double trap design, see Section 7.2, is engineered to optimize the coupling of the ion-wire-ion system in terms of speed and stability. With this design, we demonstrate both wire-mediated sympathetic heating (Section 7.3.4) and sympathetic reduction of heating (Section 7.3.5) for separately trapped ions. From the measurements of reduced heating, we extract a coupling rate of $\kappa = 2\pi \times 11$ Hz, in agreement with simulations of the experimental parameters.

Due to abnormally high motional ion heating rates, the ability to measure an oscillating energy exchange, similar to Fig. 7.2, is hindered. In Section 7.4, we discuss potential improvements that may be implemented to lower the heating rates and increase the coupling. Finally, in Section 7.4.3, we review the implications and applications of this work.

7.3.2 Related experiments

No experiment to date has performed energy exchange between two ions through a metal wire. However, two separate groups from NIST Boulder [105] and University of Innsbruck [106] have demonstrated conceptually similar experiments of coupling ions held in two separate potential wells. The coupling mechanism in both cases was simply the mutual Coloumb interaction of the separated ions, with an expected energy exchange rate of

$$\Omega_{ex} = \frac{q_1 q_2}{4\pi\epsilon_0 s^3 \sqrt{m_1 m_2 \omega_1 \omega_2}}, \tag{7.22}$$

where q_i, m_i, ω_i are the charge, mass, and trap frequency of ion i, ϵ_0 is the permittivity of free space, and s is the separation distance between the ions. This corresponds to an exchange time of $t_{\text{ex}} = \pi/(2\Omega_{ex})$. The NIST group measured an exchange time of $t_{\text{ex}} = 155(1)$ µs at 40 µm ion separation, while the Innsbruck group measured $t_{\text{ex}} = 222(10)$ µs at 54 µm ion separation. Both measured values of t_{ex} were close to the predicted values from Eq. 7.22.

The exchange rate decreases with the separation distance as $1/s^3$. This implies that ion-ion coupling in separate potential wells directly through the Coulomb force is limited to close-range interactions. With two ions separated by $s = 620$ µm, we expect an energy exchange time of $t_{\text{ex}} \approx 600$ ms between the motional states of the ions. In comparison, our

wire-mediated coupling achieves an order of magnitude improvement in the energy exchange rate.

7.3.3 Experimental setup

As described in Section 7.2, the RF and DC electronic features of the double trap allow for independent control of vertical trapping height and trap frequency in the *top* and *bottom* traps. Each trap holds a $^{40}Ca^{+}$ ion which is addressed with an independent set of lasers.

Ion loading is performed sequentially in each trap, with a single set of photoionization lasers (at 422 nm and 375 nm) installed onto translation stages for ease of switching between *top* trap and *bottom* trap loading. The 397 nm Doppler cooling beams propagate along the planar $\hat{x}$ axis while the repumping 866 nm beams are oriented normal to the trap surface along the $\hat{z}$ axis.

Since the coupling is sensitive to the vertical ion motion, Doppler cooling in the vertical mode is essential for experimental operations. It would be ideal to perform Doppler cooling of the vertical mode directly with 397 nm light oriented along the vertical axis, but unfortunately, as stated in Section 7.2.2, we find that exposure of light with wavelengths below 422 nm onto the trap induces photoelectric charging of the floating wire. To avoid this situation, Doppler cooling is achieved on the $P_{1/2} \leftrightarrow D_{3/2}$ transition using vertical red-detuned 866 nm beams instead of conventional red-detuned 397 nm beams. The functionality of the planar 397 nm beams remains for Doppler cooling in the planar modes and fluorescent detection of each ion onto separate photomultiplier tubes.

Additional cooling of the vertical mode is performed with incoherent parametric coupling of the vertical and planar modes during Doppler cooling [63]. This scheme reduces the equilibrium temperature achievable in the vertical motional mode by a factor of ~ 4, with a lower limit of 10 mK.

State manipulation is performed by two individually focused 729 nm beams which address the $S_{1/2} \leftrightarrow D_{5/2}$ qubit transitions and point along the vertical modes of each ion. The orientation of these beams as well as the full imaging and detection setup may be seen in Fig. 5.13 of Section 5.4.3. These beams are used to perform carrier Rabi-oscillations, from which the mean motional occupation number, $\bar{n}$, is extracted using fits of these Rabi excitations to thermal state time-evolutions.

7.3.4 Sympathetic heating

As a demonstration of the coupling, we probe the energy exchange between our two remotely trapped ions by measuring the heating rate of ion m near the resonance condition of $\omega_m = \omega_a$. In this experiment, the auxiliary ion a is held 60 µm centered above the *bottom* trap surface with a fixed vertical trap frequency of $\omega_a = 1.3680(6)$ MHz and high temperature. Though we are unable to measure the exact temperature, we estimate $\bar{n}_a \gtrsim 10,000$ quanta. The measurement ion m is initialized to $\bar{n}_m = 200$ quanta at the start of each experiment and located 80 µm above the *top* trap surface at the opposite end of the coupling wire.

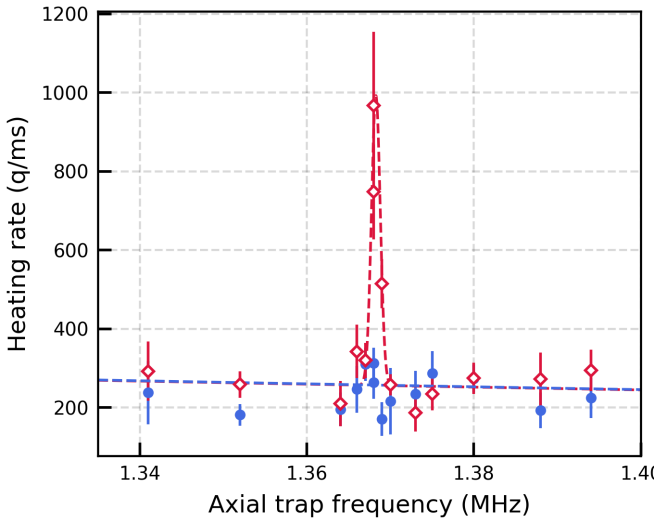

Figure 7.12: Shown in red diamonds is the heating rate, $\dot{\bar{n}}_m$, spectroscopy measured on ion m which demonstrates ion-wire-ion coupling near the resonance condition of $\omega_m = \omega_a = 1.3680(6)$ MHz, where error bars represent one standard deviation. The dashed red curve represents a Gaussian fit with power-law frequency scaling, with an extracted s.d. width of the Gaussian peak to be 527 ± 160 Hz. Blue circles represent $\dot{\bar{n}}_m$ measured with ion a detuned to $\omega_a = 1.4380(6)$ MHz and the dashed blue curve is a power-law fit to the data. No peak is visible within the frequency window, suggesting the coupling is absent, as expected.

Resonant coupling of ion m with ion a is mediated by the shared wire and induces increased heating of ion m. As the trap frequency ω_m is detuned from ω_a, the coupling is turned off, and the heating rate of ion m relaxes to the baseline values of ~ 300 quanta/ms. The data which signals this resonant behavior is shown as red diamonds in Fig. 7.12. We fit this data using a combined Gaussian peak and power-law frequency scaling (dashed red curve) and estimate an interaction width of 527 ± 160 Hz. This implies a vertical trap frequency stability of ~ 370 Hz, which may be caused by high ion temperatures and trap frequency broadening from anharmonicities in the trapping potential, see Section 7.3.5. Unfortunately, we cannot take advantage of techniques to directly measure the vertical trap frequency stability due to our inability to perform ground state cooling and aversion to shine 397 nm light vertically onto the floating center wire. An additional contribution to the large measured interaction width may be the voltage cross-talk effect discussed in Section 7.2.3. From this effect, we have measured that changing the vertical trap frequency of ion m by $\Delta\omega_m = 4$ kHz shifts the vertical trap frequency of ion a by $\Delta\omega_a = 1$ kHz in the same direction. This cross-talk is expected to result in a 25% increase in the interaction width.

To verify the resonant peak as a true signal of the coupling, i.e. not an artifact of technical noise, we measure the heating rate of ion m across the same frequency range while ion a is set to a detuned vertical trap frequency of $\omega_a = 1.4380(6)$ MHz. The data for this far off-resonant measurement are shown as blue circles in Fig. 7.12 and fit to a power-law frequency

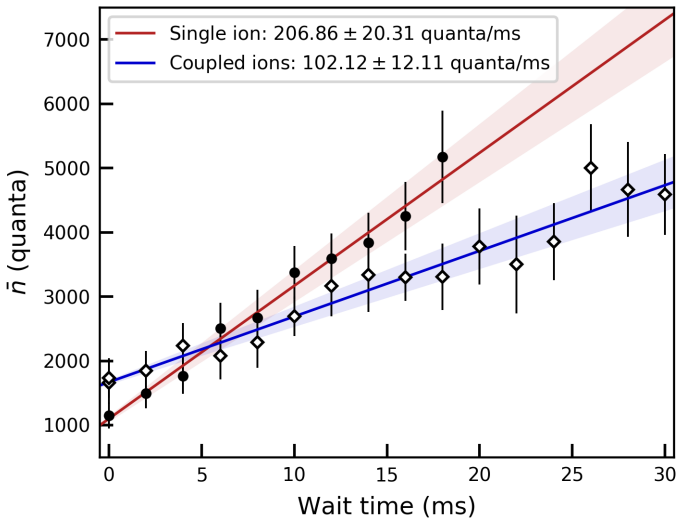

Figure 7.13: Motional occupation, $\bar{n}$, of ion m is plotted with error bars representing one standard deviation. The $\bar{n}$ heating of a single ion is plotted (dots) along with a heating rate fit of 206(20) quanta per millisecond (red). A second experiment (diamonds) demonstrates sympathetic reduction of heating of ion m induced by resonant wire-mediated energy exchange with ion a held at 182(15) quanta, resulting in a reduced heating rate of 102(12) quanta per millisecond (blue).

scaling (dashed blue curve). With no discernible peak in this off-resonant dataset, we infer that the resonant data (in red) is valid and not caused by technical noise at 1.3680(6) MHz. In addition, we measure the single-ion heating rates of ion m in the complete absence of ion a and, as expected, find agreement with the data shown in blue.

Because we are unable to measure the initial temperature of ion a, a calculation of the coupling rate cannot be determined from this data.

7.3.5 Sympathetic reduction of heating

In order to extract a coupling rate, we move the ions to a regime with lower noise by increasing the resonance frequency from 1.368 MHz to 1.990 MHz. Under this condition, we may monitor the temperature of the auxiliary ion during resonant coupling. Additionally, the ions are shuttled to lower heights (50 µm for ion m and 70 µm for ion a) to increase the coupling signal. Because of the large electric-field noise present in our double trap system, is it not possible to observe the oscillations of energy exchange between ion m and ion a. However, this does not preclude extraction of a coupling rate.

With these parameters, we demonstrate wire-mediated sympathetic reduction of heating of ion m with ion a using a two-part measurement sequence. The first part involves only a single ion m trapped at 50 µm height with no ion present in the companion trap. In this simple configuration, we measure a baseline heating rate of 206(20) quanta per millisecond

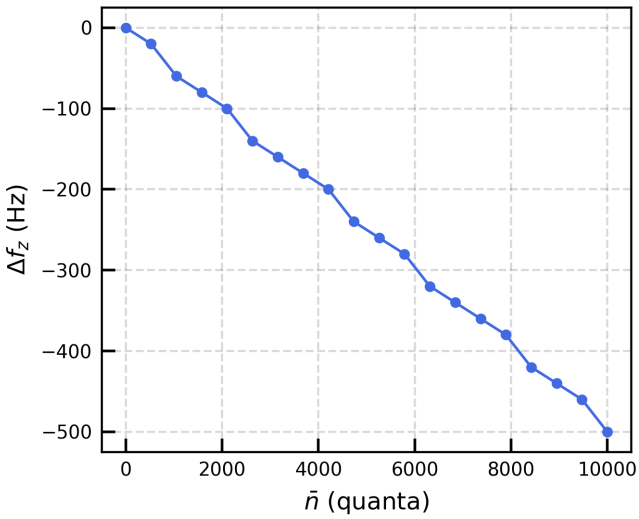

Figure 7.14: Simulated ω_z trap frequency shift in a trapping potential expanded to fourth order, centered at 70 µm height, and with nominal ω_z.

at $\omega_m = 1.9900(6)$ MHz, extracted from the red fit line in Fig. 7.13.

In the second part, we work with one ion in each trapping site. The auxiliary ion a is trapped at 70 µm height, held at a constant temperature of $\bar{n} = 182(15)$ quanta, and set to be resonant with ω_m for the entire duration of the experiment. As per the first part, we measure the time-evolution of the motional occupation of ion m and observe a reduction in heating rate to 102(12) quanta per millisecond, see blue fit in Fig. 7.13.

With a classical model of the ion motions, we extract an effective coupling rate of $\kappa = 2\pi \times 11.23$ Hz from the data in Fig. 7.13, corresponding to an energy exchange time of $t_{\text{ex}} = 22.3$ ms. The 9% difference between our measured exchange time of $t_{\text{ex}} = 22.3$ ms and the predicted exchange time of $t_{\text{ex}} = 24.6$ ms from Eq. 7.13 is likely due to uncertainties in the simulated wire capacitance, C_w, or uncertainties in the ion heights of ion a and ion m. As comparison, this wire-mediated energy exchange rate is ~ 60 times faster than the expected bare Coulomb coupling of 1.347 s for a $2\pi \times 1.99$ MHz resonant interaction frequency.

Anharmonic potentials

One side-effect of working with high $\bar{n}$ values is the presence trap frequency shifts due to higher-order anharmonic parts of the trapping potential. Under standard operation, the dynamics of ion motion within our traps are approximated using harmonic potentials. As discussed in Section 4.2.2, full control of the DC multipoles up to second order may be achieved with our elevator trap design. However, the trap design does not include enough degrees of freedom to control multipoles beyond the dipoles and quadrupoles. In particular, the fourth order multipole coefficient (C_4) in the vertical direction, z^4, is uncontrolled. A non-zero C_4 coefficient is negligible in standard trapped ion experiments because the ion

is typically held near the motional ground state, with $\sim$ 20 nm extent for $^{40}Ca^{+}$ at $\omega_t = 2\pi \times 1$ MHz. However, our experiments work with ion motional occupations up to $\bar{n} = 5000$ quanta, corresponding to a spatial extend of ~ 1.6 µm of the vertical ion motion.

As the extent of the ion motion increases with higher ion temperatures, the ion samples the trapping potential far from the minimum. In this regime, the C_4 component becomes relevant to the ion dynamics. Specifically, the trap frequency shifts relative to that of a low-temperature ion. We simulate this shift in Fig. 7.14 and find a linear trap frequency shift of ~ 50 Hz per 1000 $\bar{n}$ at 70 µm trapping height and nominal trap frequency of $\omega_z = 2\pi \times 2$ MHz.

Preliminary measurements of trap frequency as a function of $\bar{n}$ confirm the presence of frequency shifts caused by anharmonicities. However, further investigation is required in order to determine the actual magnitude and trend of the trap frequency shifts. Regardless, the frequency shift acts as an effective time-dependent detuning to the coupling experiment. This implies that, without compensation, the effective coupling strength between the remotely trapped ions is reduced as $\Delta\bar{n} = \bar{n}_m - \bar{n}_a$ deviates from the initial temperatures.

7.4 Conclusions

To conclude, we have established classical energy exchange between two remotely trapped ions enhanced via a solid-state wire. We believe this is the first demonstration of wire-mediated ion-ion energy exchange in an RF (Paul) trap structure. This achievement opens the path for sympathetic cooling of one remote ion with another, regardless of ion species. This may enable precision measurements of ion species not amenable to laser cooling and grants potential control of negatively charged ions and antiprotons. Our results, shown in Section 7.3, are a culmination of 15 years worth of theoretical and experimental efforts. Prior to my time with the Häffner lab, several technical hurdles were cleared, and as the torch was passed to me, two main challenges remained: (1) operate and characterize our novel elevator trap with out-of-phase RF drive, and (2) understand the effects associated with our integrated floating center wire and establish control of ions trapped above the wire. Over the course of my thesis work, these two challenges were successfully surmounted, as addressed in Chapters 4, 6, and 7.

The original goal of these experiments was to verify that quantum entanglement can be mediated through a normal conducting wire. Unfortunately, even with our efforts and accomplishments over the years, this goal remains out of reach. In this final section, we discuss possible improvements to the wire-mediated coupling which may help bring the energy exchange into the single-quantum regime and allow for wire-mediated quantum entanglement between remote ions. Such an endeavor is by no means trivial and would likely require several more years of diligent work. In addition, this wire technology may still lag behind other quantum transport techniques, such as ion shuttling or photonic entanglement, in terms of speed and fidelity. However, if the issues of coupling speed and noise are drastically improved (at least 2 orders of magnitude faster coupling and 3 orders of magnitude lower noise), our

ion-wire-ion coupling may become an indispensable tool for many applications in quantum computation and spectroscopy.

7.4.1 Heating rate reduction

Foremost, we tackle the impediment of high intrinsic heating rates in our trap, which limit the effective sympathetic cooling rate, trap stability, and measurement precision. Our measurements of 207 quanta/ms at $\omega_z = 2\pi \times 1.99$ MHz and 50 µm trapping height are roughly two orders of magnitude higher than those measured in our elevator trap, see Chapter 6. Our elevator trap and double trap are fabricated on the same trap chip and operated under the same experimental conditions. Thus, we believe that the source of noise causing high heating rates in the double trap is the floating electrode wire. From simulations of such noise, we find that 5 µV amplitude noise on the floating wire would account for the measured heating rates. As comparison, we refer back to Fig. 6.4, where technical noise of amplitude 3 µV on the center electrode of the elevator trap corresponds to vertical heating rates on the order of 100 quanta/ms. In the elevator trap, our measured heating rates at 50 µm ion height and $\omega_t = 2\pi \times 1$ MHz trap frequency were on the order of 1 quanta/ms, implying a technical noise amplitude on the center electrode well below 30 nV.

The origin behind the floating wire noise is presently unclear and requires additional measurements to determine. Discussions with Markus Teller, Philipp Schindler, and Tracy Northup from the University of Innsbruck lead us to believe that the noise originates from the dielectric material below the floating wire. Electric-field noise induced by dielectric materials has been shown to affect the heating of ions trapped nearby [89]. Standard surface traps are typically insensitive to such dielectric noise because the grounded metal surface layer acts as an electrical shield between the dielectric and the ion. In contrast, we expect that our electrically floating wire distributes the noise from the dielectric over the entire center wire, effectively translating the dielectric noise into technical noise on the wire and resulting in simulated ion heating rates of order 100 quanta/ms. Other candidates for such high heating rates are the motion of charge carriers on the floating electrode wire or relative technical noise voltage fluctuations between the floating wire and the trap ground.

From an experimental perspective, we may employ established techniques to reduce the noise in our trap to workable levels. One such technique is in-situ Ar^+ bombardment, which has been shown to reduce ion heating rates by two orders of magnitude [116, 117]. Due to the floating wire, care must be taken during the Ar^+ treatment to prevent excessive build-up of charge which may prevent further sputtering. From our experimental results in Section 7.2.2, we believe this issue may be mitigated with a controlled photoelectric effect. A caveat of this technique is that it affects only the trap surface, meaning any noise originating from the dielectric beneath the floating wire will not be altered. In this case, the only solution may be to utilize a different dielectric material underneath the floating wire or remove the dielectric completely. Another tactic for reducing the noise is to operate the ion trap at cryogenic temperatures, where previous groups have also shown reduced heating rates by two orders of magnitude [75, 118, 119, 43, 120, 49].

7.4.2 Enhancements

With an established low-noise system, we may further improve the coupling strength by increasing the ion motional dipole in each trap. The first strategy for this enhancement is to increase the total number of ions [105], which will result in a linear increase to the coupling rate according to Eq. 7.13. A second pathway towards faster coupling rates is to lower the resonant coupling frequency, which also provides a linear advantage. Moreover, the trap design and wire design may be further engineered to deliver even faster exchange rates.

7.4.3 Applications

From our demonstration of classical energy exchange through a wire, there are immediate applications to sympathetic cooling of one remote ion with another using an RF (Paul) trap. With only moderate reduction of the noise in our system (1 order of magnitude) or moderate increase in the coupling rate (1 order of magnitude), we believe our wire-mediated scheme may lead to sympathetically cooled ion temperatures of order 100 mK, comparable to dilution refrigerator temperatures. At these low temperatures, precision measurements of previously difficult to cool ion species become possible. Because this coupling technique is agnostic to ion species, the wire design may allow sympathetic cooling, trapping, and detection of charged particles which are otherwise difficult to work with, such as antiprotons [121] or electrons [113]. In fact, the coupling strength increases by two orders of magnitude when replacing $^{40}Ca^{+}$ ions with trapped electrons at ~ 100 MHz trap frequency. Additionally, such experiments would require cryogenic operation, reducing the system's inherent electric-field noise.

Any further applications will require significant improvements in the experimental setup. Specifically, we must reduce the current noise in our system in order to lower the ion heating rates from ~ 100 quanta/ms to at most ~ 100 quanta/s. Although we mention a few methods for achieving lower heating rates in Section 7.4.1, they are difficult to implement and are in no way guaranteed to reduce our noise by more than 3 orders of magnitude. Additionally, in order to compete with remote coupling via ion shuttling, our wire-mediated coupling rate of $\kappa = 2\pi \times 11.23$ Hz must quicken by at least 2 orders of magnitude to $\kappa \sim 2\pi \times 1$ kHz. Though we suggest a few paths toward faster coupling rates in Section 7.4.2, further improvement will require a paradigm shift in the trap design or wire geometry.

If we are able to achieve faster coupling rates with reduced levels of motional heating, we can then generate deterministic entanglement between the qubit sqin states of two separated ions. By initializing one ion, a, in the first excited state and the other ion, b, in the motional ground state, the combined motional state is $|1\rangle_a |0\rangle_b$. If the wire-mediated coupling is then turned on for a time $t = t_{\text{ex}}/2$, our combined motional state evolves into the Bell state $(|1\rangle_a |0\rangle_b + i |0\rangle_a |1\rangle_b)/\sqrt{2}$. This entangled motional state may be transferred onto the internal qubit spin states with sideband pulses in order to create an entangled two-ion spin state [122, 105, 106].

This remote entanglement capability would lead to several potential applications in quantum computation and spectroscopy for our wire-mediated coupling architecture. It could be used to facilitate entangled-pair factories [72, 44], where the need for ion shuttling is replaced with a solid-state link of the ions in separate wells. In addition, the coupling may be used to readout the spin state of one remote ion with another, a process which is useful for error correction protocols and quantum logic spectroscopy [123]. A combination of these methods may lead to scalable arrays of ion registers connected by wires, facilitate the development of electron qubit architectures, and aid the development of hybrid quantum systems, where this coupling mechanism may serve as a quantum bridge between trapped ion qubits and superconducting qubits [124, 125, 126].

Bibliography

[1] D. Leibfried et al. "Quantum dynamics of single trapped ions". In: *Reviews of Modern Physics* 75.1 (Mar. 2003), pp. 281–324. ISSN: 0034-6861. DOI: 10.1103/RevModPhys.75.281. URL: http://dx.doi.org/10.1103/RevModPhys.75.281.

[2] T. P. Harty et al. "High-Fidelity Preparation, Gates, Memory, and Readout of a Trapped-Ion Quantum Bit". In: *Physical Review Letters* 113.22 (Nov. 2014), p. 220501. ISSN: 0031-9007. DOI: 10.1103/PhysRevLett.113.220501. URL: https://link.aps.org/doi/10.1103/PhysRevLett.113.220501.

[3] J. P. Gaebler et al. "High-Fidelity Universal Gate Set for Be Ion Qubits". In: *Physical Review Letters* 117.6 (Aug. 2016), p. 060505. DOI: 10.1103/PhysRevLett.117.060505. URL: https://link.aps.org/doi/10.1103/PhysRevLett.117.060505.

[4] C. J. Ballance et al. "High-Fidelity Quantum Logic Gates Using Trapped-Ion Hyperfine Qubits". In: *Physical Review Letters* 117.6 (Aug. 2016), p. 060504. ISSN: 0031-9007. DOI: 10.1103/PhysRevLett.117.060504. URL: https://link.aps.org/doi/10.1103/PhysRevLett.117.060504.

[5] D J Wineland et al. "Experimental Issues in Coherent Quantum-State Manipulation of Trapped Atomic Ions". In: *Journal of Research of the National Institute for Standards and Technology* 103.3 (1998), pp. 259–328. URL: https://tf.nist.gov/general/pdf/1275.pdf.

[6] M. Brownnutt et al. "Ion-trap measurements of electric-field noise near surfaces". In: *Reviews of Modern Physics* 87.4 (Dec. 2015), pp. 1419–1482. ISSN: 0034-6861. DOI: 10.1103/RevModPhys.87.1419. URL: http://link.aps.org/doi/10.1103/RevModPhys.87.1419.

[7] Q A Turchette et al. "Heating of trapped ions from the quantum ground state". In: *Physical Review A* 61 (2000), p. 063418. DOI: 10.1103/PhysRevA.61.063418.

[8] R. Dubessy, T. Coudreau, and L. Guidoni. "Electric field noise above surfaces: A model for heating-rate scaling law in ion traps". In: *Physical Review A* 80.3 (Sept. 2009), 031402(R). DOI: 10.1103/PhysRevA.80.031402. URL: http://link.aps.org/doi/10.1103/PhysRevA.80.031402.

[9] Guang Hao Low, Peter F Herskind, and Isaac L Chuang. "Finite-geometry models of electric field noise from patch potentials in ion traps". In: *Physical Review A* 84.5 (Nov. 2011), p. 053425. DOI: 10.1103/PhysRevA.84.053425. URL: http://link.aps.org/doi/10.1103/PhysRevA.84.053425.

[10] M. Kim et al. "Decoherence of Near-Surface Nitrogen-Vacancy Centers Due to Electric Field Noise". In: *Physical Review Letters* 115.8 (Aug. 2015), p. 87602. ISSN: 0031-9007. DOI: 10.1103/PhysRevLett.115.087602. URL: https://link.aps.org/doi/10.1103/PhysRevLett.115.087602.

[11] J. B. Camp, T. W. Darling, and Ronald E. Brown. "Macroscopic variations of surface potentials of conductors". In: *Journal of Applied Physics* 69.10 (1991), pp. 7126–7129. ISSN: 00218979. DOI: 10.1063/1.347601.

[12] T. W. Darling et al. "The fall of charged particles under gravity: A study of experimental problems". In: *Reviews of Modern Physics* 64.1 (1992), pp. 237–257. ISSN: 00346861. DOI: 10.1103/RevModPhys.64.237.

[13] V. Sandoghdar et al. "Direct measurement of the van der Waals interaction between an atom and its images in a micron-sized cavity". In: *Physical Review Letters* 68.23 (June 1992), p. 3432. DOI: 10.1103/PhysRevLett.68.3432.

[14] D. M. Harber et al. "Measurement of the Casimir-Polder force through center-of-mass oscillations of a Bose-Einstein condensate". In: *Physical Review A* 72.3 (Sept. 2005), p. 033610. DOI: 10.1103/PhysRevA.72.033610.

[15] D. Gorman. "Noise sensing and quantum simulation with trapped atomic ions". PhD thesis. University of California, Berkeley, 2018. URL: http://research.physics.berkeley.edu/haeffner/publications/dylan_gorman_thesis.pdf.

[16] Wolfgang Paul. "Electromagnetic traps for charged and neutral particles". In: *Reviews of Modern Physics* 62.3 (July 1990), pp. 531–540. ISSN: 0034-6861. DOI: 10.1103/RevModPhys.62.531. URL: http://link.aps.org/doi/10.1103/RevModPhys.62.531.

[17] D. J. Berkeland et al. "Minimization of ion micromotion in a Paul trap". In: *Journal of Applied Physics* 83.10 (May 1998), pp. 5025–5033. ISSN: 0021-8979. DOI: 10.1063/1.367318. URL: http://aip.scitation.org/doi/10.1063/1.367318.

[18] M Abramowitz and I A Stegun. "Handbook of mathematical functions". In: New York: Dover, 1972, p. 784.

[19] N. W McLachlan. *Theory and Applications of Mathieu Functions*. Oxford, Clarendon Press, 1947.

[20] M. Drewsen and A. Brøner. "Harmonic linear Paul trap: Stability diagram and effective potentials". In: *Phys. Rev. A* 62.4 (2000), p. 045401. DOI: 10.1103/PhysRevA.62.045401. URL: https://link.aps.org/doi/10.1103/PhysRevA.62.045401.

[21] H. Häffner, C. F. Roos, and R. Blatt. "Quantum computing with trapped ions". In: *Physics Reports* 469.September (Dec. 2008), pp. 155–203. ISSN: 03701573. DOI: 10.1016/j.physrep.2008.09.003. URL: http://linkinghub.elsevier.com/retrieve/pii/S0370157308003463.

[22] S. Debnath et al. "Demonstration of a small programmable quantum computer with atomic qubits". In: *Nature* 536.7614 (Aug. 2016), pp. 63–66. ISSN: 0028-0836. DOI: 10.1038/nature18648.

[23] Signe Seidelin et al. "Microfabricated Surface-Electrode Ion Trap for Scalable Quantum Information Processing". In: *Physical Review Letters* 96.25 (June 2006), p. 253003. ISSN: 0031-9007. DOI: 10.1103/PhysRevLett.96.253003. URL: https://www.nist.gov/publications/microfabricated-surface-electrode-ion-trap-scalable-quantum-information-processing%20https://link.aps.org/doi/10.1103/PhysRevLett.96.253003.

[24] J. Chiaverini et al. "Surface-electrode architecture for ion-trap quantum information processing". In: *Quantum Information and Computation* 5 (2005), pp. 419–439. URL: http://dl.acm.org/citation.cfm?id=2011670.2011671.

[25] C E Pearson et al. "Experimental investigation of planar ion traps". In: *Physical ReviewA* 73 (2006), p. 32307. DOI: 10.1103/PhysRevA.73.032307. URL: https://journals.aps.org/pra/pdf/10.1103/PhysRevA.73.032307.

[26] G. Shu et al. "Heating rates and ion-motion control in a y -junction surface-electrode trap". In: *Physical Review A* 89 (2014), p. 62308. DOI: 10.1103/PhysRevA.89.062308.

[27] Kenneth Wright et al. "Reliable transport through a microfabricated X -junction surface-electrode ion trap". In: *New Journal of Physics* 15.3 (Mar. 2013), p. 33004. ISSN: 1367-2630. DOI: 10.1088/1367-2630/15/3/033004. URL: http://stacks.iop.org/1367-2630/15/i=3/a=033004?key=crossref.2dd5f3491da25e9c8caeae276f2259b1.

[28] D L Moehring et al. "Design, fabrication and experimental demonstration of junction surface ion traps". In: *New Journal of Physics* 13.7 (July 2011), p. 75018. ISSN: 1367-2630. DOI: 10.1088/1367-2630/13/7/075018. URL: http://stacks.iop.org/1367-2630/13/i=7/a=075018?key=crossref.e67b9e2fdf0c3cb16ebabb1be06b0715.

[29] Hao-Kun Li et al. "Realization of Translational Symmetry in Trapped Cold Ion Rings". In: *Physical Review Letters* 118.5 (Jan. 2017), p. 053001. ISSN: 10797114. DOI: 10.1103/PhysRevLett.118.053001. arXiv: 1605.02143 [quant-ph]. URL: https://link.aps.org/doi/10.1103/PhysRevLett.118.053001.

[30] D. An et al. "Surface trap with dc-tunable ion-electrode distance". In: *Review of Scientific Instruments* 89.9 (Sept. 2018), p. 093102. DOI: 10.1063/1.5046527. URL: http://aip.scitation.org/doi/10.1063/1.5046527.

[31] Karan K. Mehta et al. "Integrated optical addressing of an ion qubit". In: *Nature Nanotechnology* 11 (Aug. 2016), pp. 1066–1070. ISSN: 1748-3387. DOI: 10.1038/nnano.2016.139. URL: http://www.nature.com/doifinder/10.1038/nnano.2016.139.

[32] D T C Allcock et al. "Implementation of a symmetric surface-electrode ion trap with field compensation using a modulated Raman effect". In: *New Journal of Physics* 12.5 (May 2010), p. 053026. ISSN: 1367-2630. DOI: 10.1088/1367-2630/12/5/053026. URL: http://stacks.iop.org/1367-2630/12/i=5/a=053026?key=crossref.942f3fda4048764a9c1b665dc4e40e23.

[33] Thaned Pruttivarasin. "Spectroscopy , fundamental symmetry tests and quantum simulation with trapped ions". PhD thesis. University of California, Berkeley, 2014, p. 141.

[34] Michael Ramm et al. "Precision Measurement Method for Branching Fractions of Excited P$_{1/2}$ States Applied to $ˆ{40}$Ca$ˆ{+}$". In: *Physical Review Letters* 111.2 (July 2013), p. 023004. ISSN: 0031-9007. DOI: 10.1103/PhysRevLett.111.023004. URL: http://dx.doi.org/10.1103/PhysRevLett.111.023004.

[35] P A Barton et al. "Measurement of the lifetime of the 3d ˆ2D_5/2 state in ˆ40Caˆ+". In: *Phys. ˜Rev. ˜A* 62 (2000), p. 32503.

[36] Christian Felix Roos. "Controlling the quantum state of trapped ions". PhD thesis. University of Innsbruck, 2000.

[37] D Leibfried et al. "Experimental demonstration of a robust, high-fidelity geometric two ion-qubit phase gate". In: *Nature* 422 (2003), pp. 412–415. DOI: 10.1038/nature01492. URL: http://dx.doi.org/10.1038/nature01492.

[38] Stig Stenholm. "The semiclassical theory of laser cooling". In: *Reviews of Modern Physics* 58.3 (July 1986), pp. 699–739. ISSN: 0034-6861. DOI: 10.1103/RevModPhys.58.699. URL: http://link.aps.org/doi/10.1103/RevModPhys.58.699.

[39] R Loudon. *The Quantum Theory of Light*. Oxford University Press, 1983.

[40] C. C. (Christopher C.) Gerry and Peter (Peter L.) Knight. *Introductory quantum optics*. Cambridge University Press, 2005, p. 317. ISBN: 052152735X.

[41] C Monroe et al. "Resolved-sideband Raman cooling of a bound atom to the 3D zero-point energy." In: *Physical Review Letters* 75 (1995), pp. 4011–4014. DOI: 10.1103/PhysRevLett.75.4011. URL: https://journals.aps.org/prl/abstract/10.1103/PhysRevLett.75.4011.

[42] R. B. Blakestad et al. "High-Fidelity Transport of Trapped-Ion Qubits through an X-Junction Trap Array". In: *Phys. Rev. Lett.* 102.15 (Apr. 2009), p. 153002. ISSN: 0031-9007. DOI: 10.1103/PhysRevLett.102.153002. URL: http://link.aps.org/doi/10.1103/PhysRevLett.102.153002.

[43] J. Chiaverini and J. M. Sage. "Insensitivity of the rate of ion motional heating to trap-electrode material over a large temperature range". In: *Physical Review A* 89.1 (Jan. 2014), p. 012318. ISSN: 1050-2947. DOI: 10.1103/PhysRevA.89.012318. URL: http://link.aps.org/doi/10.1103/PhysRevA.89.012318.

[44] D Kielpinski, C Monroe, and D J Wineland. "Architecture for a large-scale ion-trap quantum computer." In: *Nature* 417.6890 (2002), pp. 709–711. ISSN: 0028-0836. DOI: 10.1038/nature00784. URL: http://www.ncbi.nlm.nih.gov/pubmed/12066177.

[45] J. H. Wesenberg. "Electrostatics of surface-electrode ion traps". In: *Physical Review A* 78.6 (Dec. 2008), p. 063410. DOI: 10.1103/PhysRevA.78.063410. URL: http://link.aps.org/doi/10.1103/PhysRevA.78.063410.

[46] Philipp Schindler et al. "Polarization of electric-field noise near metallic surfaces". In: *Physical Review A* 92.1 (July 2015), p. 13414. ISSN: 1050-2947. DOI: 10.1103/PhysRevA.92.013414. URL: https://link.aps.org/doi/10.1103/PhysRevA.92.013414%20http://link.aps.org/doi/10.1103/PhysRevA.92.013414.

[47] Gebhard Littich. *Electrostatic Control and Transport of Ions on a Planar Trap for Quantum Information Processing*. Tech. rep. ETH Z¨urich and University of California, Berkeley, 2011.

[48] Ivan A. Boldin, Alexander Kraft, and Christof Wunderlich. "Measuring Anomalous Heating in a Planar Ion Trap with Variable Ion-Surface Separation". In: *Physical Review Letters* 120 (2018), p. 023201. ISSN: 10797114. DOI: 10.1103/PhysRevLett.120.023201.

[49] J. A. Sedlacek et al. "Distance scaling of electric-field noise in a surface-electrode ion trap". In: *Physical Review A* 97 (2018), 020302(R). DOI: 10.1103/PhysRevA.97.020302.

[50] Da An et al. "Distance scaling and polarization of electric-field noise in a surface ion trap". In: *Phys Rev A* 100.6 (Dec. 2019), p. 063405. ISSN: 24699934. DOI: 10.1103/PhysRevA.100.063405.

[51] B. Lekitsch et al. "Blueprint for a microwave trapped-ion quantum computer". In: *Science Advances* 3.2 (2017), e1601540. DOI: 10.1126/sciadv.1601540.

[52] C. Ospelkaus et al. "Microwave quantum logic gates for trapped ions". In: *Nature* 476.7359 (Aug. 2011), pp. 181–184. ISSN: 0028-0836. DOI: 10.1038/nature10290. URL: http://dx.doi.org/10.1038/nature10290%20https://ws680.nist.gov/publication/get_pdf.cfm?pub_id=908366.

[53] F. Mintert and C. Wunderlich. "Ion-Trap Quantum Logic Using Long-Wavelength Radiation". In: *Physical Review Letters* 87 (2001), p. 257904. DOI: 10.1103/PhysRevLett.87.257904. URL: http://dx.doi.org/10.1103/PhysRevLett.87.257904%20https://journals.aps.org/prl/pdf/10.1103/PhysRevLett.87.257904.

[54] Shannon X. Wang et al. "Laser-induced charging of microfabricated ion traps". In: *Journal of Applied Physics* 110 (2011), p. 104901. DOI: 10.1063/1.3662118.

[55] D. T. C. Allcock et al. "Heating rate and electrode charging measurements in a scalable, microfabricated, surface-electrode ion trap". In: *Applied Physics B* 107.4 (Nov. 2011), pp. 913–919. ISSN: 0946-2171. DOI: 10.1007/s00340-011-4788-5. URL: http://link.springer.com/10.1007/s00340-011-4788-5.

[56] M Harlander et al. "Trapped-ion probing of light-induced charging effects on dielectrics". In: *New Journal of Physics* 12.9 (Sept. 2010), p. 093035. ISSN: 1367-2630. DOI: 10.1088/1367-2630/12/9/093035. URL: http://stacks.iop.org/1367-2630/12/i=9/a=093035?key=crossref.aefbc4412f74c34855eaf78da989a855.

[57] N Daniilidis et al. "Wiring up trapped ions to study aspects of quantum information". In: *J. Phys. B* 42.15 (Aug. 2009), p. 154012. ISSN: 0953-4075. DOI: 10.1088/0953-4075/42/15/154012. URL: http://stacks.iop.org/0953-4075/42/i=15/a=154012?key=crossref.c85ec400f8b1c300df78abfce5d7ce88.

[58] Crystal Noel. "High temperature studies of electric-field noise in a surface ion trap". PhD thesis. University of California, Berkeley, 2019. URL: http://www.physics.berkeley.edu/research/haeffner/publications/Noel_thesis.pdf.

[59] Maya Berlin-Udi. "Treatments of a Surface Ion Trap: A Study of Electric-Field Noise near a Contaminated Metal Surface". PhD thesis. University of California, Berkeley, 2020.

[60] Soenke Moeller. "How to couple trapped ions to superconducting resonators: towards hybrid quantum devices". PhD thesis. 2016.

[61] J. D. Siverns et al. "On the application of radio frequency voltages to ion traps via helical resonators". In: *Applied Physics B: Lasers and Optics* 107.4 (2012), pp. 921–934. ISSN: 09462171. DOI: 10.1007/s00340-011-4837-0.

[62] J. Keller et al. "Precise determination of micromotion for trapped-ion optical clocks". In: *Journal of Applied Physics* 118 (2015), p. 104501. DOI: 10.1063/1.4930037.

[63] Dylan J Gorman et al. "Two-mode coupling in a single-ion oscillator via parametric resonance". In: *Physical Review A* 89.6 (June 2014), p. 062332. ISSN: 1050-2947. DOI: 10.1103/PhysRevA.89.062332. URL: http://link.aps.org/doi/10.1103/PhysRevA.89.062332.

[64] I. Talukdar et al. "Implications of surface noise for the motional coherence of trapped ions". In: *Physical Review A* 93.4 (Apr. 2016), p. 043415. ISSN: 2469-9926. DOI: 10.1103/PhysRevA.93.043415. URL: http://link.aps.org/doi/10.1103/PhysRevA.93.043415.

[65] K. Deng et al. "A modified model of helical resonator with predictable loaded resonant frequency and Q-factor". In: *Review of Scientific Instruments* 85.10 (Oct. 2014). ISSN: 10897623. DOI: 10.1063/1.4897478.

[66] S R Jefferts et al. "Coaxial-resonator-driven rf (Paul) trap for strong confinement." In: *Phys. ˜Rev. ˜A* 51 (1995), pp. 3112–3116.

[67] D. Gandolfi et al. *Compact radio-frequency resonator for cryogenic ion traps*. Aug. 2012. DOI: 10.1063/1.4737889.

[68] Long-Sheng Ma et al. *Delivering the same optical frequency at two places: accurate cancellation of phase noise introduced by an optical fiber or other time-varying path*. Tech. rep. 21. 1994, p. 1777.

[69] Karin Fisher. "Trapped Ion Quantum Information Coherent Control Laser System for the Quantum State Manipulation of Trapped Ions". PhD thesis. ETH Zurich, 2013.

[70] G Kirchmair et al. "Deterministic entanglement of ions in thermal states of motion". In: *New J. Phys.* 11.2 (Feb. 2009), p. 23002. ISSN: 1367-2630. DOI: 10.1088/1367-2630/11/2/023002. URL: http://stacks.iop.org/1367-2630/11/i=2/a=023002?key=crossref.be3fc247c634554dc69f59ebce95a834.

[71] T Rosenband et al. "Frequency ratio of Al+ and Hg+ single-ion optical clocks: metrology at the 17th decimal place." In: *Science (New York, N.Y.)* 319.5871 (Mar. 2008), pp. 1808–12. ISSN: 1095-9203. DOI: 10.1126/science.1154622. URL: http://www.ncbi.nlm.nih.gov/pubmed/18323415.

[72] D.J. Wineland et al. "Experimental Primer on the Trapped Ion Quantum Computer". In: *Fortschritte der Physik* 46.4-5 (June 1998), pp. 363–390. ISSN: 0015-8208. DOI: 10.1002/(SICI)1521-3978(199806)46:4/5<363::AID-PROP363>3.0.CO;2-4. URL: http://doi.wiley.com/10.1002/(SICI)1521-3978(199806)46:4/5%3C363::AID-PROP363%3E3.0.CO;2-4.

[73] C. Henkel, S. Pötting, and M. Wilkens. "Loss and heating of particles in small and noisy traps". In: *Applied Physics B: Lasers and Optics* 69.5-6 (Dec. 1999), pp. 379–387. ISSN: 0946-2171. DOI: 10.1007/s003400050823. URL: http://www.springerlink.com/openurl.asp?genre=article&id=doi:10.1007/s003400050823%20http://www.springerlink.com/openurl.asp?genre=article%7B&%7Did=doi:10.1007/s003400050823.

[74] F. Intravaia, S. Maniscalco, and A. Messina. *Density-matrix operatorial solution of the non-Markovian master equation for quantum Brownian motion*. 2003. DOI: 10.1103/PhysRevA.67.042108.

[75] L Deslauriers et al. "Scaling and suppression of anomalous heating in ion traps." In: *Phys. Rev. Lett.* 97.10 (2006), p. 103007. DOI: 10.1103/PhysRevLett.97.103007. URL: http://www.ncbi.nlm.nih.gov/pubmed/17025815.

[76] Christian L. Arrington et al. "Micro-fabricated stylus ion trap". In: *Review of Scientific Instruments* 84.8 (Aug. 2013), p. 085001. DOI: 10.1063/1.4817304.

[77] D. A. Hite et al. "Measurements of trapped-ion heating rates with exchangeable surfaces in close proximity". In: *MRS Advances* 2.41 (Jan. 2017), pp. 2189–2197. ISSN: 2059-8521. DOI: 10.1557/adv.2017.14. URL: https://doi.org/10.1557/adv.2017.14%20https://www.cambridge.org/core/product/identifier/S2059852117000147/type/journal_article.

[78] M A Rowe et al. "Transport of quantum states and separation of ions in a dual RF ion trap". In: *Quantum Information and Computation* 2.4 (2002), pp. 257–271. ISSN: 15337146.

[79] E. Paladino et al. "1/ f noise: Implications for solid-state quantum information". In: *Reviews of Modern Physics* 86 (2014), p. 361. DOI: 10.1103/RevModPhys.86.361.

[80] A. Safavi-Naini et al. "Microscopic model of electric-field-noise heating in ion traps". In: *Physical Review A* 84.2 (Aug. 2011), p. 023412. DOI: 10.1103/PhysRevA.84.023412. URL: http://link.aps.org/doi/10.1103/PhysRevA.84.023412.

[81] E. Kim et al. "Electric-field noise from carbon-adatom diffusion on a Au(110) surface: First-principles calculations and experiments". In: *Physical Review A* 95.3 (Mar. 2017), p. 033407. ISSN: 24699934. DOI: 10.1103/PhysRevA.95.033407. URL: https://link.aps.org/doi/10.1103/PhysRevA.95.033407.

[82] M. G. House. "Analytic model for electrostatic fields in surface-electrode ion traps". In: *Physical Review A* 78.3 (Sept. 2008), p. 033402. ISSN: 10502947. DOI: 10.1103/PhysRevA.78.033402.

[83] J. A. Sedlacek et al. "Method for determination of technical noise contributions to ion motional heating". In: *Journal of Applied Physics* 124.21 (Dec. 2018). ISSN: 10897550. DOI: 10.1063/1.5045326.

[84] J A Sedlacek et al. "Evidence for multiple mechanisms underlying surface electric-field noise in ion traps". In: *Physical Review A* 98 (2018), p. 63430. ISSN: 24699934. DOI: 10.1103/PhysRevA.98.063430. URL: https://journals.aps.org/pra/pdf/10.1103/PhysRevA.98.063430.

[85] Conyers Herring and M H Nichols. "Thermionic Emission". In: *Reviews of Modern Physics* 21.2 (1949), p. 185. DOI: 10.1103/RevModPhys.21.185. URL: https://doi.org/10.1103/RevModPhys.21.185.

[86] H G Dehmelt and F L Walls. ""Bolometric" Technique for the rf Spectroscopy of Stored Ions". In: *Phys. Rev. Lett.* 21.3 (July 1968), pp. 127–131. DOI: 10.1103/PhysRevLett.21.127.

[87] P. Debye, H. R. Anderson, and H. Brumberger. "Scattering by an inhomogeneous solid. II. the correlation function and its application". In: *Journal of Applied Physics* 28.6 (1957), pp. 679–683. ISSN: 00218979. DOI: 10.1063/1.1722830.

[88] Chi Sing Man et al. "On the geometric autocorrelation function of polycrystalline materials". In: *Journal of Computational and Applied Mathematics* 190.1-2 (June 2006), pp. 200–210. DOI: 10.1016/j.cam.2005.01.044.

[89] Muir Kumph et al. "Electric-field noise above a thin dielectric layer on metal electrodes". In: *New Journal of Physics* 18.2 (Nov. 2016), p. 023020. ISSN: 13672630. DOI: 10.1088/1367-2630/18/2/023020. URL: http://stacks.iop.org/1367-2630/18/i=2/a=023020?key=crossref.130a28137e2c845665e6d27aecf345a9.

[90] Kuan Yu Lin, Guang Hao Low, and Isaac L. Chuang. "Effects of electrode surface roughness on motional heating of trapped ions". In: *Physical Review A* 94.1 (July 2016), p. 013418. ISSN: 24699934. DOI: 10.1103/PhysRevA.94.013418.

[91] R. van Gastel et al. "Nothing moves a surface: Vacancy mediated surface diffusion". In: *Physical Review Letters* 86.8 (Feb. 2001), pp. 1562–1565. DOI: 10.1103/PhysRevLett.86.1562.

[92] by Jesper Møller et al. "Stochastic Geometry and Random Tessellations". In: *Research Report Series* (2007). ISSN: 1601-7811.

[93] M. B. Weissman. "1/f noise and other slow, nonexponential kinetics in condensed matter". In: *Reviews of Modern Physics* 60 (1988), p. 537. DOI: 10.1103/RevModPhys.60.537.

[94] Crystal Noel et al. "Electric-field noise from thermally activated fluctuators in a surface ion trap". In: *Physical Review A* 99.6 (June 2019), p. 063427. ISSN: 24699934. DOI: 10.1103/PhysRevA.99.063427. URL: https://link.aps.org/doi/10.1103/PhysRevA.99.063427.

[95] B E King et al. "Cooling the Collective Motion of Trapped Ions to Initialize a Quantum Register". In: *Physical Review Letters* 81.7 (1998), p. 1525. URL: https://journals.aps.org/prl/pdf/10.1103/PhysRevLett.81.1525.

[96] Joseph Aidan Delf Randall. "High-Fidelity Entanglement of Trapped Ions using Long-Wavelength Radiation". PhD thesis. 2016.

[97] K. Wright et al. "Benchmarking an 11-qubit quantum computer". In: *Nature Communications* 10.1 (Mar. 2019), p. 5464. ISSN: 2041-1723. DOI: 10.1038/s41467-019-13534-2. URL: http://www.nature.com/articles/s41467-019-13534-2%20http://arxiv.org/abs/1903.08181.

[98] Kenneth R. Brown, Jungsang Kim, and Christopher Monroe. "Co-designing a scalable quantum computer with trapped atomic ions". In: *npj Quantum Information* 2.1 (2016), pp. 1–10. ISSN: 20566387. DOI: 10.1038/npjqi.2016.34.

[99] L.-M. Duan and C. Monroe. "Colloquium: Quantum networks with trapped ions". In: *Reviews of Modern Physics* 82.2 (Apr. 2010), pp. 1209–1224. ISSN: 0034-6861. DOI: 10.1103/RevModPhys.82.1209. URL: http://link.aps.org/doi/10.1103/RevModPhys.82.1209.

[100] Tongcang Li et al. "Space-Time Crystals of Trapped Ions". In: *Physical Review Letters* 109.16 (Oct. 2012), p. 163001. ISSN: 0031-9007. DOI: 10.1103/PhysRevLett.109.163001. URL: http://dx.doi.org/10.1103/PhysRevLett.109.163001.

[101] C. Monroe et al. "Large-scale modular quantum-computer architecture with atomic memory and photonic interconnects". In: *Physical Review A - Atomic, Molecular, and Optical Physics* (2014). ISSN: 10502947. DOI: 10.1103/PhysRevA.89.022317.

[102] S Olmschenk et al. "Quantum teleportation between distant matter qubits." In: *Science (New York, N.Y.)* 323.5913 (2009), pp. 486–9. ISSN: 1095-9203. DOI: 10.1126/science.1167209. URL: http://www.sciencemag.org/cgi/content/abstract/323/5913/486.

[103] D Matsukevich et al. "Bell inequality violation with two remote atomic qubits". In: *Phys. Rev. Lett.* 100 (2008), p. 150404.

[104] D Hucul et al. "Modular entanglement of atomic qubits using photons and phonons". In: *NATURE PHYSICS* — 11 (2015). DOI: 10.1038/NPHYS3150. URL: www.nature.com/naturephysics.

[105] M Harlander et al. "Trapped-ion antennae for the transmission of quantum information." In: *Nature* 471.7337 (Mar. 2011), pp. 200–3. ISSN: 1476-4687. DOI: 10.1038/nature09800. URL: http://www.ncbi.nlm.nih.gov/pubmed/21346764.

[106] K R Brown et al. "Coupled quantized mechanical oscillators." In: *Nature* 471.7337 (Mar. 2011), pp. 196–9. ISSN: 1476-4687. DOI: 10.1038/nature09721. URL: http://www.ncbi.nlm.nih.gov/pubmed/21346762.

[107] D J Larson et al. "Sympathetic cooling of trapped ions: A laser-cooled two-species nonneutral ion plasma." In: *Phys. ˜Rev. ˜Lett.* 57 (1986), pp. 70–73.

[108] G Morigi and H Walther. "Two-species Coulomb chains for quantum information". In: *Eur. ˜Phys. ˜J. ˜D* 13 (2000), pp. 261–269.

[109] H Rohde et al. "Sympathetic ground-state cooling and coherent manipulation with two-ion crystals". In: *Journal of Optics B: Quantum and Semiclassical Optics* 3.1 (2001). ISSN: 14644266. DOI: 10.1088/1464-4266/3/1/357. URL: www.iop.org/Journals/ob.

[110] M D Barrett et al. "Sympathetic cooling of ˆ9Be^+ and ˆ24Mg^+ for quantum logic". In: *Phys. ˜Rev. ˜A* 68 (2003), p. 42302.

[111] J. P. Home et al. "Memory coherence of a sympathetically cooled trapped-ion qubit". In: *Physical Review A* 79.5 (May 2009), p. 050305. ISSN: 10502947. DOI: 10.1103/PhysRevA.79.050305. URL: https://link.aps.org/doi/10.1103/PhysRevA.79.050305.

[112] M. Guggemos et al. "Sympathetic cooling and detection of a hot trapped ion by a cold one". In: *New Journal of Physics* 17.10 (Sept. 2015). ISSN: 13672630. DOI: 10.1088/1367-2630/17/10/103001.

[113] Clemens Matthiesen et al. "Trapping Electrons in a Room-Temperature Microwave Paul Trap". In: *Physical Review X* 11.1 (Jan. 2021), p. 011019. ISSN: 2160-3308. DOI: 10.1103/PhysRevX.11.011019. URL: https://link.aps.org/doi/10.1103/PhysRevX.11.011019.

[114] D J Wineland and H G Dehmelt. "Principles of the stored ion calorimeter". In: *J. App. Phys.* 46 (1975), p. 919. DOI: 10.1063/1.321602.

[115] D J Heinzen and D J Wineland. "Quantum-limited Cooling and Detection of Radio-Frequency Oscillations by Laser-cooled Ions". In: *Phys. Rev. A* 42 (1990), p. 2977.

[116] D. A. Hite et al. "100-Fold Reduction of Electric-Field Noise in an Ion Trap Cleaned with In Situ Argon-Ion-Beam Bombardment". In: *Physical Review Letters* 109.10 (Sept. 2012), p. 103001. DOI: 10.1103/PhysRevLett.109.103001. URL: http://link.aps.org/doi/10.1103/PhysRevLett.109.103001.

[117] N. Daniilidis et al. "Probing surface electric field noise with a single ion". In: *Arxiv preprint arXiv:1307.7194* (July 2013), pp. 1–13. URL: http://arxiv.org/abs/1307.7194.

[118] J Labaziewicz et al. "Suppression of Heating Rates in Cryogenic Surface-Electrode Ion Traps". In: *Physical Review Letters* 100 (2008), p. 013001. DOI: 10.1103/PhysRevLett.100.013001. URL: http://journals.aps.org/prl/abstract/10.1103/PhysRevLett.100.013001.

[119] Jaroslaw Labaziewicz et al. "Temperature Dependence of Electric Field Noise Above Gold Surfaces". In: *Physical Review Letters* 101 (2008), p. 180602. URL: http://journals.aps.org/prl/abstract/10.1103/PhysRevLett.101.180602.

[120] M. F. Brandl et al. "Cryogenic setup for trapped ion quantum computing". In: *Review of Scientific Instruments* (2016). ISSN: 10897623. DOI: 10.1063/1.4966970.

[121] M. Niemann et al. "Cryogenic 9Be+ Penning trap for precision measurements with (anti-)protons". In: *Measurement Science and Technology* 31.3 (2019). ISSN: 13616501. DOI: 10.1088/1361-6501/ab5722.

[122] J I Cirac and P Zoller. "Quantum Computations with Cold Trapped Ions." In: *Phys. Rev. Lett.* 74.20 (May 1995), pp. 4091–4094. ISSN: 0031-9007. URL: http://www.ncbi.nlm.nih.gov/pubmed/10058410.

[123] P O Schmidt et al. "Spectroscopy using quantum logic". In: *Science* 309.5735 (July 2005), pp. 749–752. ISSN: 00368075. DOI: 10.1126/science.1114375. URL: http://www.ncbi.nlm.nih.gov/pubmed/16051790.

[124] L Tian et al. "Interfacing quantum-optical and solid-state qubits." In: *Physical Review Letters* 92.24 (June 2004), p. 247902. ISSN: 0031-9007. URL: http://www.ncbi.nlm.nih.gov/pubmed/15245134.

[125] L Tian and P Zoller. "Coupled ion-nanomechanical systems." In: *Phys. Rev. Lett.* 93.26 Pt 1 (Dec. 2004), p. 266403. ISSN: 0031-9007. URL: http://www.ncbi.nlm.nih.gov/pubmed/15697998.

[126] L. Tian, R. Blatt, and P. Zoller. "Scalable ion trap quantum computing without moving ions". In: *The European Physical Journal D* 32.2 (Nov. 2004), pp. 201–208. ISSN: 1434-6060. DOI: 10.1140/epjd/e2004-00172-5. URL: http://www.springerlink.com/index/10.1140/epjd/e2004-00172-5.